

Article

# Microstructure and Hardness Evolution of Al<sub>8</sub>Zn<sub>7</sub>Ni<sub>3</sub>Mg Alloy after Casting at very Different Cooling Rates

Pavel Shurkin <sup>1,\*</sup>, Torgom Akopyan <sup>1,2</sup>, Nataliya Korotkova <sup>1</sup>, Alexey Prosviryakov <sup>3</sup>,  
Andrey Bazlov <sup>3</sup>, Alexander Komissarov <sup>4</sup> and Dmitry Moskovskikh <sup>5</sup>

<sup>1</sup> Department of Metal Forming, National University of Science and Technology MISiS, Leninsky Ave. 4, 119049 Moscow, Russia; nemiroffandtor@yandex.ru (T.A.); darkhopex@mail.ru (N.K.)

<sup>2</sup> Baikov Institute of Metallurgy and Materials Science, Russian Academy of Sciences, Leninsky Ave. 49, 119991 Moscow, Russia

<sup>3</sup> Department of Physical Metallurgy of Non-Ferrous Metals, National University of Science and Technology MISiS, Leninsky Ave. 4, 119049 Moscow, Russia; pro.alex@mail.ru (A.P.); bazlov@misis.ru (A.B.)

<sup>4</sup> Laboratory of Hybrid Nanostructured Materials, National University of Science and Technology MISiS, Leninsky Ave. 4, 119049 Moscow, Russia; komissarov.alex@gmail.com

<sup>5</sup> Centre of Functional Nanoceramics, National University of Science and Technology MISiS, Leninsky Ave. 4, 119049 Moscow, Russia; mos@misis.ru

\* Correspondence: pa.shurkin@gmail.com

Received: 13 May 2020; Accepted: 5 June 2020; Published: 7 June 2020

**Abstract:** In this study, we combined both a high strength Al-8%Zn-3%Mg aluminum matrix and a reinforcing contribution of Al<sub>3</sub>Ni intermetallics in Al<sub>8</sub>Zn<sub>7</sub>Ni<sub>3</sub>Mg hypereutectic alloy with a tuned microstructure via a variation of cooling rates from 0.1 K/s to 2.3 × 10<sup>5</sup> K/s. Using the ThermoCalc software, we analyzed the effect of nickel content on the phase equilibria during solidification and found out that 7%Ni provides a formation of equal fractions of primary (6.5 vol.%) and eutectic (6.3 vol.%) crystals of the Al<sub>3</sub>Ni phase. Using microstructural analysis, a refinement of intermetallics with an increase in cooling rate was observed. It is remarkable that the structure after solidification at ~10<sup>3</sup> K/s across 1 mm flake casting consists of a quasi-eutectic with 1.5 μm Al<sub>3</sub>Ni fibers, while an increase in the cooling rate to ~10<sup>5</sup> K/s after melt spinning leads to the formation of 50 nm equiaxed Al<sub>3</sub>Ni particles. Under these conditions, the alloy showed an aging response at 200 °C, resulting in hardness of 200 HV and 220 HV, respectively. After 470 °C annealing, the fibers in the 1 mm sample evolved to needles. However, in melt-spun ribbons, the particles were kept globular and small-sized. Overall, the results may greatly contribute to the development of new eutectic type composites for rapid solidification methods.

**Keywords:** composite materials; hypereutectic aluminum alloys; Al-Zn-Mg alloys; rapid solidification; eutectic; CALPHAD; microstructure; intermetallics; precipitation hardening

## 1. Introduction

Due to the growing demand in strong lightweight materials, numerous studies have been dedicated to increase aluminum alloys strength. Since the Al-Zn-Mg-(Cu) alloys (7xxx) are the class of Al-based materials with the highest strength, their application has made advances for years in aircraft and space components [1,2]. The most common approaches toward the strengthening of 7xxx alloys are precipitation hardening and work hardening [3–5]. According to [6], conventional 7075 alloy may have 600 MPa tensile strength (T6), while by using the complex alloying and processing techniques the properties can be further enhanced. For example, according to [7], the von Mises yield rule of the dislocation theory, based on the yield prediction of the isotropic material under complex

loading condition, says that they can reach more than 1148 GPa yield strength. This value was partially confirmed in some studies [8–10], where about 700–900 MPa tensile strength was achieved as a result of a raise in the overall content (Zn + Mg + Cu), addition of precipitation inoculants like Ag or Sc, and complex thermomechanical treatment, including cold working or severe plastic deformation. However, the increase in strength can also be achieved by creating a composite material with a high fraction of in-situ reinforcing particles [11,12]. The accelerated solidification of the alloys, such as in the case of melt spinning or selective laser melting (hereafter referred to as SLM), can minimize the decrease in ductility caused by reinforcing particles, while the strength can be significantly increased via the Orowan looping mechanism [13] or a load transfer [14]. Therefore, we find it worth considering to strengthen Al-Zn-Mg alloy using an in-situ particulate reinforcing approach which has been widely implemented for various Al-based materials.

Aluminum matrix composites (AMCs) have become popular during the last decades, and nowadays the amount of their demand grows along with the requirements for properties of products and the technology of their fabrication [15]. Most AMCs are post-produced by the introduction of ceramic particles (e.g.,  $\text{Al}_2\text{O}_3$ , SiC, AlN, etc.) via casting methods (stir/squeeze casting), powder and granule metallurgy, combustion synthesis, etc. [15–20]. Nevertheless, their fabrication faces challenges like difficulty in producing a smaller particle size [15] and poor wettability between ceramics and molten aluminum [20]. These disadvantages cause strong restrictions on their applications, especially at a high volume of the reinforcement.

Aluminum-based alloying systems offer opportunities to fabricate AMCs reinforced by particles formed after natural (in-situ) crystallization which provide their homogenous distribution. For example, the most common commercial eutectic-based Al-Si alloys share many properties of ceramic reinforced composites [21]. Since the mechanical properties of the AMCs are tuned by controlling the type, size, morphology, and volume fraction of the filler, the prevalent number of the Al-Si in-situ composites are hypereutectic (>12%Si) and fabricated using special techniques providing rapid solidification (hereafter referred to as RS methods) in order to avoid a coarse primary silicon phase and achieve a quasi-eutectic microstructure phenomena [22,23]. In this case, the strengthening is provided by the formation of a homogeneously distributed eutectic mixture.

However, the tensile properties of Al-Si composites are low (e.g., UTS < 200 MPa for consolidated powder product [24]). Moreover, when it comes to 7xxx alloys, it is recognized that silicon is a harmful impurity since it causes  $\text{Mg}_2\text{Si}$  phase formation which leads to a reduction of precipitation strengthening [25]. This statement is supported by official data presented in the Aluminium Association standard, e.g., commercial 7075 and 7068 alloys contain up to 0.4 wt.% and 0.12% Si, respectively [26].

Meanwhile, another eutectic-forming element, nickel, does not interact with zinc and magnesium. The  $\text{Al}_3\text{Ni}$  compound has a tensile strength of about 2160 MPa and an acceptable Young modulus of 116–152 GPa that makes it reasonable for reinforcing of aluminum [27]. Moreover, its orthorhombic lattice provides incoherency toward aluminum [28]. Some near eutectic (<4 wt.%Ni) Al-Zn-Mg-Ni based on (Al) +  $\text{Al}_3\text{Ni}$  eutectic alloys are recognized to be promising as structural materials fabricated by casting and metal forming technologies [29,30], while Al-Zn-Mg/ $\text{Al}_3\text{Ni}$  composites with a high volume of reinforcement (e.g., at hypereutectic concentrations of nickel) have not been described in depth. The enhancement of the aging rate along with  $\text{Al}_3\text{Ni}$  phase volume fraction was reported in [31]. The 7005/(0–10.4 vol.%)  $\text{Al}_3\text{Ni}$  composite was prepared by metal mold gravity casting and there were particles of more than 50  $\mu\text{m}$  in size. Thus, their contribution into reinforcing is reasonable to be low. The approach toward refining of  $\text{Al}_3\text{Ni}$  primary crystals up to 5  $\mu\text{m}$  by rolling was suggested in the study on 7050/(5–10 wt.%) Ni composite [7]. It is alleged that the yield strength calculated by the Orowan equation can get 630 MPa, while the brittle fracture surface was shown. Both these papers do not consider the RS methods to obtain a quasi-eutectic structure. In an earlier research [32], the formation of the fully eutectic structure in Al-7%Ni hypereutectic alloy after unidirectional solidification is reported. In Martínez-Villalobos et al.'s study [33], the same result on Al-8%Ni after

melt spinning was achieved and an effectiveness of reinforcement was shown to be due to ultrafine  $\text{Al}_3\text{Ni}$  particles formation.

As for matrix, the experiments on melt-spun ribbons of Al-Zn-Mg alloys showed an opportunity of obtaining a supersaturated solid solution without prior annealing for quenching [34]. The same result was achieved after rapid solidification released during SLM of 7068 alloy along with providing precipitation hardening via the aging of as-built parts [35]. In this study, we chose the copper-free matrix system Al-8%Zn-3%Mg as basis related to the strongest commercial 7xxx alloys (7001, 7090, 7055, etc. [26]). We do not consider copper addition because it causes unreasonable complication of phase composition, as it is clearly shown in a pivotal research [36] on the optimization of Al-Zn-Mg-Cu-Ni alloys.

As for reinforcement, the key requirements are to possess a high enough volume of aluminides particles and an absence of the primary crystals in the structure. Thus, it is mainly desirable to obtain a fully eutectic structure on the supersaturated matrix field. To ensure a high concentration of reinforcement particles, the study is dedicated on nickel content of 7% that is substantiated in the computational section. Since the morphology of the  $\text{Al}_3\text{Ni}$  phase can be tuned on the cooling rate basis, we followed the investigation path via the study of the phase diagrams and experimental simulation of cooling rate enhancement.

From the above, the current paper aims to investigate the evolution of the solidification path, structure, and hardness depending on cooling rate variation from slow to rapid solidification of the Al8Zn7Ni3Mg alloy by thermodynamic calculation and experimental study.

## 2. Materials and Methods

Initially, we investigated details of Al-8%Zn-3%Mg alloys with various nickel contents, in particular, solidification path and phase composition using the Thermo-Calc software (Version 3.1, TCA14 Al-based alloy database, Thermo-Calc Software AB, Stockholm, Sweden) [37]. Single point equilibrium, phase diagram, property diagram, and Scheil–Goulliver solidification simulation options were used.

For the experimental section, the Al8Zn7Ni3Mg alloy was the main test material. The samples were prepared by melting high-purity aluminum (99.99%Al), zinc (99.97%Zn), magnesium (99.9%Mg), and Al20%Ni master alloy in a graphite–chamotte crucible using a Nabertherm K 1/13 (Nabertherm GmbH, Lilienthal, Germany) resistance furnace in an air atmosphere. The melt temperature was kept at 850 °C and the total time of the melting process was about 90 min. The Al20%Ni master alloy was mixed into the molten aluminum using a graphite stick. Before casting, the melt was purified by dry  $\text{C}_2\text{Cl}_6$  powder. The chemical composition as determined by spectral analysis is presented in Table 1.

**Table 1.** Chemical composition of the experimental alloy.

Designation	Concentrations, wt. %			
	Zn	Mg	Ni	Al
Al8Zn7Ni3Mg	7.79	3.13	7.16	Balance

In order to obtain a variety of cooling rates, we provided different solidification conditions. A portion of molten metal ~50 g was solidified in the furnace, and thus the lowest cooling rate was achieved (FC sample). Three cooling conditions were provided via casting. We obtained cylindrical samples of 30 mm and 5 mm in diameter, and a thin flake of less than 1 mm via pouring onto a cold steel heat sink. The highest cooling rate was induced using a melt spinning (MS sample) of experimental alloy ingot via pouring a molten metal onto a rotating copper wheel of DVX-II apparatus (Dexing Magnet Tech. CO. Ltd., Xiamen, China) in an argon gas atmosphere. The linear rotation speed of the copper wheel was 30 m/s. A general view of the samples is demonstrated in Figure 1.

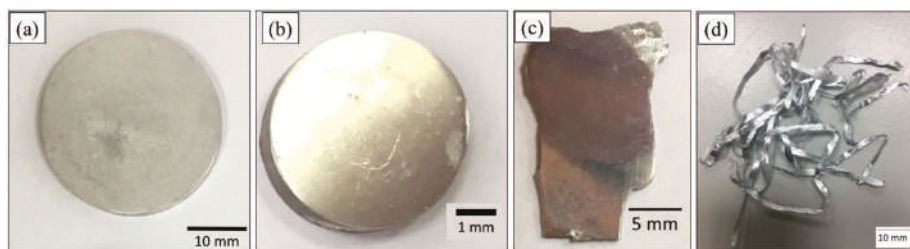


**Figure 1.** Experimental cast samples and melt-spun ribbons: (a) 30 mm cast sample; (b) 5 mm cast sample; (c) 1 mm cast sample; (d) melt-spun ribbon.

The microstructure was examined by optical microscopy (OM, Axio Observer MAT, Carl Zeiss Microscopy GmbH, Oberkochen, Germany), scanning electron microscopy (SEM, TESCAN VEGA3, Tescan Orsay Holding, Brno, Czech Republic) with an electron microprobe analysis system (EMPA, Oxford Instruments plc, Abingdon, UK), and the Aztec software (Version 3.0, Oxford Instruments plc, Abingdon, UK). The metallographic samples were ground with SiC abrasive paper and polished with 1  $\mu\text{m}$  diamond suspension. A total of 1% hydrogen fluoride (HF) water solution was used for etching. To investigate the structure of the melt-spun ribbons, we used transmission electron microscopy (TEM, JEM-2100, JEOL Ltd., Tokyo, Japan).

The size of the dendritic cells (dendritic parameter,  $d$ ), as well as of the intermetallics, was experimentally determined using metallography from high-contrast microstructural images processed with the appropriate software, ImageJ (National Institutes of Health, Bethesda, MD, USA). The Horizontal Lines option was used for implementing the stereological method of measuring the relative length of the phase regions. To obtain reliable data, we analyzed at least 10 fields in the microstructure for defining the content of each structural component. The experimental dendritic parameter data were used for evaluating the cooling rate in the alloy crystallization temperature range using a well-known empirical relationship [38]:

$$V_c = (A/d)^{1/n}, \quad (1)$$

where  $V_c$ —cooling rate upon solidification in K/s,  $d$ —dendritic parameter in  $\mu\text{m}$  and  $A$ ,  $n$ —material-dependent constants.

Since we do not take determination of the precise material dependent constants as a mandatory, they were taken from [20] for high-strength Al-Zn-Mg-Cu alloys as  $A = 100$  and  $n = 1/3$ .

Some samples were selectively subjected to a T5 heat treatment (aging at 200  $^{\circ}\text{C}$  for 1 h without prior quenching) and a T4 heat treatment (470  $^{\circ}\text{C}$  for 1 h). To control the properties evolved, a Vickers' hardness test at a load of 10 g (0.1 N) and 5 s dwell (for the MS sample), and at a load of 1 kg (10 N) and a dwell time of 10 s (for other samples) was used.

### 3. Results and Discussion

#### 3.1. Computational Section

The polythermal section shown in Figure 2a indicates that under equilibrium conditions the nickel addition to the Al-8%Zn-3%Mg alloy significantly influences on the solidification path shifting to a hypereutectic manner at over 3.6%Ni. The Al-Zn-Mg-Ni system is convenient to study due to a lack of interaction between Al-Zn-Mg and Al-Ni systems. Thus, all of Zn and Mg are bonded into the T phase ( $\text{Al}_2\text{Mg}_3\text{Zn}_3$ ) which is responsible for precipitation hardening of alloys with a Zn/Mg atomic mass ratio of less than 1 [39]. The liquidus line rises and the equilibrium solidus decreases slightly with an increase in nickel concentration in hypereutectic alloys. The Al8Zn7Ni3Mg alloy shows an experimental liquidus and solidus temperature of 665 and 520  $^{\circ}\text{C}$ , respectively. However,

the Scheil–Goulliver simulation showed that the solidification range is much higher than the one in equilibrium condition and it ends with the proceeding of the [(Al) + Al<sub>3</sub>Ni + T] reaction at a temperature of 478 °C (dotted line in the polythermal section). The temperatures, determined by thermal analysis using a single chromel–alumel thermocouple submerged into the melt, sufficiently agree with the calculated data that especially fair for non-equilibrium solidus. The reactions [L→Al<sub>3</sub>Ni] at 659 °C, [L + Al<sub>3</sub>Ni + (Al)] at 624 °C, and [L + Al<sub>3</sub>Ni + (Al) + T] at 478 °C are detected. On the one hand, such a low solidus intrinsic to 7xxx alloys deteriorates their hot cracking tolerance in some RS methods, like SLM [40]. On the other hand, having a high volume of eutectic may lead to an improvement of brittleness due to cracking healing in the solid–liquid state [41].

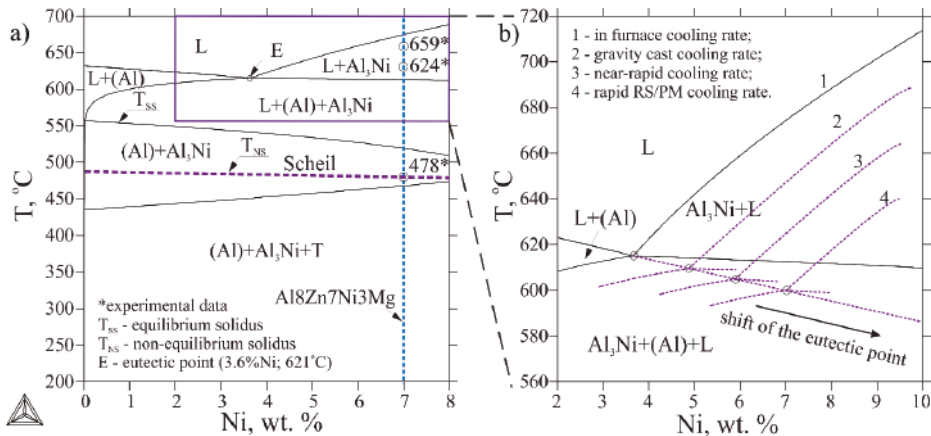


**Figure 2.** (a) Polythermal section of a Al-Zn-Mg-Ni system at 8%Zn and 3%Mg with marked non-equilibrium solidus calculated by Scheil–Goulliver simulation and (b) schematic representation of the solidification path shift as a result of an increase in the cooling rate.

In addition, Figure 2b schematically shows how the binary eutectic point shift depends on the cooling rate. According to [42], under high undercooling, diffusion in the liquid phase may be hindered causing local changes in composition and difference in local solidification rates. Under this condition, the sustainable extension of Zn and Mg solubility in the (Al) matrix can be expected [34]. In addition, the temperatures of liquidus and solidus may be lower than the equilibrium ones. It is anticipated that the experimental samples may solidify via different paths, causing a variety of structures from highly-hypereutectic to hypoeutectic, including eutectic manner if the two phases would solidify simultaneously in a diffusion coupled fashion. These microstructures can be qualified as quasi-structures, because the corresponding alloy is hypereutectic in general.

According to Figure 2a, the solvus temperature corresponding to the dissolution of the T phase (Al<sub>2</sub>Mg<sub>2</sub>Zn<sub>3</sub>) increases along with nickel content and therefore the [(Al) + Al<sub>3</sub>Ni] area is narrowing as well as the suitable range of quenching temperatures. We chose a temperature of 470 °C as a conventional temperature for a solid solution treatment of 7xxx alloys [1].

Figure 3a shows how the (Al) solid solution composition evolves at 470 °C depending on nickel content. It is assumed to be the same after rapid solidification. According to the (Al) matrix composition, we simulated its decomposition at the chosen aging temperature of 200 °C as a volume fraction of precipitation products both T' and M'. The graph shows that nickel addition contributes to a gradual growth of Zn and Mg content in (Al) matrix, as well as precipitates volume, respectively. The solid solution of the experimental Al8Zn7Ni3Mg alloy composes 9.6%Zn and 3.6%Mg, promoting precipitations of 9.6 vol.% both T' and M' dispersoids responsible for matrix hardening. It is clearly seen that the (Al) solid solution composition and volume of dispersoids see a plateau (9.7%Zn and

3.7%Mg in (Al) and 10.1 vol.% of precipitates) at over 7.5%Ni. The further addition of nickel may cause an undesirable end of solidification via ternary eutectic [(Al) + Al<sub>3</sub>Ni + T] leading to the appearance of an additional quantity of the T-phase in the structure undissolved in aluminum. That way, a higher amount of nickel seems to be unreasonable.

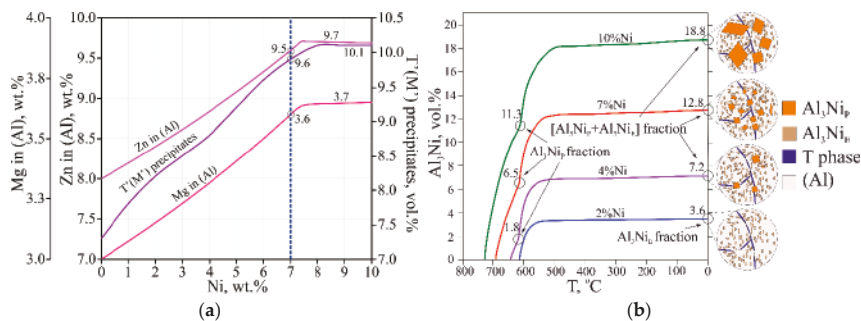


**Figure 3.** (a) Composition of the (Al) solid solution at 470 °C and corresponding volume fraction of T' (M') precipitates at 200 °C depending on nickel content in Al-8%Zn-3%Mg; (b) relationship between volume fraction of Al<sub>3</sub>Ni phase and temperature at various nickel contents in Al-8%Zn-3%Mg alloy and schematic display of the structure evolution.

Figure 3b shows the volume fraction of the Al<sub>3</sub>Ni phase in Al-8%Zn-3%Mg-xNi (x = 2%, 4%, 7%, 10%) alloy depending on the temperature under equilibrium conditions. In hypereutectic alloys, the formation of two types of intermetallics is possible. The primary phase (Al<sub>3</sub>Ni<sub>p</sub>) appears before the aluminum solid solution. Then it progresses with eutectic particles (Al<sub>3</sub>Ni<sub>E</sub>) formation along with aluminum. As we schematically represented, the Al<sub>3</sub>Ni<sub>E</sub> type nucleates as disperse particles, while the Al<sub>3</sub>Ni<sub>p</sub> type commonly has a faceted morphology. While at 2% and 4%Ni the volume of the reinforcement is significantly scarce (3.6% and 7.2%), at increasingly hypereutectic concentrations (10%Ni) the volume fraction is superior (18.8%), but the Al<sub>3</sub>Ni<sub>p</sub> fraction is dominant (11.3%). On this occasion, the suppression of the pre-eutectic stage may be not accomplished in our experimental conditions. Barclay et al. [32], who first achieved a quasi-eutectic structure in Al-Ni hypereutectic alloys by the RS method, found that Al-10%Ni alloy requires a five times higher solidification rate than Al-7%Ni alloy for achieving suppression of the Al<sub>3</sub>Ni primary crystallization.

Thus, the experimental Al8Zn7Ni3Mg alloy exhibits appropriate volume fraction of intermetallics (12.8%) composed of balanced eutectic (6.3%) and primary (6.5%) crystals. In addition to that, it shows the highest promise for precipitation hardening, a low inter-particles spacing is anticipated, taking into account positive results on binary alloys [32,33].

### 3.2. Solidification Path and Structure Analysis

The results of the cooling rate estimation are shown in Table 2, as well as the change in microstructural peculiarities pertaining to the dendritic parameter and Al<sub>3</sub>Ni intermetallics size. As can be seen, an increase in the cooling rate drives a refinement of primary crystals up to the ultimate suppression of the pre-eutectic stage after cooling at more than 10<sup>3</sup> K/s.

The results are supported by a general view of microstructure evolution from a slow rate furnace-cooled sample to rapidly cooled melt-spun ribbons (Figure 4). In OM images, the Al<sub>3</sub>Ni phase is visible as brown inclusions embedded into the light matrix of the (Al) solid solution, and otherwise, in the SEM image light intermetallics are incorporated into the dark matrix. Generally, the evolution allows to estimate the formation of a quasi-eutectic structure under an increase in the cooling rate.

**Table 2.** Microstructure peculiarities of the Al8Zn7Ni3Mg alloy depending on the cooling rate.

Experimental Sample	Dendritic Parameter ( $d$ ) <sup>1</sup> , $\mu\text{m}$	Cooling Rate ( $V_c$ ) <sup>2</sup> , K/s	Al <sub>3</sub> Ni Size Range <sup>1</sup> , $\mu\text{m}$	Al <sub>3</sub> Ni Median Size <sup>1</sup> , $\mu\text{m}$ (Al <sub>3</sub> Ni <sub>E</sub> /Al <sub>3</sub> Ni <sub>P</sub> )
FC	198 ± 31	0.1	30–351	12/225
30 mm cast	39 ± 6	17	20–94	4/13
5 mm cast	19 ± 6	133	5–43	2/7
1 mm cast	9 ± 2	$1.4 \times 10^3$	1–3	1.5/-
MS	$1.6 \pm 0.3$	$2.3 \times 10^5$	0.03–1.8	0.3/-

<sup>1</sup> determined using image analysis software; <sup>2</sup> calculated using the Equation (1).

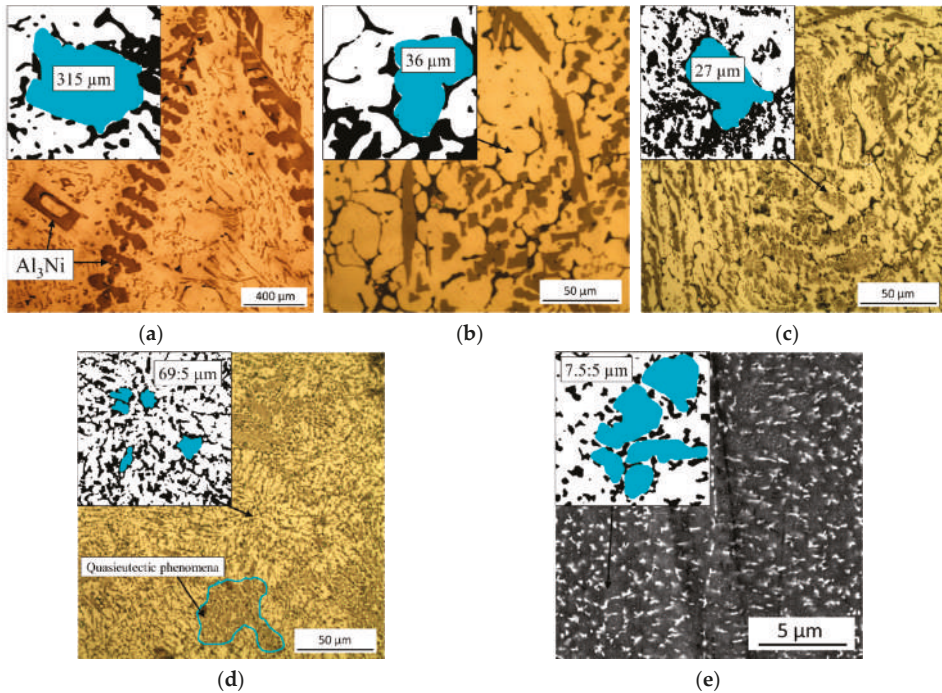


**Figure 4.** Microstructures of the Al8Zn7Ni3Mg alloy after solidification at different cooling rates, including binary imaging used for dendritic parameter determination: (a) furnace-cooled (FC) sample; (b) 30 mm cast sample; (c) 5 mm cast sample; (d) 1 mm cast sample; (e) melt spinning (MS) sample.

The microstructure of the FC sample (Figure 4a) can be qualified as the nearest to the equilibrium one. During in-furnace solidification, a large fraction of imposingly coarse primary crystals of up to 351  $\mu\text{m}$  can be observed, which are probably responsible for a low ductility of material under such condition. The presented pattern reliably agrees with a schematic one shown in Figure 2b. The primary Al<sub>3</sub>Ni<sub>P</sub> crystals are in an equilibrium with the eutectic mixture [(Al) + Al<sub>3</sub>Ni<sub>E</sub>] in which the eutectic-origin particles are relatively small (medium size 12  $\mu\text{m}$ ).

Considering the structure of gravity cast samples, we managed to achieve a significant difference among their solidification conditions and cooling rates as well. The cooling rate of 17 K/s for the 30 mm cast sample (Figure 4b) was calculated using equation 1 and a dendritic parameter of around 39  $\mu\text{m}$ . The conception of the microstructure does not look modified in comparison to the furnace-cooled sample, but the refinement is obvious from the scale and increased number of dendritic cells reduced fivefold in size along with dramatically reduced intermetallics.

A further increase in the cooling rate resulted in intermetallic bands formation that indicates a closeness of the solidification path to the eutectic one. In the 5 mm cast sample (Figure 4c), there is still an extremely high number of  $\text{Al}_3\text{Ni}$  needle-like primary intermetallics, halved in size, obtained via near-rapid cooling ( $d \sim 20 \mu\text{m}$ ,  $V_c = 133 \text{ K/s}$ ). Meanwhile, the 1 mm cast sample ( $d \sim 10 \mu\text{m}$ ,  $V_c = 1.4 \times 10^3 \text{ K/s}$ ) contains wide areas where the coupled growth of  $\text{Al}_3\text{Ni}$  and the (Al) solid solution was provided (Figure 4d). This as qualified quasi-eutectic structure consists of micron-scale intermetallics, mixed with a hypoeutectic structure in vicinity, allowed to estimate the dendritic parameter. Such inhomogeneous structure is probably due to different crystallization front and related to a tough experimental condition. The quasi-eutectic structure is believed to develop via the following solidification path [43–45]. The  $\text{Al}_3\text{Ni}$  phase as part of the eutectic [(Al) +  $\text{Al}_3\text{Ni}$ ] nucleates first due to its higher melting point. Next, the (Al) solid solution nucleates in the nickel depleted zone around the  $\text{Al}_3\text{Ni}$  particles preventing its growth. Therefore, the residual liquid phase is enriched with the nickel until its composition reaches the eutectic point. Thus, the reciprocal growth of both the  $\text{Al}_3\text{Ni}$  phase and the (Al) solid solution occurs.

In contrast, under melt spinning conditions, the highest cooling rate was achieved resulting in an ultrafine microstructure with visible dendritic cells of about  $1.5 \mu\text{m}$  (Figure 4e). The estimated cooling rate is  $2.3 \times 10^5 \text{ K/s}$ , which agrees with literature data [22]. The quasi-eutectic-origin intermetallics of submicron size are located along (Al) solid solution dendritic cells and the ultimate structure looks hypoeutectic. However, some areas are revealed to have very small in-bulks particles, which are to be studied using a high-magnification technique.

The microstructure of the 5 mm cast sample was studied in detail (Figure 5). According to EMPA analysis (Figure 5b), the white phase (in Figure 5a) corresponds to an insoluble  $\text{Al}_3\text{Ni}$  phase with a homogenous composition of 76% Al and 24%Ni. In the vicinity, T phase veins are clearly observed. It is striking that the most part of the Zn and Mg are dissolved in the (Al) matrix even under cooling at  $133 \text{ K/s}$ . Hence, it is reasonable to anticipate a dramatic extension of solid solubility in samples obtained at higher cooling rates.

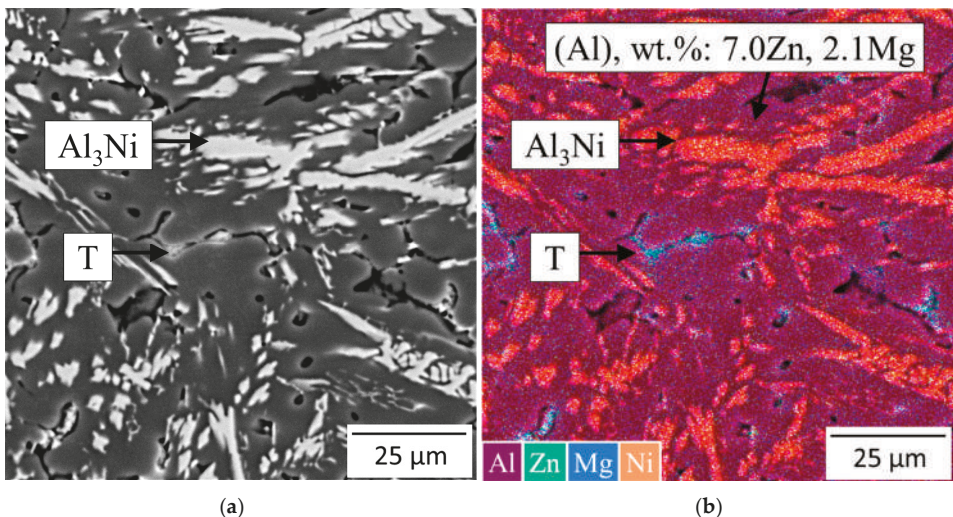


**Figure 5.** Microstructure of the 5 mm cast sample of the  $\text{Al}_8\text{Zn}_7\text{Ni}_3\text{Mg}$  alloy: (a) SEM; (b) multilayer elemental map.

Ultimately, the analysis of the structure revealed a significant deviation of the solidification path from a local equilibrium condition. Microstructural peculiarities (dendritic cells and intermetallics) were far much refined under an increase in the cooling rate, and their characterization in the samples

after a cooling rate of more than  $10^3$  K/s requires for detailed analysis using higher magnification. Preliminary, it is believed that a needle-like  $\text{Al}_3\text{Ni}$  phase, occurring in the structure of the FC, 30 mm, and 5 mm cast samples, is responsible for brittle behavior, while globular particles presented in other samples could play a reinforcing role in enhancing strength without a substantial loss of ductility. Moreover, the supersaturation of the (Al) solid solution is expected and will be discussed upon the hardness measurement results.

### 3.3. Characterization of the Quasi-Eutectic Structure

In the microstructure of the 1 mm cast sample (Figure 6), the tough casting condition resulted in the shrinkage cavities formation along the grains. There is no primary phase detected, and the structure seems to be homogeneous and quasi-eutectic in general. As can be seen, the  $\text{Al}_3\text{Ni}$  eutectic bands are in the bulk of the (Al) solid solution, and in their vicinities, Zn and Mg rich areas are presented with an Al-8.7%Zn-3.4%Mg composition. This result virtually agrees with a previously calculated (Al) matrix composition at 470 °C and corresponds to a supersaturated condition. The magnified section of the [(Al) +  $\text{Al}_3\text{Ni}$ ] eutectic band shows that it has a rather fibrous morphology with a linear size of up to 3  $\mu\text{m}$ . These microstructure features exhibit a correspondence to fiber-reinforced metal matrix composites, so it probably yields the best load transfer efficiency.

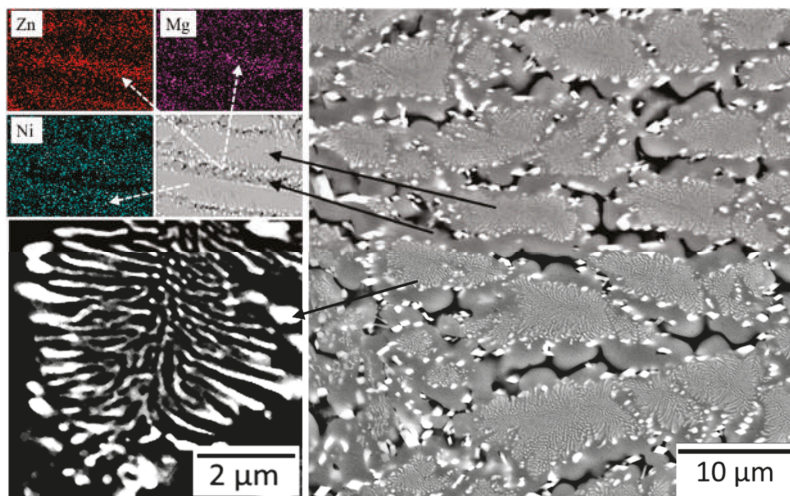
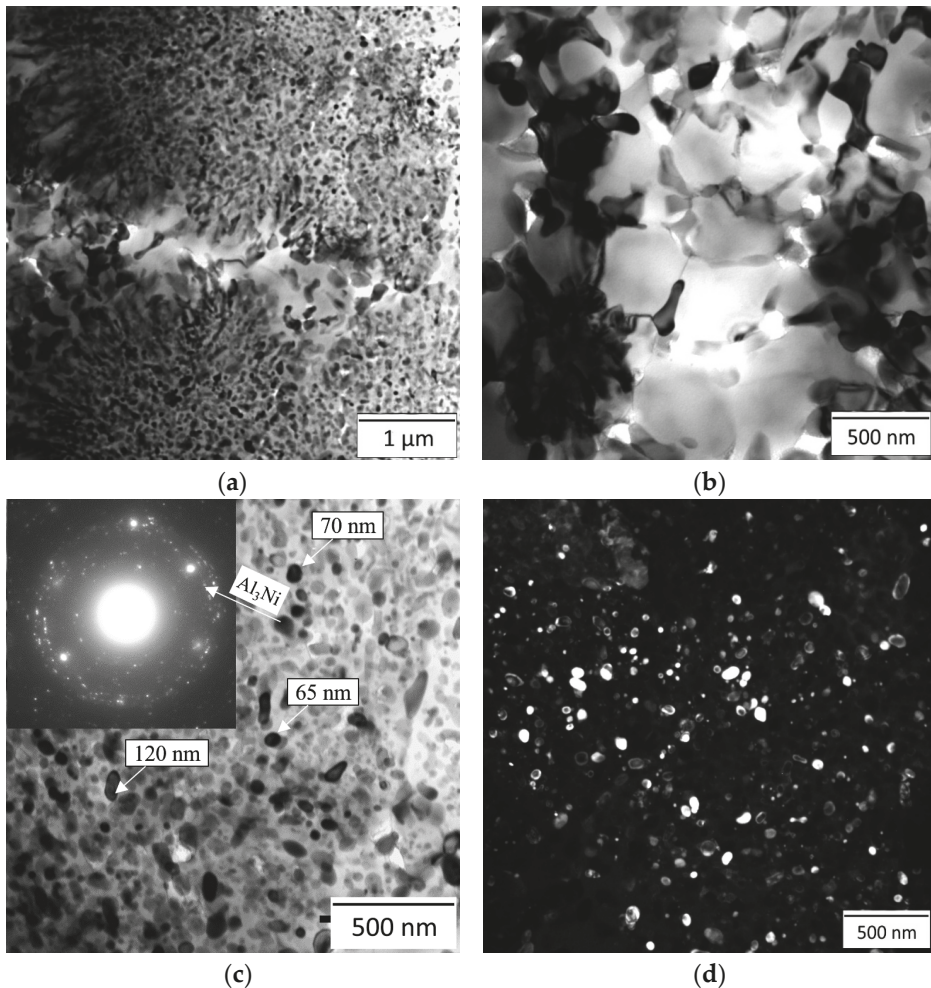


Figure 6. Microstructure of the  $\text{Al}_8\text{Zn}_7\text{Ni}_3\text{Mg}$  alloy after solidification at  $1.4 \times 10^3$  K/s.

Figure 7 displays the TEM characterization of the structure appearing in the melt-spun ribbons. As can be seen from Figure 7a, it is conceptually similar to the quasi-eutectic structure of the 1 mm cast sample, because it also shows wide bands of the fine intermetallics, surrounded by dendritic bulks of (Al) solid solution, which are clearly seen in Figure 7b. Since the dendritic cells presented are less than 300 nm in size, we can assume that the cooling rate achieved in some areas was much higher than  $\sim 10^6$  K/s, probably provided by greater thermal conductivity of the aluminum matrix than intermetallics. The incoherent equiaxed  $\text{Al}_3\text{Ni}$  particles with a median linear size of 50 nm are located within the (Al) matrix (Figure 7c). The dark field image (Figure 7d) served as a more contrasting image for inter-particles spacing estimation. Its value is in the 10–50 nm range, which, in turn, shows good promise for a contribution into strength along with precipitate shearing due to possible naturally or artificially triggered decomposition of the (Al) solid solution.



**Figure 7.** Microstructure of the melt-spun ribbons (MS sample,  $2.3 \times 10^5$  K/s) of the Al<sub>8</sub>Zn<sub>7</sub>Ni<sub>3</sub>Mg alloy: (a) general view of the intermetallic bands; (b) a (Al) dendritic structure appeared in the bands' vicinities; (c) light field image of the globular intermetallics' band; (d) dark field image.

### 3.4. Hardness and Influence of Heat Treatment

The results of the hardness measurement are shown in Figure 8. As it was earlier shown, the FC sample comprises of primary intermetallics of significantly giant linear size, and therefore, the hardness of 52 HV presented reflects the footprint after indentation into the (Al) matrix. Hence, the nickel contribution is relatively low, as well as the hardness value. A further increase in the cooling rate causes a strong visible effect on the hardness value. For comparison, it increased twofold in the 30 mm cast sample and threefold in the 5 mm and 1 mm samples. The most value of 195 HV was achieved in melt-spun ribbons, which have the finest virtually qualified nanocomposite microstructure. Furthermore, it is worth considering that the most uniform distribution of the hardness values was obtained in cast samples, while the inhomogeneous structure of the 1 mm cast sample provided high deviation, as well as for the MS sample measured using far lower load due to brittleness.

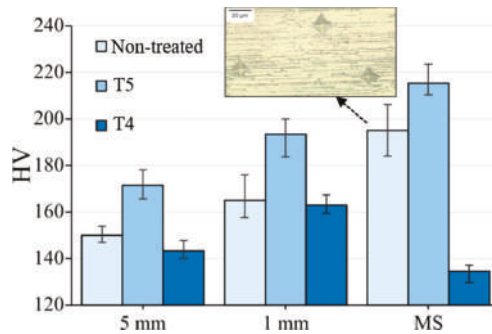


**Figure 8.** Influence of heat treatment on the hardness of experimental samples of the Al<sub>8</sub>Zn<sub>7</sub>Ni<sub>3</sub>Mg alloy.

Thermal treatment causes significant changes in microstructure and hardness, respectively. The bar chart demonstrates a relatively high aging response of around 20 HV at 200 °C without preliminary quenching in 5 mm and 1 mm cast samples as well as the MS sample. It is striking that the MS sample initially has a hardness of 200 HV, which is the same as an aged 1 mm cast sample. However, further aging leads to an increase in values of up to 220 HV, corresponding to ultrahigh-strength Al-based materials [10]. However, a further increase in temperature to 470 °C leads to a significant degradation of hardness. For all samples this is due to the (Al) matrix solutionization during alloy solidification. Moreover, for a composite-structured 1 mm cast sample and MS samples, this loss of properties is caused by a significant degradation of the intermetallics morphology.

The degradation of the Al<sub>3</sub>Ni phase morphology after a 470 °C heat treatment is highly dependent on the initial microstructure. As the as-cast 1 mm sample microstructure contains fiber-like, slightly elongated inclusions, they were conjugated along a definite crystallographic plane, resulting in significant shape deformation as a mixture of needles and coalesced particles, both blocky for load transfer (Figure 9a). Meanwhile, the MS sample initially contained equiaxed intermetallics, and heating to 470 °C caused advanced coalescence. The particles size is ranged in 0.2–2.5 μm, but their roundness is apparently appropriate to be 0.8–1 for 90% of the whole volume (Figure 9b). This factor seems to be advantageous in terms of hot consolidation of the melt-spun ribbons, hence, the microstructure of the bulk products may still be qualified as a reinforced composite.

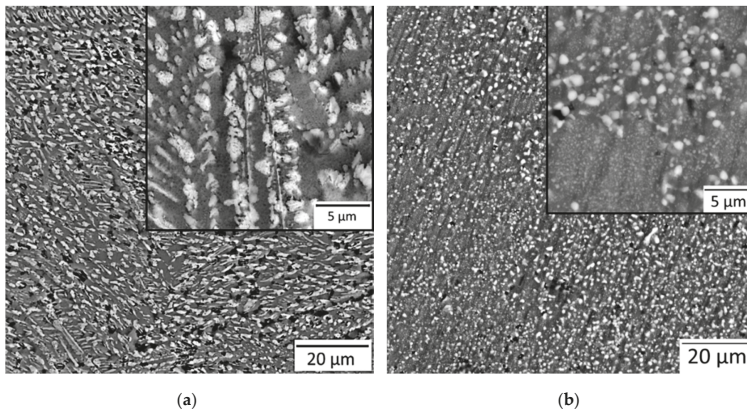


**Figure 9.** Microstructure of the Al<sub>8</sub>Zn<sub>7</sub>Ni<sub>3</sub>Mg alloy after 470 °C heat treatment: (a) 1 mm cast sample; (b) MS sample.

#### 4. Conclusions

By using computational and experimental studies, the effect of different cooling rates (0.1 K/s, 17 K/s, 133 K/s,  $1.4 \times 10^3$  K/s, and  $2.3 \times 10^5$  K/s) on the phase composition, solidification manner, microstructure, and hardness of the Al8Zn7Ni3Mg aluminum alloy has been analyzed in details. The tremendous refinement of the microstructure along with extension in Zn and Mg solid solubility was accompanied with increase in hardness as a result of solidification path shift from a hypereutectic to a eutectic and hypoeutectic one. The results are believed to be beneficial for the development of new high-strength particulate reinforced composites which do not require ex-situ intervention for the input of reinforcements. Moreover, when considering eutectic forming element addition, a decrease in hot embrittlement is anticipated. Hence, the new composition may be highly recommended for laser additive manufacturing applications. The major conclusions are as follows:

- (1) By using the CALPHAD approach, the concentration of nickel in the experimental Al8Zn7Ni3Mg alloy has been justified. While the eutectic point in the Al-8%Zn-3%Mg-Ni system corresponds to 3.6%Ni, the 7%Ni composition is highly hypereutectic. Taking into account the opportunity to shift the solidification path with further refinement caused by increase in cooling rates, the experimental alloy comprises 12.8 vol.% Al<sub>3</sub>Ni intermetallics in which half corresponds to the primary phase;
- (2) Composition of the (Al) solid solution after rapid solidification has been simulated similar to the one at the 470 °C solid solution temperature. The higher the nickel content, the more saturated the (Al) matrix. It is shown that a 7%Ni concentration is advantageous in terms of obtaining supersaturated solid solution containing 9.6%Zn and 3.6%Mg, promoting precipitation of 9.6 vol.% of T' and M' dispersoids. Meanwhile, a higher amount of nickel does not provide a significant change in these values;
- (3) By OM, SEM, and TEM analysis, the increase in cooling rates on the microstructure was investigated, showing profound opportunities for microstructure tuning. A highly hypereutectic structure was observed after solidification at 0.1 K/s, 17 K/s, and 133 K/s accompanied with a refinement of the Al<sub>3</sub>Ni phase from 50 to 7 μm in medium size. A cooling rate of  $1.4 \times 10^3$  K/s appeared to be sufficient for providing quasi-eutectic solidification manner, and most of the structure area is covered with fiber-like composite microstructure of 1.5 μm intermetallics, while the melt spinning provided a cooling rate of  $2.3 \times 10^5$  K/s resulting in a visible hypoeutectic structure with ultrafine equiaxed 50 nm intermetallics in the (Al) matrix bulk, beneficial for looping reinforcing;
- (4) The hardness test revealed a substantial increase in strengthening as a result of structure refinement. While in slow and conventionally-cooled samples the hardness of 50–150 HV is relatively not contributed by Al<sub>3</sub>Ni intermetallics appearance, the rapidly solidified samples showed a significant enhancement of 165 HV in the 1 mm cast sample and 195 HV in melt-spun ribbons. Moreover, these samples both showed a significant strengthening after low temperature annealing at 200 °C, achieving up to 220 HV;
- (5) Nonetheless, a solid solution treatment at 470 °C resulted in significant degradation of hardness. While the 1 mm cast sample saw a decrease to the initial level, the melt-spun sample degraded to obtain hardness of around 140 HV. Such a loss in properties is caused by structure coarsening. Meanwhile, the fibrous-like intermetallics coalesced to become needles and rods (up to 10 μm), and the globular particles evolved remaining a high roundness and relatively low size (0.2–2.5 μm), which is promising in terms of further consolidation processing.

**Author Contributions:** Conceptualization, P.S. and T.A.; investigation, N.K. and A.P.; methodology, A.P., A.B., and A.K.; resources, A.P., A.K., D.M., and A.B.; supervision, T.A.; writing—original draft, P.S.; writing—review & editing, P.S. and T.A. All authors have read and agreed to the published version of the manuscript.

**Funding:** This research was funded by the Russian Science Foundation (project No. 19-79-30025).

**Acknowledgments:** The authors would like to thank Mikhail Gorshenkov for providing TEM investigations.

**Conflicts of Interest:** The authors declare no conflict of interest.

## References

- Polmear, I.; StJohn, D.; Nie, J.-F.; Qian, M. Physical metallurgy of aluminium alloys. In *Light Alloys*, 5th ed.; Elsevier: London, UK, 2017; pp. 31–107. [\[CrossRef\]](#)
- Starke, E.A., Jr.; Staley, J.T. Application of modern aluminium alloys to aircraft. In *Fundamentals of Aluminium Metallurgy*; Lumley, R., Ed.; Woodhead Publishing Limited: Cambridge, UK, 2011; pp. 747–783. [\[CrossRef\]](#)
- Ditta, A.; Weia, L.; Xub, Y.; Wua, S. Microstructural characteristics and properties of spray formed Zn-rich Al-Zn-Mg-Cu alloy under various aging conditions. *Mater. Charact.* **2020**, *161*, 110133. [\[CrossRef\]](#)
- Zhao, J.; Liu, Z.; Bai, S.; Zeng, D.; Luo, L.; Wang, J. Effects of natural aging on the formation and strengthening effect of G.P. zones in a retrogression and re-aged Al-Zn-Mg-Cu alloy. *J. Alloys Compd.* **2020**, *829*, 154469. [\[CrossRef\]](#)
- Chen, Z.; Yuan, Z.; Ren, J. The mechanism of comprehensive properties enhancement in Al-Zn-Mg-Cu alloy via novel thermomechanical treatment. *J. Alloys Compd.* **2020**, *828*, 154446. [\[CrossRef\]](#)
- Tamarin, Y. *Atlas of Stress-Strain Curves*, 2nd ed.; ASM International: Novelty, OH, USA, 2002.
- Peng, G.; Tietao, Z.; Xiaoqing, X.; Zhi, G.; Li, C. Refinement mechanism research of Al<sub>3</sub>Ni phase in Ni-7050 alloy. *Rare Met. Mater. Eng.* **2013**, *42*, 6–13. [\[CrossRef\]](#)
- Aoi, I.; Kuramoto, S.; Oh-ishi, K. Mechanical properties of Al-(8,10)%Zn-2%Mg-2%Cu base alloys processed with high-pressure torsion. *Light Met.* **2015**, 179–182. [\[CrossRef\]](#)
- Ibrahim, M.F.; Samuel, A.M.; Alkahtani, S.A.; Samuel, F.H. A novel solution heat treatment of 7075-type alloy. *Light Met.* **2013**, 383–390. [\[CrossRef\]](#)
- Wang, W.; Pana, Q.; Wang, X.; Sun, Y.; Long, L.; Huang, Z. Mechanical properties and microstructure evolution of ultra-high strength Al-Zn-Mg-Cu alloy processed by room temperature ECAP with post aging. *Mater. Sci. Eng. A* **2018**, *731*, 195–208. [\[CrossRef\]](#)
- Elliot, R. *Eutectic Solidification Processing: Crystalline and Glassy Alloys*, 1st ed.; Butterworth-Heinemann: Oxford, UK, 1983. [\[CrossRef\]](#)
- Kim, C.S.; Cho, K.; Manjili, M.H.; Nezafati, M. Mechanical performance of particulate-reinforced Al metal-matrix composites (MMCs) and Al metalmatrix nano-composites (MMNCs). *J. Mater. Sci.* **2017**, *52*, 13319–13349. [\[CrossRef\]](#)
- Zhang, Z.; Chen, D.L. Contribution of Orowan strengthening effect in particulate-reinforced metal matrix nanocomposites. *Mater. Sci. Eng. A* **2008**, *483–484*, 148–152. [\[CrossRef\]](#)
- Garces, G.; Bruno, G.; Wanner, A. Load transfer in short fibre reinforced metal matrix composites. *Acta Mater.* **2007**, *55*, 5389–5400. [\[CrossRef\]](#)
- Garg, P.; Jamwal, A.; Kumar, D.; Sadasivuni, K.K.; Hussain, C.M.; Gupta, P. Advance research progresses in aluminium matrix composites: Manufacturing & applications. *J. Mater. Res. Tech.* **2019**, *8*, 4924–4939. [\[CrossRef\]](#)
- Chung, D.D.L. Metal-Matrix Composites. In *Carbon Composites*, 2nd ed.; Elsevier: London, UK, 2017; pp. 532–562. [\[CrossRef\]](#)
- Dinakaran, I. Liquid metallurgy processing of intermetallic matrix composites. In *Intermetallic Matrix Composites*; Mitra, R., Ed.; Elsevier: London, UK, 2017; pp. 167–202. [\[CrossRef\]](#)
- Gao, T.; Bian, Y.; Li, Z.; Xu, Q.; Yang, H.; Zhao, K.; Liu, X. Synthesis of a (ZrAl<sub>3</sub> + AlN)/Al composite and the influence of particles content and element Cu on the microstructure and mechanical properties. *J. Alloys Compd.* **2019**, *791*, 730–738. [\[CrossRef\]](#)
- Najarian, A.R.; Emadi, R.; Hamzeh, M. Fabrication of as-cast Al matrix composite reinforced by Al<sub>2</sub>O<sub>3</sub>/Al<sub>3</sub>Ni hybrid particles via in-situ reaction and evaluation of its mechanical properties. *Mater. Sci. Eng. B* **2018**, *231*, 57–65. [\[CrossRef\]](#)
- Bao, S.; Tang, K.; Kvithyld, A.; Engh, T.; Tangstad, M. Wetting of pure aluminium on graphite, SiC and Al<sub>2</sub>O<sub>3</sub> in aluminium filtration. *Trans. Nonferrous Met. Soc. China* **2012**, *22*, 1930–1938. [\[CrossRef\]](#)

21. Cai, Z.; Zhang, C.; Wang, R.; Peng, C.; Wu, X.; Li, H. Microstructure, mechanical and thermo-physical properties of Al–50Si–xMg alloys. *Mater. Sci. Eng. A* **2018**, *730*, 57–65. [CrossRef]
22. Dobatkin, V.I.; Elagin, V.I.; Fedorov, V.M. Structure of rapidly solidified aluminium alloys. *Adv. Perform. Mater.* **1995**, *2*, 89–98. [CrossRef]
23. Uzun, O.; Karaaslan, T.; Gogebakan, M.; Keskin, M. Hardness and microstructural characteristics of rapidly solidified Al–8–16 wt.%Si alloys. *J. Alloys Compd.* **2004**, *376*, 149–157. [CrossRef]
24. Cai, Z.; Zhang, C.; Wang, R.; Peng, C.; Qiu, K.; Feng, Y. Preparation of Al–Si alloys by a rapid solidification and powder metallurgy route. *Mater. Des.* **2015**, *87*, 996–1002. [CrossRef]
25. Hatch, J.E. *Aluminium: Properties and Physical Metallurgy*; American Society for Metals: Cleveland, OH, USA, 1984.
26. The Aluminium Association, International Alloy Designations and Chemical Composition Limits for Wrought Aluminium and Wrought Aluminium Alloys. The Aluminium Association. Available online: <https://www.aluminum.org/sites/default/files/Teal%20Sheets.pdf> (accessed on 26 April 2020).
27. Fukui, Y.; Okada, H.; Kumazawa, N.; Watanabe, Y. Near-net-shape forming of Al–Al<sub>3</sub>Ni functionally graded material over eutectic melting temperature. *Met. Mater. Trans. A* **2000**, *31*, 2627–2636. [CrossRef]
28. Nash, P.; Pan, Y.Y. The Al–Ni–Zr system (Aluminium–Nickel–Zirconium). *J. Phase Equilibria* **1991**, *12*, 105–113. [CrossRef]
29. Belov, N.A.; Zolotarevskiy, V.S. The Effect of nickel on the structure, mechanical and casting properties of aluminium alloy of 7075 type. *Mater. Sci. Forum* **2002**, *396–402*, 935–940. [CrossRef]
30. Belov, N.A.; Cheverikin, V.V.; Eskin, D.G.; Turchin, A.N. Effect of Al<sub>3</sub>Ni and Mg<sub>2</sub>Si eutectic phases on casting properties and hardening of an Al–7%Zn–3%Mg alloy. *Mater. Sci. Forum* **2006**, *519–521*, 413–418. [CrossRef]
31. Wang, S.H.; Uan, J.Y.; Lui, T.S.; Chen, L.H. Examination on the aging and tensile properties of Al–Zn–Mg/Al<sub>3</sub>Ni eutectic composite. *Met. Mater. Trans. A* **2002**, *33*, 707–711. [CrossRef]
32. Barclay, R.S.; Kerr, H.W.; Niessen, P. Off-eutectic composite solidification and properties in Al–Ni and Al–Co alloys. *J. Mater. Sci.* **1971**, *6*, 1168–1173. [CrossRef]
33. Martínez-Villalobos, M.A.; Figueroa, I.A.; Suarez, M.A.; Rodríguez, G.A.L.; Peralta, O.N.; Reyes, G.G.; López, I.A.; Martínez, J.V.; Trujillo, C.D. Microstructural Evolution of Rapid Solidified Al–Ni Alloys. *J. Mex. Chem. Soc.* **2016**, *60*, 67–72. [CrossRef]
34. Lin, Y.; Mao, S.; Yan, Z.; Zhang, Y.; Wang, L. The enhanced microhardness in a rapidly solidified Al alloy. *Mater. Sci. Eng. A* **2017**, *692*, 182–191. [CrossRef]
35. Casati, R.; Coduri, M.; Riccio, M.; Rizzi, A.; Vedani, M. Development of a high strength Al–Zn–Si–Mg–Cu alloy for selective laser melting. *J. Alloys Compd.* **2019**, *801*, 243–253. [CrossRef]
36. Belov, N.A. Sparingly alloyed high-strength aluminium alloys: Principles of optimization of phase composition. *Mater. Sci. Heat Tr.* **2012**, *53*, 19–27. [CrossRef]
37. Thermo-Calc Software TTAL5 Al-Alloys. Available online: <http://www.thermocalc.com> (accessed on 17 April 2020).
38. Neikov, O.D.; Naboychenko, S.S.; Yefimov, N.A. *Handbook of Non-Ferrous Metal Powders: Technologies and Applications*, 2nd ed.; Elsevier: London, UK, 2018; p. 995. [CrossRef]
39. Nishi, M.; Matsuda, K.; Miura, N.; Watanabe, K.; Ikeno, S.; Yoshida, T.; Murakami, S. Effect of the Zn/Mg ratio on microstructure and mechanical properties in Al–Zn–Mg alloys. *Mater. Sci. Forum* **2014**, *794–796*, 479–482. [CrossRef]
40. Galy, C.; Le Guen, E.; Lacoste, E.; Arvieu, C. Main defects observed in aluminium alloy parts produced by SLM: From causes to consequences. *Addit. Manuf.* **2018**, *22*, 165–175. [CrossRef]
41. Glazoff, M.; Khvan, A.; Zolotarevsky, V.; Belov, N.; Dinsdale, A. *Casting Aluminium Alloys: Their physical and Mechanical Metallurgy*, 2nd ed.; Elsevier: Amsterdam, The Netherlands, 2018. [CrossRef]
42. Grandfield, J.; Eskin, D.G.; Bainbridge, I. *Direct-Chill Casting of Light Alloys: Science and Technology*, 1st ed.; John Wiley & Sons, Inc.: Hoboken, NJ, USA, 2013.
43. Todeschini, P.; Champier, G.; Samuel, F.H. Production of Al–(12–25) wt% Si alloys by rapid solidification: Melt spinning versus centrifugal atomization. *J. Mater. Sci.* **1992**, *27*, 3539–3551. [CrossRef]

44. Ma, P.; Prashanth, K.G.; Scudino, S.; Jia, Y.; Wang, H.; Zou, C.; Wei, Z.; Eckert, J. Influence of Annealing on Mechanical Properties of Al-20Si Processed by Selective Laser Melting. *Metals* **2014**, *4*, 28–36. [[CrossRef](#)]
45. Lekatou, A.; Sfikas, A.K.; Petsa, C.; Karantzalis, A.E. Al-Co alloys prepared by vacuum arc melting: Correlating microstructure evolution and aqueous corrosion behavior with Co content. *Metals* **2016**, *6*, 46. [[CrossRef](#)]



© 2020 by the authors. Licensee MDPI, Basel, Switzerland. This article is an open access article distributed under the terms and conditions of the Creative Commons Attribution (CC BY) license (<http://creativecommons.org/licenses/by/4.0/>).

Article

# Influence of Continuous Casting Speeds on Cast Microstructure and Mechanical Properties of an ADC14 Alloy

Yoon-Seok Lee <sup>1,\*</sup>, Yuya Makino <sup>1</sup>, Jun Nitta <sup>1</sup> and Eunkyung Lee <sup>2</sup>

<sup>1</sup> Graduate School of Natural Science and Technology, Okayama University, Okayama 700-0082, Japan; po507fwv@s.okayama-u.ac.jp (Y.M.); p8177t18@s.okayama-u.ac.jp (J.N.)

<sup>2</sup> Department of Ocean Advanced Materials Convergence Engineering, Korea Maritime and Ocean University, Busan 49112, Korea; elee@kmou.ac.kr

\* Correspondence: y\_lee@okayama-u.ac.jp; Tel.: +81-80-3332-4770

Received: 31 March 2020; Accepted: 8 May 2020; Published: 11 May 2020

**Abstract:** To improve the mechanical properties of the casting alloys, various attempts have been made to use alternative casting technologies. The Ohno continuous casting (OCC) process is a unidirectional solidification method, which leads to high-quality cast samples. In this study, the Al-Si-Cu-Mg alloy was cast at casting speeds of 1 mm/s, 2 mm/s, and 3 mm/s, by the OCC process. The aim of this study is to investigate the effects of the casting process parameters, such as casting speeds and cooling conditions, on the crystallization characteristics and mechanical properties of OCC-Al-Si-Cu-Mg alloy. Particularly, secondary dendrite arms spacing of  $\alpha$ -Al dendrites in OCC samples significantly decreases with increasing casting speed. Moreover, the mean tensile strength of the samples, produced at the highest casting speed of 4.0 mm/s, is significantly higher than that for the samples produced at a casting speed of 1.0 mm/s.

**Keywords:** aluminum alloy; casting speed; solidification; Ohno continuous casting; gravity casting; dendritic spacing

## 1. Introduction

The reductions in automotive exhaust greenhouse gases, such as carbon dioxide (CO<sub>2</sub>) and nitrogen oxides (NO<sub>x</sub>), are strongly required for environmental reasons. Light-weighting of vehicles presents an opportunity for cutting greenhouse gas emissions. Aluminum (Al) alloys are one of the light weighting automotive materials, which meets vehicle safety and performance requirements [1]. Therefore, automotive parts made of heavy steel have been replaced with Al alloys. Particularly, the hypereutectic Al-Si alloy family is widely used in the automotive industry because of its high strength, good castability, and low density.

The Al-Si-Cu-Mg alloy, used in this study, is particularly the commercial hypereutectic Al-Si<sub>16</sub>-Cu<sub>4</sub>-Mg<sub>0.6</sub> alloy (JIS (Japanese Industrial Standards) ADC14). This Al-Si-Cu-Mg alloy has been also widely used for various automotive parts, such as linerless engine blocks, pistons, pumps, and compressors. Furthermore, there has been increasing use in the cast Al-Si-Cu-Mg alloy for automotive parts, over the world. The cast Al-Si-Cu-Mg alloy microstructure consists of mainly coarse  $\alpha$ -Al, primary silicon (Si), and needle-shaped eutectic phases, which significantly affects the mechanical properties of Al-Si-Cu-Mg alloy [2]. In particular, it should be noted that the mechanical properties of Al-Si-Cu-Mg alloy are also directly affected by  $\alpha$ -Al dendrite size, as indicated by dendrite arms spacing (DAS). However, the use of this Al-Si-Cu-Mg alloy, to replace heavy steel in automotive industry, has been restricted because of their lower strength and lower ductility.

Al-Si alloy family has been investigated using a unique continuous casting technique proposed by Ohno, which is known as the Ohno continuous casting (OCC) process. The OCC process is a unidirectional solidification method, and this casting process provides phase control and texture control [3], which can lead to easy control of microstructure size [4] and crystal orientation [5]. Some researchers have investigated the mechanical properties of OCC-Al alloys, showing excellent tensile and fatigue properties. This can be explained by that their unidirectional microstructures, low defect density, and uniformly oriented lattice structure [6–8]. Therefore, it is believed that the OCC process is useful in the automotive industry.

These days, a better understanding of how alloy solidifies at different casting conditions, involving cooling rates is required in order to improve mechanical properties of cast Al-Si-Cu-Mg alloys as automotive parts. However, very little investigation has been reported, which includes the interpretation of cooling conditions and mechanical properties for the OCC-Al-Si-Cu-Mg alloy on a metallurgical basis.

Therefore, the Al-Si-Cu-Mg samples were cast at casting speeds of 1 mm/s, 2 mm/s, 3 mm/s, and 4 mm/s via the OCC process in this study. In addition, the influences of microstructures, such as  $\alpha$ -Al phases, primary Si, and DAS on the mechanical properties of cast Al-Si-Cu-Mg alloys were investigated. The aim of this work is to investigate the effects of casting speeds and cooling conditions on the  $\alpha$ -Al dendritic grains-growing and tensile properties of OCC-Al-Si-Cu-Mg alloy.

## 2. Experimental Procedure

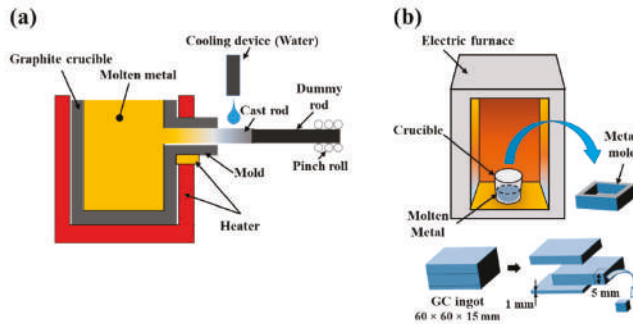
### 2.1. Materials

Table 1 shows the chemical compositions of Al-Si-Cu-Mg alloy used in this study. The Al-Si-Cu-Mg samples were prepared by the OCC process. In this study, the samples were also prepared by the gravity cast (GC) process for comparison with the OCC process. Figure 1a shows a schematic drawing of a horizontal-type OCC arrangement, consisting of a melting furnace, a heated graphite mold with a diameter of 5 mm, a graphite crucible, a cooling device, and a dummy rod for withdrawal of the cast sample. Approximately 0.4 kg of Al-Si-Cu-Mg ingot was placed in the graphite crucible for melting, with the graphite mold heated to approximately 910 K, which is just above the liquidus of the Al-Si-Cu-Mg alloy. The melted Al alloy in the crucible was fed continuously into the mold through a runner. A schematic drawing of conventional GC arrangement, consisting of an electric furnace, a crucible, and a metal mold, is shown in Figure 1b for comparison. The Al-Si-Cu-Mg ingot was also placed and melted in the crucible at approximately 910 K for 1 h, using the electric furnace. Then the molten alloy was solidified in the wide rectangular mold.

To obtain various microstructural characteristics, the casting operation of the OCC process was carried out at different speeds, from 1.0 mm/s to 4.0 mm/s. In this study, the round-rod samples were produced via the OCC process with a diameter of 5 mm and a length of approximately 1 m.

**Table 1.** Chemical composition (mass%) of the Al-Si-Cu-Mg alloy used in this study.

Alloy \ Element	Cu	Si	Mg	Zn	Fe	Mn	Al
Al-Si-Cu-Mg	4.20	16.49	0.61	0.37	0.72	0.31	bal.



**Figure 1.** Schematic drawings of (a) vertical Ohno continuous casting (OCC) and (b) gravity cast (GC) process.

## 2.2. Metallurgical Analysis

Some of the OCC and GC samples were sectioned to observe microstructures using optical microscope (OM). The cut surfaces were first metallographically polished using up to a 4000 grit-sized silicon carbide paper and were subsequently buff-polished using an  $\text{Al}_2\text{O}_3$  powder with an average diameter of  $0.3 \mu\text{m}$  and a colloidal  $\text{SiO}_2$  solution.

The DAS were also investigated from optical micrographs of cross-section of the cast samples. In particular, the secondary dendrite arms spacing (SDAS) was determined by several optical micrographs and applying an image analysis software. The total spacing from the first to the last arm in a certain area was firstly measured to calculate the SDAS. Consequently, the SDAS was obtained from the following equation:

$$\text{SDAS} = L / (n \times V), \quad (1)$$

where  $L$  is the measuring length in  $\mu\text{m}$ ,  $n$  is the number of existing dendrite arms in a certain area, and  $V$  is the micrograph magnification. Then, an average value of the results was calculated after repeated measurements in different areas.

In addition, some of the cast rod was sectioned parallel to the withdrawal direction and scanning electron microscope (SEM)-based electron back-scattered diffraction (EBSD) analysis was performed to develop a more quantitative view of the microstructures. The cut surfaces were also buff-polished and the orientation data obtained from the EBSD scans were analyzed using an Orientation Imaging Microscopy (OIM<sup>TM</sup>) analysis software (version 7.2, EDAX Inc., Mahwah, NJ, USA). Moreover, after the tensile tests, the fracture surfaces were also observed to analyze the material defects, using SEM.

## 2.3. Mechanical Properties

The hardness of longitudinal cross-sections of OCC samples was measured using a Vickers hardness tester at a load of 9.8 N for a holding time of 15 s. The hardness of GC samples was also measured under the same conditions. Nine different points were measured for each sample. The highest and lowest values were discarded, and the hardness of each sample was determined using the average of the remaining seven values.

Moreover, the tensile tests were carried out using an electro-servo-hydraulic system with a crosshead speed of 1 mm/min in air at room temperature. Dumbbell-shaped round specimens (4 mm in diameter and 30 mm in length) were used as shown in Figure 2. The three specimens were prepared and tested for each tensile test. Load and strain were measured using a load cell attached to the machine and a foil-type strain gage attached to the gage section of the specimens, respectively. The tensile strength and strain of the specimens were obtained from the tensile stress–strain curve.

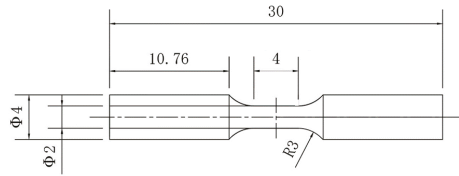


Figure 2. Schematic drawing of specimen used for tensile test.

### 3. Results

#### 3.1. Microstructural Characteristics

Figure 3 shows optical micrograph of cross-section of sample produced by GC. The microstructure basically consists of large primary Si, embedded between primary  $\alpha$ -Al grains. Moreover, Figure 4 shows optical micrographs of cross-sections of OCC samples produced at casting speeds of 1.0, 2.0, 3.0, and 4.0 m/s. The microstructures of OCC samples also consist of large primary Si, embedded between primary  $\alpha$ -Al grains. It can be also clearly observed that the mean sizes of primary Si are the largest at a speed of 1.0 mm/s, regardless of the observed location.

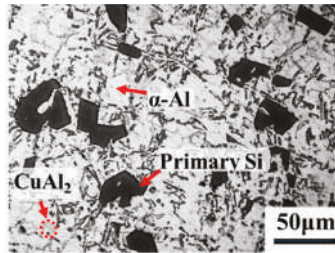


Figure 3. Optical micrograph showing microstructure of GC sample.

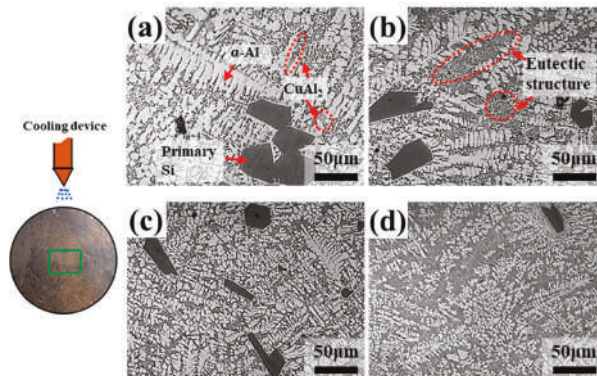
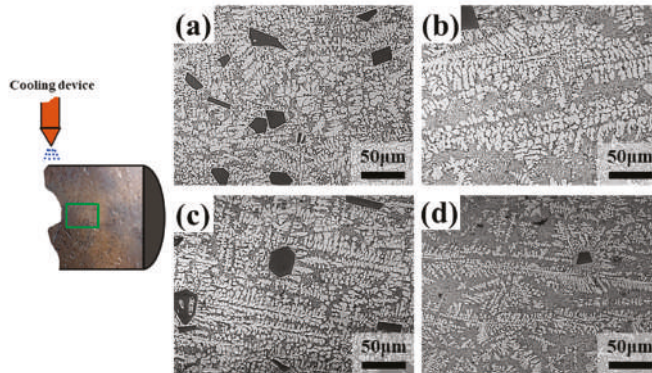


Figure 4. Optical micrographs of cross-sections of OCC samples; middle parts cast at speeds of (a) 1.0 mm/s, (b) 2.0 mm/s, (c) 3.0 mm/s, and (d) 4.0 mm/s.

Figure 4 shows middle parts of cross-sectioned OCC samples. In this study, no sharp difference is observed between upper and lower parts of the samples at any of the casting speeds, although upper parts were cooled directly by spray water and cooled at the fastest rate (Figure 1a). It can be explained by that the diameter of cast rod is too small to show large difference in the cooling rate, between upper and lower parts.

Moreover, it is observed that the grain structure transition occurs with increasing casting speeds, owing to the different cooling rates. The morphologies of primary Si phases show sharp edges and flat faces, indicating the facet characteristics. Furthermore, the distributions of primary Si phases are non-homogenous, regardless of the casting speeds. In particular, both the sizes and amount of primary Si are reduced between 1.0 mm/s and 2.0 mm/s. Larger primary Si particles (approximately 5–100  $\mu\text{m}$  in equivalent diameter) are observed in the samples cast at a lowest speed (1.0 mm/s), while smaller primary Si particles (approximately 5–40  $\mu\text{m}$  in equivalent diameter) are observed at the other speeds (2.0 mm/s, 3.0 mm/s, and 4.0 mm/s).

In addition, optical micrographs of longitudinal cross-sections are also shown in Figure 5. It is clear from the results at higher casting speeds (Figure 5b–d) that the  $\alpha$ -Al dendrite cells grow in the withdrawal direction. No sharp difference was also observed between upper and lower parts of cast samples, regardless of the casting speeds. The grain structure transition is also observed in longitudinal cross-sections with changes in casting speeds. The quantitative analysis of dendritic structures can be conducted by measurements of DAS. As shown in Figure 5, it is clearly observed that the dendritic structures are refined with increasing casting speed. It is considered that higher cooling rates during solidification induce a higher degree of refinement in dendritic array.



**Figure 5.** Optical micrographs of longitudinal cross-sections of OCC samples; middle parts cast at speeds of (a) 1.0 mm/s, (b) 2.0 mm/s, (c) 3.0 mm/s, and (d) 4.0 mm/s.

EBSD analysis was also carried out in order to analyze morphologies of the dendritic structures, including SDAS. All observations were obtained from longitudinal cross-sections of the samples as shown in Figure 6. It can be more clearly observed from both image quality (IQ) maps and corresponding grain boundary (GB) maps that SDAS of  $\alpha$ -Al dendrites significantly decreases with increasing casting speed. SDAS is one of the most important factor, which affects the mechanical properties of Al-Si alloy family. The effects of SDAS and grain size on mechanical properties are similarly obtained for the related Al-Si alloys [9]. Figure 7 shows the relationship between the casting speeds and SDAS. SDAS of  $\alpha$ -Al dendrites in OCC samples significantly decreases with increasing casting speed. Moreover, SDAS of OCC samples is smaller than that in GC samples, regardless of the casting speed. The mean SDAS is approximately 4.0  $\mu\text{m}$  for the high casting speed of 4.0 mm/s and 8.7  $\mu\text{m}$  for the low casting speed of 1.0 mm/s, resulting from the longitudinal cross-sections. It is considered that the changes in SDAS are due to a different cooling rate, which lead to different solidification behavior.

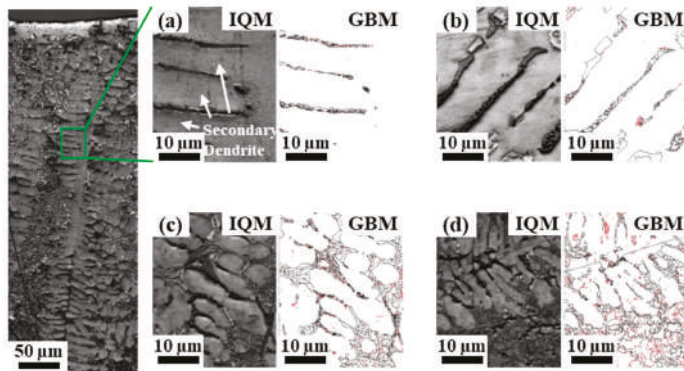


**Figure 6.** Electron back-scattered diffraction (EBSD) analysis of longitudinal cross-sections of OCC samples: image quality (IQ) maps and corresponding grain boundary (GB) maps of samples cast at speeds of (a) 1 mm/s, (b) 2 mm/s, (c) 3 mm/s, and (d) 4 mm/s.

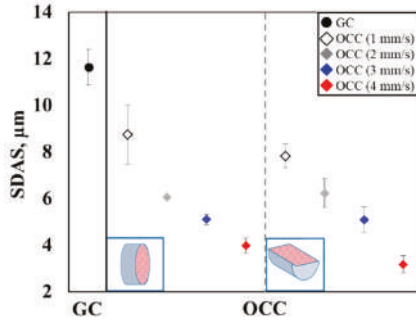


**Figure 7.** Secondary dendrite arms spacing (SDAS) of GC and OCC samples.

As shown in Figure 8, the cooling rates (CR) of the casting samples were also estimated from the following equation [10]:

$$CR = 2 \times 10^4 \times SDAS^{-2.67} \quad (2)$$

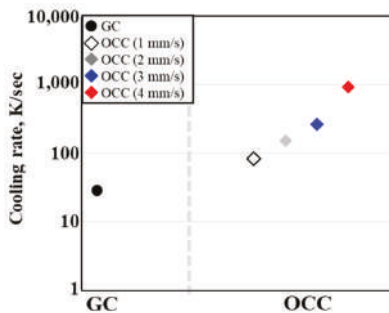


**Figure 8.** Relationship between casting rate and cooling rate for Al-Si-Cu-Mg alloys.

The cooling rates significantly increase with increasing casting speeds for OCC samples. Furthermore, the estimated cooling rates of OCC samples are higher than those of GC samples, regardless of the casting speed. It can be explained by that OCC samples have much smaller volumes with cooled directly with sprayed water.

3.2. Mechanical Properties

As shown in Figure 9, it is clearly observed that the hardness of OCC samples significantly increases with increasing casting speeds, showing similar behaviors with those of CR plotted in Figure 8. Grain boundaries generally act as barriers to dislocation motion. As mentioned in Section 3.1, the effects of SDAS and grain size on mechanical properties are similar for the Al-Si-Cu-Mg alloy. Consequently, it is considered that the refinement of SDAS, with increasing cooling rate, leads to increase in hardness. Moreover, the mean hardness of OCC samples cast at speeds over 3 mm/s exceeds that of GC sample.

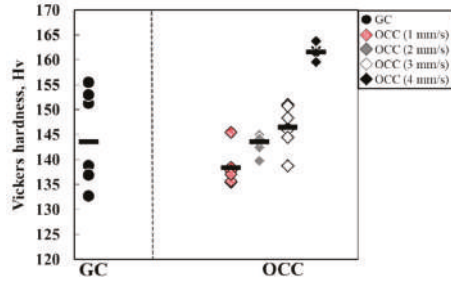


Figure 9. Vickers hardness of GC and OCC samples.

In addition, Figure 10 shows the variations of ultimate tensile strength as functions of casting speeds. It can be observed that the mean ultimate tensile strength increases at higher casting speeds. These results from the tensile tests are similar to the hardness results shown in Figure 9. The mean tensile strength shows a maximum for the samples produced at the highest casting speed of 4.0 mm/s, which is about 70% higher than that for the samples produced at a casting speed of 1.0 mm/s. Moreover, the mean tensile strength of OCC samples cast at 4.0 mm/s is also much higher (by more than 2 times) than that of the GC samples.

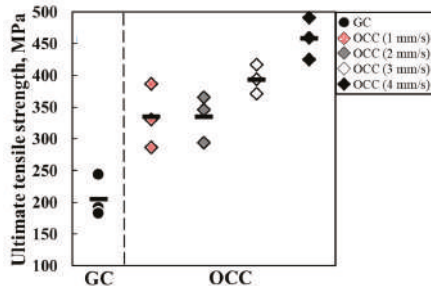


Figure 10. Ultimate tensile strength of GC and OCC samples.

The variations of fracture strain as functions of casting speeds are also shown in Figure 11. No sharp difference is observed with a changing casing speed. Nevertheless, the fracture strains of OCC samples are slightly higher compared to that of GC samples, regardless of the casting speeds.

It is believed that such improvements of mechanical properties of OCC samples can be explained by the presence of unidirectional microstructures and refined dendritic array. Particularly, the improvements of the tensile strength of OCC samples are owing to the refinement of SDAS, which may be the obstacles to the movement of dislocations. SDAS is particularly a significant factor determining the mechanical properties of cast Al-Si-Cu-Mg alloys due to grain-boundary hardening, although the mechanical properties are also affected by other microstructural characteristics, such as eutectic and Si phases.

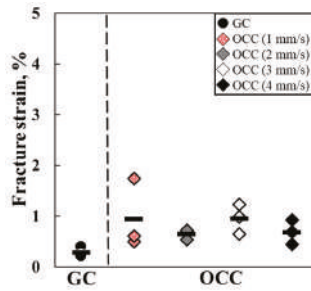


Figure 11. Fracture strain of GC and OCC samples.

SEM fractographs of the tensile specimens cast by GC and OCC are shown in Figure 12. Large pores (approximately 150  $\mu\text{m}$  in diameter) can be observed only at the fracture surface of GC samples, as shown in Figure 12a. On the other hand, from the microstructural observations, the fine casting defects (pores or inclusions) are detected in all of OCC samples. The casting defects could give rise to the stress concentration, leading to the crack formation during the tensile test [11]. It should be noted that the large pore, among the casting defects, is the most responsible for crack formation. Hydrogen (H), as the only gas capable of dissolving to significant quantities in an aluminum melt, is the main factor influencing gas porosity. It is considered that the large pore of GC sample is generated by H gas during the solidification in this study. This is because the morphology of the large pore on the fracture surface does not seem to be a shrinkage pore with an irregular shape, but a gas pore of a spherical shape [11]. It is considered that the large gas pore in the GC sample is generated by the slower cooling rate compared to the OCC samples. Furthermore, not only SDAS, but also the casting defects are smaller and better distributed at a higher casting speed. Consequently, the lower strength and ductility of GC alloys are assumed to result from not only enlarged  $\alpha\text{-Al}$  and SDAS but also internal defects in this study.

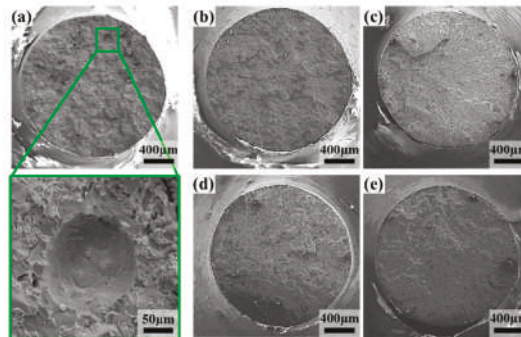


Figure 12. SEM fractographs of Al-Si-Cu-Mg samples cast by (a) GC and OCC at casting speeds of (b) 1.0 m/s, (c) 2.0 m/s, (d) 3.0 m/s, and (e) 4.0 m/s, after tensile tests.

#### 4. Summary

In this study, the effects of casting speeds and cooling conditions on the cast microstructures and mechanical properties of Al-Si-Cu-Mg alloy were investigated. The primary findings of this study are the following:

- 1) The microstructures, particularly those of the sizes of  $\alpha\text{-Al}$  grains, differ among the samples, which resulted from the different cooling rate. SDAS of  $\alpha\text{-Al}$  dendrites in OCC samples significantly

decreases with increasing casting speed. Moreover, SDAS of  $\alpha$ -Al dendrites in OCC samples is smaller than that in GC samples, regardless of the casting speed.

- 2) The improvements of mechanical properties of OCC samples are owing to the refinement of SDAS, which may be the obstacles to the movement of dislocations. The mean tensile strength shows maximum for the samples produced at the highest casting speed of 4.0 mm/s.
- 3) The large pore can be observed only at the fracture surface of GC samples. On the other hand, only fine casting defects are detected in any of OCC samples. It is believed that the presence of large pores may lead to crack formation during the tensile test.
- 4) The solidification conditions in continuous casting process, leading to the refinement of the dendritic structures and low porosity, are regarded as contributing to the higher quality of the products and mechanical properties of Al-Si-Cu-Mg casting alloy.

**Author Contributions:** Conceptualization, Y.-S.L.; methodology, Y.-S.L.; formal analysis, Y.-S.L. and Y.M.; investigation, Y.M. and J.N.; resources, Y.-S.L.; data curation, Y.-S.L. and Y.M.; writing—original draft preparation, Y.-S.L.; writing—review and editing, Y.-S.L. and E.L.; visualization, Y.-S.L.; supervision, Y.-S.L.; project administration, Y.-S.L. All authors have read and agreed to the published version of the manuscript.

**Funding:** This research received no external funding.

**Acknowledgments:** This work was supported in part by The Light Metal Educational Foundation, Inc., Japan.

**Conflicts of Interest:** The authors declare no conflict of interest.

## References

1. Kim, H.-J.; Keoleian, G.A.; Skerlos, S.J. Economic assessment of greenhouse gas emissions reduction by vehicle lightweighting using aluminum and high-strength steel. *J. Ind. Ecol.* **2011**, *15*, 64–80. [[CrossRef](#)]
2. Okayasu, M.; Takeuchi, S.; Shiraishi, T. Crystallisation characteristics of primary silicon particles in cast hypereutectic Al-Si alloy. *Int. J. Cast Met. Res.* **2013**, *26*, 105–113. [[CrossRef](#)]
3. Soda, H.; Motoyasu, G.; Mclean, A.; Jen, C.K.; Lisboa, O. Method for continuous casting of metal wire and tube containing optical fibre. *Mater. Sci. Technol.* **1995**, *11*, 1169–1173. [[CrossRef](#)]
4. Sengupta, S.; Soda, H.; Mclean, A. Microstructure and properties of a bismuth-indium-tin eutectic alloy. *Mater. Sci.* **2002**, *37*, 1747–1758. [[CrossRef](#)]
5. Okayasu, M.; Ota, K.; Takeuchi, S.; Ohfuji, H.; Shiraishi, T. Influence of microstructural characteristics on mechanical properties of ADC12 aluminum alloy. *Mater. Sci. Eng. A* **2014**, *592*, 189–200. [[CrossRef](#)]
6. Wang, Y.; Huang, H.-Y.; Xie, J.-X. Enhanced room-temperature tensile ductility of columnar-grained polycrystalline Cu–12 wt.% Al alloy through texture control by Ohno continuous casting process. *Mater. Lett.* **2011**, *65*, 1123–1126. [[CrossRef](#)]
7. Okayasu, M.; Yoshie, S. Mechanical properties of Al–Si<sub>13</sub>–Ni<sub>1.4</sub>–Mg<sub>1.4</sub>–Cu<sub>1</sub> alloys produced by the Ohno continuous casting process. *Sci. Eng. A* **2010**, *527A*, 3120–3126. [[CrossRef](#)]
8. Okayasu, M.; Takasu, S.; Yoshie, S. Microstructure and material properties of an Al–Cu alloy provided by the Ohno continuous casting technique. *J. Mater. Process. Technol.* **2010**, *210*, 1529–1535. [[CrossRef](#)]
9. Ceschini, L.; Morri, A.; Gamberini, A.; Messieri, S. Correlation between ultimate tensile strength and solidification microstructure for the sand cast A357 aluminium alloy. *Mater. Des.* **2009**, *30*, 4525–4531. [[CrossRef](#)]
10. Okayasu, M.; Ohkura, Y.; Takeuchi, S.; Takasu, S.; Ohfuji, H.; Shiraishi, T. A study of the mechanical properties of an Al–Si–Cu alloy (ADC12) produced by various casting processes. *Mater. Sci. Eng. A* **2012**, *543*, 185–192. [[CrossRef](#)]
11. Teng, X.; Mae, H.; Bai, Y.; Wierzbicki, T. Pore size and fracture ductility of aluminum low pressure die casting. *Eng. Fract. Mech.* **2009**, *76*, 983–996. [[CrossRef](#)]



© 2020 by the authors. Licensee MDPI, Basel, Switzerland. This article is an open access article distributed under the terms and conditions of the Creative Commons Attribution (CC BY) license (<http://creativecommons.org/licenses/by/4.0/>).

Article

# Analysis of Different Solution Treatments in the Transformation of $\beta$ -AlFeSi Particles into $\alpha$ -(FeMn)Si and Their Influence on Different Ageing Treatments in Al–Mg–Si Alloys

Florentino Alvarez-Antolin \*, Juan Asensio-Lozano, Alberto Cofiño-Villar and Alejandro Gonzalez-Pociño

Materials Pro Group, Department of Materials Science and Metallurgical Engineering, University of Oviedo, Independencia 13, 33004 Oviedo, Spain; jasensio@uniovi.es (J.A.-L.); UO229780@uniovi.es (A.C.-V.); gonzalezpalejandro@uniovi.es (A.G.-P.)

\* Correspondence: alvarezflorentino@uniovi.es; Tel.: +34-985181949

Received: 7 April 2020; Accepted: 7 May 2020; Published: 10 May 2020

**Abstract:** In the as-cast state, Al–Mg–Si alloys are not suitable for hot forming. They present low ductility due to the presence of intermetallic  $\beta$ -AlFeSi particles that form in the interdendritic regions during the solidification process. Homogenization treatments promote the transformation of these particles into  $\alpha$ -(FeMn)Si particles, which are smaller in size and more rounded in shape, thus improving the ductility of the material. This paper analyses the influence of various solution treatments on the transformation of  $\beta$ -AlFeSi particles into  $\alpha$ -(FeMn)Si particles in an Al 6063 alloy. Their effect on different ageing treatments in the 150–180 °C temperature range is also studied. An increase in the solution temperature favours greater transformation of the  $\beta$ -AlFeSi particles into  $\alpha$ -(FeMn)Si, dissolving a greater amount of Si, thereby having a significant effect on subsequent ageing. We found that as the dwell time at a temperature of 600 °C increases, the rate of dissolution of the Fe atoms from  $\alpha$ -(FeMn)Si particles exceeds the rate of incorporation of Mn atoms into said particles. This seems to produce a delay in reaching the peak hardness values in ageing treatments, which warrants further research to model this behaviour. The optimal solution treatment takes place at around 600 °C and the highest obtained peak hardness value is 104 HV after a 2 h solution treatment at said temperature and ageing at 160 °C for 12 h.

**Keywords:** Al–Mg–Si;  $\alpha$ -Al<sub>8</sub>(Fe<sub>2</sub>Mn)Si particles; solution treatment; ageing; dissolution of Fe; Differential Scanning Calorimetry

## 1. Introduction

Aluminium alloys usually have iron as a common impurity. The maximum equilibrium solubility of Fe in solid aluminium is very low. Thus, most Fe forms Fe-rich intermetallic compounds together with other elements, which appear as needles or sharp edges in the microstructure. Some types of Fe-rich intermetallic compounds are very harmful to mechanical properties, especially ductility [1]. The particles present in Al–Mg–Si alloys during solidification are mostly  $\beta$ -AlFeSi (generally the  $\beta$ -Al<sub>5</sub>FeSi phase),  $\alpha$ -AlFeSi (generally the  $\alpha$ -Al<sub>8</sub>Fe<sub>2</sub>Si phase) and Mg<sub>2</sub>Si [1–3]. These alloys are not suitable for hot forming processes in the as-cast state or in processes of intensive deformation, as occurs in extrusion. Their ductility is too low, mainly due to the presence of intermetallic  $\beta$ -AlFeSi particles that locate at interdendritic regions, giving rise to the occurrence both inside the  $\alpha$ -Al grains and at their grain boundaries after solidification is completed [4]. These particles usually have an acicular morphology in the polished plane. Hot ductility is impaired by the presence of these particles, decreasing significantly as their content increases. The purpose of the high-temperature

homogenization process is the chemical homogenization of the dendrites, as well as the simultaneous fragmentation of the  $\beta$ -Al<sub>5</sub>FeSi precipitates, thus avoiding their continuity along the grain boundaries and favouring their conversion into  $\alpha$ -Al(FeMn)Si particles with rounded edges, which increase ductile behaviour. This conversion must be complete in hot extrusion processes, as they take place in a single stage with intensive deformation and in a very short time. Hot rolling processes that obtain flat rolled products and multi-pass hot strip mills enable the decrease in temperatures and homogenization times without completing the total transformation of  $\beta$  particles into  $\alpha$  particles.  $\beta$ -AlFeSi particles can lead to local crack initiation and induce surface defects on the extruded material. The more rounded  $\alpha$ -Al(FeMn)Si particles in the homogenized material improve the extrudability of the material as well as the surface quality of the extruded material [5]. The morphology of the Fe-rich phase is related to many factors, such as the composition of the alloy, the cooling rate, and the content of Fe. During solidification, for example,  $\alpha$ -Al<sub>8</sub>Fe<sub>2</sub>Si tends to form at higher cooling rates than  $\beta$ -Al<sub>5</sub>FeSi [6]. The presence of Mn can change the morphology of the acicular Fe-rich phase and form a granular intermetallic  $\alpha$ -Al(MnFe)Si phase [7,8]. The formation of the  $\beta$ -AlFeSi particles is prior to, or at least concurrent with, the solidification of the alloy, which is why these precipitates are found in the interdendritic regions. The same grain can eventually encompass several dendrites. Therefore, these particles can appear inside the grains. As a result, the above processes lead to an increase in hot ductility [9]. A homogenization heat treatment promotes the transformation of these needle-like particles into smaller particles with more rounded shapes denoted as  $\alpha$ -(FeMn)Si,  $\alpha$ -Al<sub>8</sub>(FeMn)<sub>2</sub>Si or  $\alpha$ -Al<sub>12</sub>(FeMn)<sub>3</sub>Si [5], which allows an enhancement in the ductility of the material [9–14]. The main force inducing the transformation of the  $\beta$  particles into  $\alpha$  particles is found in the difference of Fe concentration between the Al matrix and the  $\beta$  particles themselves. It has been found that an Fe content in the alloy between 0.15% and 0.25% favours the appearance of smaller volume fractions of  $\beta$  intermetallics during solidification and promotes fine acicular morphologies, favouring a faster  $\beta \rightarrow \alpha$  transformation [15]. Moreover, the Mn in turn modifies this inducing force by causing variations in the concentration of Fe in the matrix and  $\beta$  interfaces. Kuijpers et al. determined that the optimal rate of transformation of  $\beta$  particles into  $\alpha$  particles occurs when the manganese concentration falls within the 0.02% to 0.2% range [16]. With an increase in solution time, the acicular morphology of the  $\beta$ -AlFeSi particles can be transformed into rounded shapes and the  $\alpha$ -Al<sub>8</sub>(FeMn)<sub>2</sub>Si phase can be formed. A minimal amount of Mn is needed to promote this transformation. The desirable Mn/Fe ratio could be around 0.5. The  $\alpha$ -(FeMn)Si particles present an Fe/Si atomic ratio that is higher than that of its homologous  $\beta$  phase. Therefore, the solid solution of Si in the matrix phase accordingly increases, favouring subsequent hardening via an ageing treatment [12,17]. Lui et al. concluded that the (Fe + Mn)/Si atomic ratio remains constant in homogenization treatments within the 550–580 °C temperature range [18]. In addition to the aforementioned objectives, the homogenization treatment also aims to reduce the microsegregation produced during non-equilibrium solidification and endow the material with a fine, homogeneous structure of precipitates that ensures its subsequent manufacture. The final mechanical properties are determined by the solution heat treatment, quench rate and ageing heat treatment employed. In the solution heat treatment, the aim is to dissolve the phases containing Mg and Si. The temperatures employed in these alloys usually fall within the 460–530 °C range [19]. Chen et al. placed the optimal treatment at 520 °C for 3.5 h [20]. The ageing of these alloys begins with the formation of clusters in the Guinier–Preston (GP) zones followed by sequential precipitation of the  $\beta''$  phase and other metastable phases until precipitation of the  $\beta$  equilibrium phase is achieved [21]. The high level of saturation and high concentration of voids that the  $\alpha$ -Al phase presents after quenching promotes the rapid formation of Si clusters and/or GP zones. These clusters have a high concentration of solute and maintain absolute coherence with the matrix, although elastic stresses are induced around them due to the difference in size between the atoms of the solute and those of the solvent. At this point, there is an increase in hardness, as these clusters/zones constitute a major obstacle to the displacement of dislocations [22,23]. Transition precipitates that are coherent with the matrix may nucleate from these zones. The increase in strength is defined by the size of the precipitates, their distribution, and their

coherence with the matrix. In these alloys, the precipitate responsible for hardening is the  $\beta''$  (associated with the  $Mg_2Si$  phase) [22–25]. It was found that the width of the precipitate-free zones (PFZs) was significant and optimal precipitation was associated with low thickness [26,27]. The temperatures used in the solubilization treatment and the dwell times at these temperatures seem to have a significant influence on the strength obtained after the ageing treatment. An increase in the temperature or dwell times at the aforementioned temperatures seems to favour an increase in strength after ageing [19,28]. Nandy et al. managed to obtain a peak hardness value of 90 HV by ageing at 175 °C for around 8 h, after a solution treatment at 525 °C for 2 h [29]. Yuksel obtained a maximum hardness value of nearly 100 HV by means of a solution treatment at 535 °C for 2 h and ageing at 204 °C for 2 h [25]. Note that the greatest decrease in hardness due to over-ageing was obtained at this same temperature compared to lower ageing temperatures. Several authors concluded that the rate of cooling prior to ageing and after the solubilization treatment seems to influence the peak hardness value after the ageing treatment. This cooling rate should be as high as possible in order to achieve the maximum supersaturation of Si and Mg in solid solution [24,30–32]. The most sensitive temperature range at industrial cooling rates seems to be between 450 and 250 °C [24,31,33]. Prolonged solubilization treatments are necessary in order to ensure the total dissolution of the  $Mg_2Si$  formed in the cooling after chemical homogenization. As a form of validation, it is likewise necessary to employ a cooling rate which is fast enough to avoid the premature precipitation of  $Mg_2Si$ . This would allow the full potential of structural hardening to be available in the subsequent ageing process.

The aim of this paper is to analyse the influence of various solution treatments, employing quenching in water, on the transformation of the  $\beta$ -AlFeSi particles in an Al 6063 alloy into  $\alpha$ -(FeMn)Si particles and their possible influence on different ageing treatments carried out in the 150–180 °C range.

## 2. Materials and Methods

One hundred twenty specimens were taken from the intermediate zone of the radius of a number of 200-mm-diameter slabs in the as-cast state. Table 1 shows the chemical composition of the as-cast material. These slabs were manufactured by continuous casting in discontinuous processes, with cooling and lubrication by demineralized water in the die. The round aluminium products had an approximate diameter of 228 mm and a length of 12 m. The cooling rates measured at the centre of these products were 1 K/s, and 20 K/s at the surface. The specimens had a cubic geometry measuring 12–15 mm per side. One hundred sixteen of these specimens were subjected to four solution treatments, employing three different ageing temperatures for each. Quenching in water at 15 °C was used after the solution treatments. Figure 1 outlines the experimental work carried out. The 120 specimens were distributed as follows:

- (1) 108 specimens were used to obtain the hardness profiles: 4 different solution treatments were carried out, employing 3 ageing treatments per solution treatment, with a total of 9 specimens in each ageing treatment.
- (2) 8 specimens had no ageing. There were 2 specimens after each solution treatment, one was used for metallographic inspection and calculation of the material's hardness, while the other was used for differential scanning calorimetry (DSC).
- (3) The remaining 4 specimens were analysed in the as-cast state.

**Table 1.** Chemical composition (% by weight).

%Si	%Fe	%Cu	%Mg	%Mn	%Ti
0.42	0.22	0.018	0.47	0.031	0.019

Metallographic inspection was carried out using an optical microscope and a scanning electron microscope. Preparation of the metallographic specimens was carried out by cutting with a SiC disc, cold mounting with an epoxy resin, grinding with SiC paper of different abrasive grain sizes ranging

from grit 240 to 600 then finally polishing in three steps with textile cloths using different types of abrasives in each step. In the first step, 6 and 1  $\mu\text{m}$  diamond paste was used, while a 0.5  $\mu\text{m}$  alumina solution in distilled water was used in the second step. In the third stage, a 0.05  $\mu\text{m}$  colloidal silica solution, which was also in distilled water, was utilized.

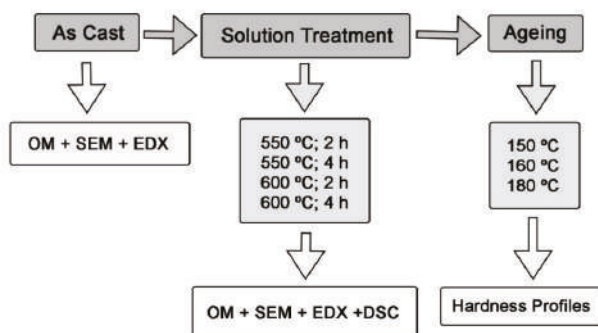


**Figure 1.** Outline of the experimental work carried out. OM: optical microscopy; DSC: differential scanning calorimetry; EDX: energy dispersive X-ray spectroscopy; SEM: scanning electron microscopy.

The etching reagents used in the optical microscopy analysis were:

- (1) 2 mL HF, 3 mL HCl, 5 mL HNO<sub>3</sub> and 190 mL distilled water.
- (2) A solution made of 4 g KMnO<sub>4</sub>, 1 g NaOH and 100 mL distilled water. This reagent reveals the chemical heterogeneities derived from dendritic microsegregation.

The optical microscope used was a NIKON Epiphot 200 (Nikon, Tokyo, Japan) and the images were obtained using Beuhler Omnimet Enterprise image analyser software (5.0, Beuhler, Lake Bluff, USA). The scanning electron microscope employed was a JEOL JSM-5600 (JEOL, Nieuw-Vennep, The Netherlands). The Fe/Si atomic ratio in the  $\alpha$ -Al(FeMn)Si particles was determined on metallographic samples in the polished state, without etching with a chemical reagent. Energy dispersive X-ray (EDX) microanalysis was used for this purpose, randomly analysing 30 particles per specimen (20 kV with reflections of up to 10 keV).

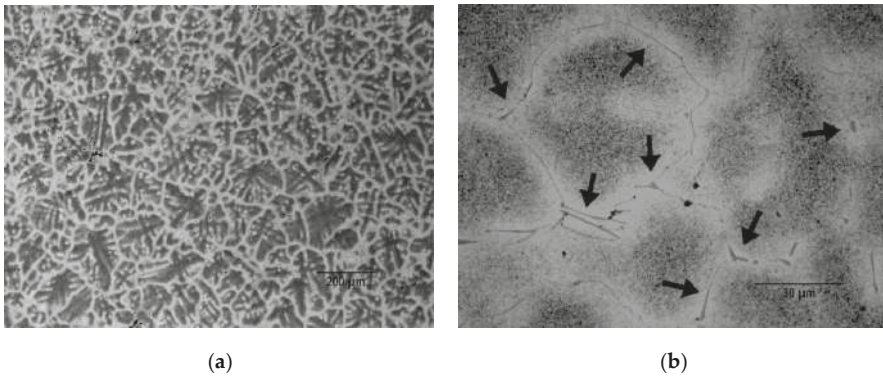
Vickers hardness values were obtained under the application of a 300 N load. The results correspond to the mean value obtained from 12 indentations per specimen.

The differential scanning calorimeter used was a Mettler Toledo DSC 822e (Mettler Toledo, Schwerzenbach, Switzerland). The heating rate was 10 °C/min, and the test was conducted between 25 and 500 °C. The results obtained by DSC will not provide us with the isothermal temperature at which the precipitation of the metastable phases that cause structural hardening takes place. During the DSC test, these temperatures are obtained by means of a heating ramp and are therefore always higher than the temperatures used isothermally for artificial ageing. However, when the aim is to compare various ageing treatments, this test allows us to compare whether said precipitation of structural hardening will occur sooner or later.

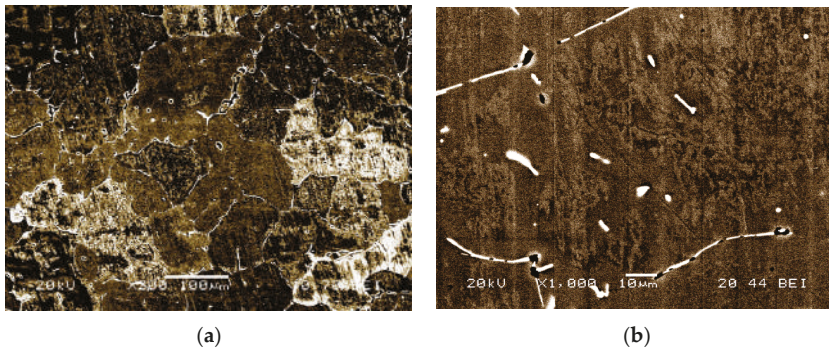
### 3. Results

Figure 2 shows the microstructure obtained in the as-cast state. It can be seen that the microstructure presents dendritic segregation and precipitation of  $\beta$ -Al<sub>5</sub>FeSi particles in the segregated zones, preferably at the grain boundaries. Figure 3 shows images of this microstructure obtained using electron channelling contrast imaging (ECCI) [34]. The elongated, acicular morphology of the  $\beta$ -Al<sub>5</sub>FeSi particles can be observed, forming a more or less continuous network through the grain boundaries network of the  $\alpha$ -Al phase. It can also be seen that the grain size is around 200–250  $\mu\text{m}$ . Figure 4 shows

the microstructure obtained following the solution treatments with cooling in water. A homogenized microstructure can be seen in all cases, with no dendritic segregation. A decrease in the volume fraction of AlFeSi particles and loss of their continuity were likewise observed. Figure 5 shows the transformation of the microstructure during the homogenization treatment. Figure 5a shows the microstructure obtained in the as-cast state. The  $\beta$ -Al<sub>5</sub>FeSi particles and the Mg<sub>2</sub>Si phase can be observed, both located at a grain boundary. Figure 5b shows the microstructure after solubilization at 600 °C, employing cooling in water. This treatment also allows the solubilization of the Mg<sub>2</sub>Si phase and the transformation of the  $\beta$ -Al<sub>5</sub>FeSi particles into  $\alpha$ -Al<sub>8</sub>(FeMn)<sub>2</sub>Si particles. Cooling in water prevented solid-state precipitation of Mg<sub>2</sub>Si.



**Figure 2.** Microstructure in the as-cast state. (a) Dendritic segregation is observed; (b)  $\beta$ -Al<sub>5</sub>FeSi particles at the grain boundaries. The etching reagent consisted of a solution of 100 mL distilled water with 4 g KMnO<sub>4</sub> and 1 g NaOH.



**Figure 3.** Microstructure in the as-cast state obtained under a scanning electron microscope (SEM) using electron channelling contrast imaging (ECCI). (a) It can be seen that the grain size can be estimated to be around 200–250  $\mu$ m. (b) The  $\beta$ -Al<sub>5</sub>FeSi particles are in white and Mg<sub>2</sub>Si particles are in black.

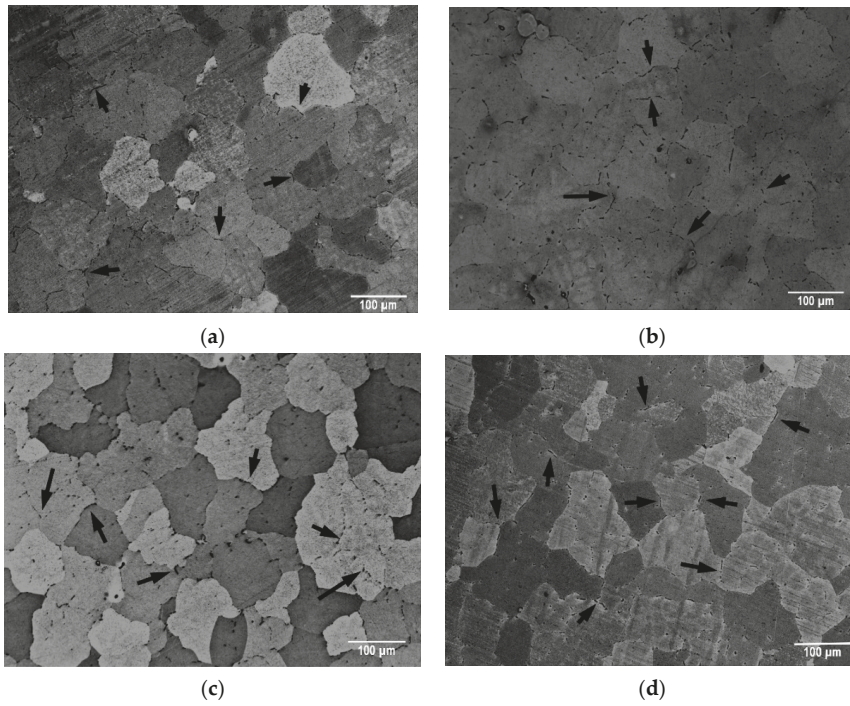


**Figure 4.** Microstructure after solution treatments, employing quenching in water. (a) Treatment at 550 °C for 2 h. (b) Treatment at 550 °C for 4 h. (c) Treatment at 600 °C for 2 h. (d) Treatment at 600 °C for 4 h.

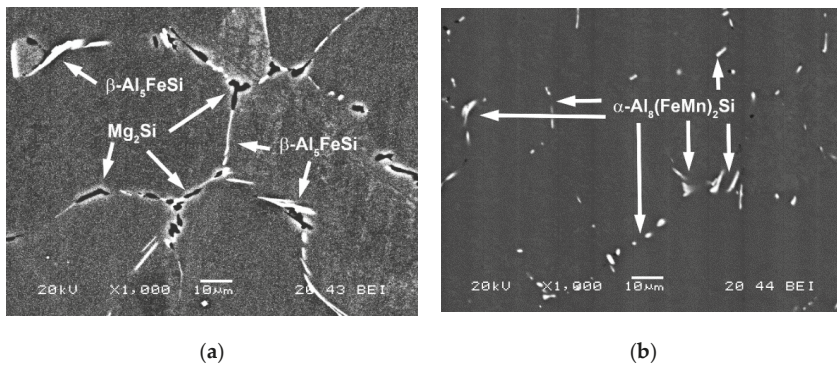


**Figure 5.** Microstructures obtained by scanning electron microscopy (SEM). (a) The as-cast state. The  $\beta$ - $\text{Al}_5\text{FeSi}$  particles and the  $\text{Mg}_2\text{Si}$  phase can be observed, located at a grain boundary. (b) After a solubilization treatment at 600 °C with water cooling, which enabled the maximum solubilization of the  $\text{Mg}_2\text{Si}$  phase and the transformation of the  $\beta$ - $\text{Al}_5\text{FeSi}$  particles into  $\alpha$ - $\text{Al}_8(\text{FeMn})_2\text{Si}$  particles.

Figure 6 shows the Fe/Si atomic ratio and the atomic percentage of Mn in the  $\alpha$ -Al(FeMn)Si particles, while Figure 7 shows the (Fe + Mn)/Si ratio, along with the atomic percentages of Si and Fe. It can be observed that the Fe/Si ratio was higher in treatments at 600 °C than in treatments at 550 °C, a finding that could be justified by the greater dissolution of Si atoms at 600 °C. This would allow an increase in the potential for structural hardening. However, this ratio decreased when the

duration of the treatment was 4 h. Note that the atomic % of Fe in the  $\alpha$  particles was much lower in the treatments at 600 °C, being lower with dwell times of 4 h versus 2 h. Moreover, the  $\beta$ -AlFeSi particles in the as-cast state do not contain Mn atoms. However, as the dwell times of the treatment temperature increased, the atomic content of Mn in the  $\alpha$ -Al(FeMn)Si particles also increased.

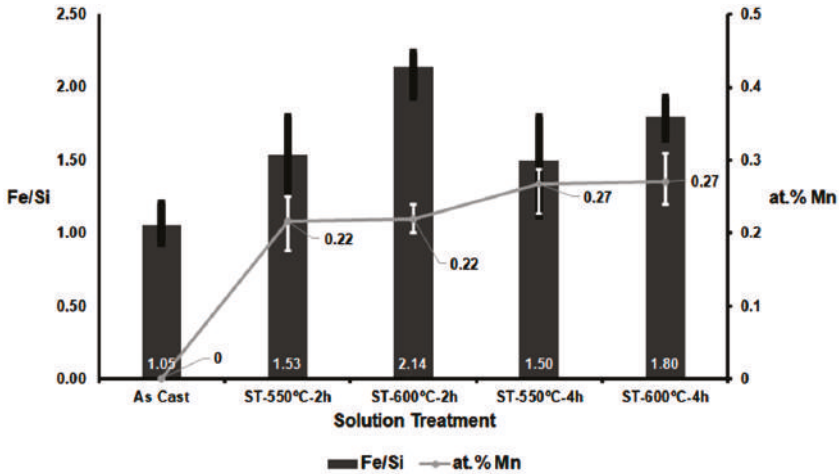


Figure 6. Mean Fe/Si atomic ratio of AlFeSi particles after the different solution treatments (ST). The results are correlated with the atomic % of Mn in these particles. The “As Cast” state refers to the  $\beta$ -Al<sub>5</sub>FeSi particles, while the state after the solution treatment refers to the  $\alpha$ -Al<sub>8</sub>(FeMn)<sub>2</sub>Si particles. The error bars show the distance between the mean value and the maximum and minimum values of the 30 particles analysed in each specimen.

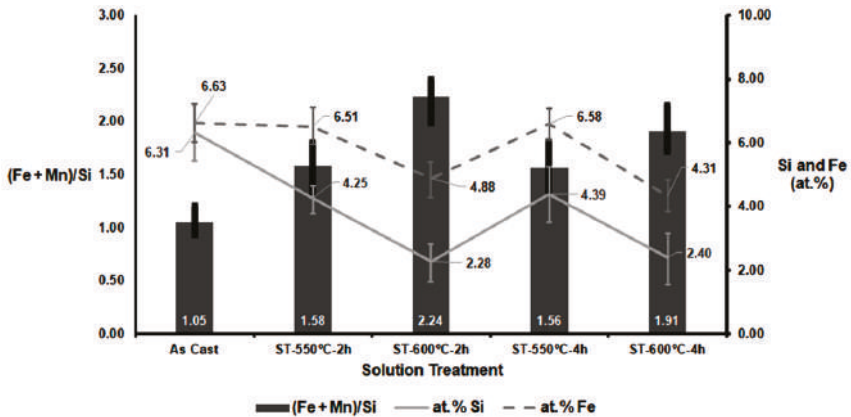
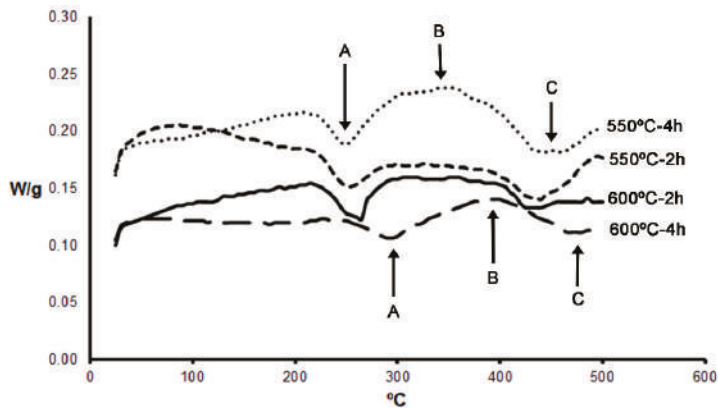


Figure 7. Mean (Fe + Mn)/Si atomic ratio of AlFeSi particles after the different solution treatments (ST). The atomic percentages of Si and Fe are also shown. The “As Cast” state refers to  $\beta$ -Al<sub>5</sub>FeSi particles, while the state after the solution treatment refers to the  $\alpha$ -Al<sub>8</sub>(FeMn)<sub>2</sub>Si particles. The error bars show the distance between the mean value and the maximum and minimum values of the 30 particles analysed in each specimen.

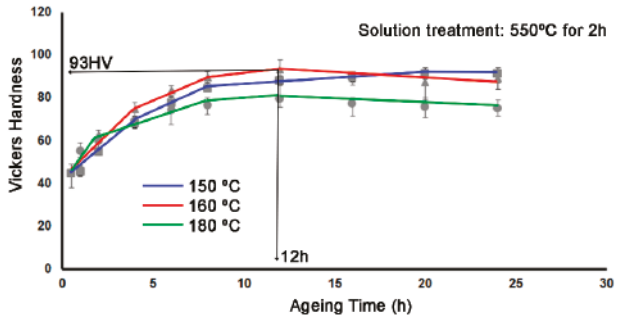
The hardness value in the as-cast state was 40 HV and the hardness value obtained after these treatments was 45 HV, with no differences in hardness being found between the different solution treatments. The hardness test was carried out immediately after these treatments.

Figure 8 shows the results obtained after the DSC analysis. Two main exothermic peaks were detected, designated as A and C. Peak A corresponds to precipitation of the  $\beta''$  and  $\beta'$  phases. In between peaks A and C is the endothermic peak B that corresponds to the dissolution of these phases. Lastly, peak C corresponds to the precipitation of the  $\beta$  phase [35–42]. The endothermic peak prior to the exothermic peak A shows the dissolution of the GP zones formed during natural ageing. The results of the DSC test provide the temperatures at which the structural hardening precipitations are verifiable when this temperature is reached by means of a heating ramp. In our case, the heating rate is 10 °C/min. This means that these temperatures cannot be compared with the isothermal ageing temperatures, the latter being necessarily lower. However, when the aim is to compare various ageing treatments, this test allows us to compare whether the structural hardening will occur sooner or later. The solution treatment at 600 °C with a dwell time of 4 h produced the greatest delay in the formation of the metastable transition phases (Peak A) and their subsequent dissolution (Peak B). This delay could be related to the dissolution of the Fe atoms that were observed in the previous solution treatment at this temperature with prolonged dwell times, which could be grounds for further investigation in this regard.

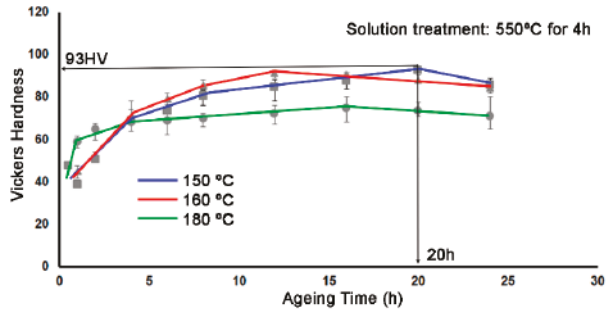


**Figure 8.** Continuous heating DSC at 10 °C/min. The samples were previously aged naturally. The exothermic peaks (A and C) indicate precipitation of the  $\beta''$ - $\beta'$  and  $\beta$  phases, respectively. The endothermic peak (B) reflects the dissolution of the  $\beta''$ - $\beta'$  phases, precipitated in A.

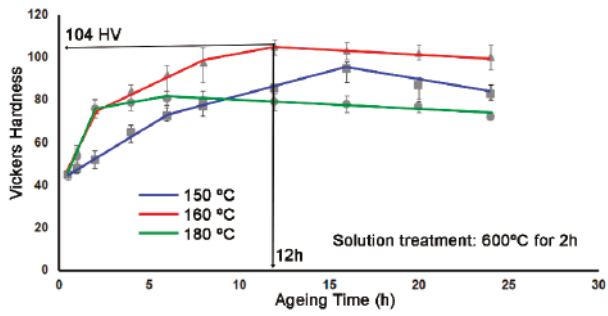
Figure 9 shows the hardness profiles obtained after the ageing treatments. The peak hardness values were obtained with solution treatments at 600 °C, which are the ones that dissolved the highest % Si from the  $\beta$ -AlFeSi particles. This would allow more Si to be available in solid solution for the subsequent precipitation of the metastable  $\beta''$  phase during ageing. The peak hardness value was 104 HV after the solution treatment at 600 °C for 2 h and ageing at 160 °C for 12 h. Very similar hardness profiles following the solution treatment at 550 °C were obtained with dwell times of 2 and 4 h. However, the peak hardness values obtained after a dwell time of 4 h at 600 °C were delayed in the three ageing temperatures compared to the 2 h dwell time. This fact may be conditioned by the dissolution of Fe atoms observed after the 4 h dwell time at 600 °C.



(a)

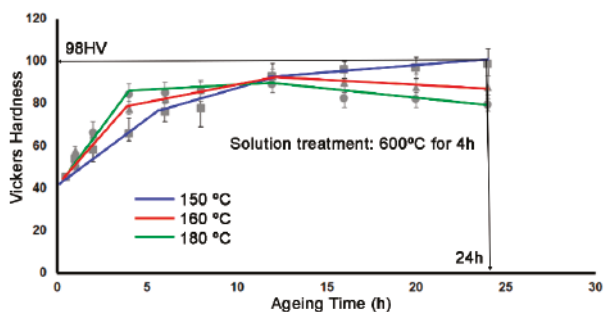


(b)



(c)

Figure 9. Cont.



(d)

**Figure 9.** Hardness profiles after the ageing treatments. (a) Treatment at 550 °C for 2 h. (b) Treatment at 550 °C for 4 h. (c) Treatment at 600 °C for 2 h. (d) Treatment at 600 °C for 4 h.

#### 4. Conclusions

This paper analyses the influence of solution treatments on the transformation of  $\beta$ -AlFeSi particles into  $\alpha$ -(FeMn)Si particles and their possible influence on different ageing treatments carried out in the 150–180 °C range. The main conclusions are:

- (1) The Fe/Si atomic ratio increased with increasing solution treatment temperature from 550 to 600 °C. This reflects a greater degree of transformation of  $\beta$ -Al<sub>5</sub>FeSi particles into  $\alpha$ -Al<sub>8</sub>(FeMn)<sub>2</sub>Si particles, and a greater potential for structural hardening.
- (2) In the transformation of  $\beta$ -Al<sub>5</sub>FeSi particles into  $\alpha$ -Al<sub>8</sub>(FeMn)<sub>2</sub>Si, a greater dissolution of both Si and Fe atoms was observed in the matrix when the solution treatment was carried out at 600 °C. The dissolution of Fe was somewhat more pronounced when the dwell times were increased from 2 to 4 h.
- (3) At a solution temperature of 550 °C, the (Fe + Mn)/Si atomic ratio remained practically constant. However, at 600 °C, this ratio decreased when the dwell time was increased from 2 to 4 h. This suggests that the rate of dissolution of Fe atoms exceeded the rate of incorporation of Mn atoms. This could lead to a delay in reaching peak hardness values during ageing at temperatures between 150 and 180 °C.
- (4) The peak hardness value obtained was 104 HV, following a solution treatment at 600 °C for 2 h and ageing at 160 °C for 12 h.

**Author Contributions:** J.A.-L. conceived and designed the investigation; A.C.-V. and A.G.-P. performed all laboratory work; F.A.-A. led the investigation, analysed the data, and wrote the paper. All authors have read and agreed to the published version of the manuscript.

**Funding:** This research received no external funding.

**Conflicts of Interest:** The authors declare no conflicts of interest.

#### References

1. Chanyathunyaraj, K.; Patakham, U.; Kou, S.; Limmaneevichitr, C. Microstructural evolution of iron-rich intermetallic compounds in scandium modified Al-7Si-0.3Mg alloys. *J. Alloy. Compd.* **2017**, *692*, 865–875. [[CrossRef](#)]
2. Hsu, C.; O'Reilly, K.A.Q.; Cantor, B.; Hamerton, R. Non-equilibrium reactions in 6xxx series Al alloys. *Mater. Sci. Eng. A-Struct. Mater. Prop. Microstruct. Process.* **2001**, *304*, 119–124. [[CrossRef](#)]

3. Sha, G.; O'Reilly, K.; Cantor, B.; Worth, J.; Hamerton, R. Growth related metastable phase selection in a 6xxx series wrought Al alloy. *Mater. Sci. Eng. A-Struct. Mater. Prop. Microstruct. Process.* **2001**, *304*, 612–616. [[CrossRef](#)]
4. Li, H.; Wang, J.Y.; Jiang, H.T.; Lo, Z.F.; Zhu, Z.F. Characterizations of precipitation behavior of Al-Mg-Si alloys under different heat treatments. *China Foundry* **2018**, *15*, 89–96. [[CrossRef](#)]
5. Kuijpers, N.C.W.; Vermolen, F.J.; Vuik, K.; van der Zwaag, S. A model of the beta-AlFeSi to alpha-Al(FeMn)Si transformation in Al-Mg-Si alloys. *Mater. Trans.* **2003**, *44*, 1448–1456. [[CrossRef](#)]
6. Gorny, A.; Manickaraj, J.; Cai, Z.H.; Shankar, S. Evolution of Fe based intermetallic phases in Al-Si hypoeutectic casting alloys: Influence of the Si and Fe concentrations, and solidification rate. *J. Alloy. Compd.* **2013**, *577*, 103–124. [[CrossRef](#)]
7. Fan, C.; Long, S.Y.; Yang, H.D.; Wang, X.J.; Zhang, J.C. Influence of Ce and Mn addition on alpha-Fe morphology in recycled Al-Si alloy ingots. *Int. J. Miner. Metall. Mater.* **2013**, *20*, 890–895. [[CrossRef](#)]
8. Wu, X.Y.; Zhang, H.R.; Zhang, F.X.; Ma, Z.; Jia, L.N.; Yang, B.; Tao, T.X.; Zhang, H. Effect of cooling rate and Co content on the formation of Fe-rich intermetallics in hypoeutectic Al7Si0.3Mg alloy with 0.5%Fe. *Mater. Charact.* **2018**, *139*, 116–124. [[CrossRef](#)]
9. Zajac, S.; Gullman, L.O.; Johansson, A.; Bengtsson, B. Hot ductility of some Al-Mg-Si alloys. *Mater. Sci. Forum* **1996**, *217*, 1193–1198. [[CrossRef](#)]
10. Bayat, N.; Carlberg, T.; Cieslar, M. In-situ study of phase transformations during homogenization of 6060 and 6063 Al alloys. *J. Phys. Chem. Solids* **2019**, *130*, 165–171. [[CrossRef](#)]
11. Sirichaivetkul, R.; Wongpinij, T.; Euaruksakul, C.; Limmaneevichitr, C.; Kajornchaiyakul, J. In-situ study of microstructural evolution during thermal treatment of 6063 aluminum alloy. *Mater. Lett.* **2019**, *250*, 42–45. [[CrossRef](#)]
12. Couto, K.B.S.; Claves, S.R.; Van Geertruyden, W.H.; Misiolek, W.Z.; Goncalves, M. Effects of homogenisation treatment on microstructure and hot ductility of aluminium alloy 6063. *Mater. Sci. Technol.* **2005**, *21*, 263–268. [[CrossRef](#)]
13. Kumar, S.; Grant, P.S.; O'Reilly, K.A.Q. Evolution of Fe Bearing Intermetallics During DC Casting and Homogenization of an Al-Mg-Si Al Alloy. *Metall. Mater. Trans. A-Phys. Metall. Mater. Sci.* **2016**, *47A*, 3000–3014. [[CrossRef](#)]
14. Zajac, S.; Hutchinson, B.; Johansson, A.; Gullman, L.O. Microstructure control and extrudability of al-mg-si alloys microalloyed with manganese. *Mater. Sci. Technol.* **1994**, *10*, 323–333. [[CrossRef](#)]
15. Asensio-Lozano, J.; Suarez-Pena, B. Quantitative analysis and morphological characterization of 6063 alloy. Microstructural and mechanical comparison between periphery and center of semi-continuous casting round billets. *Rev. De Metal.* **2012**, *48*, 199–212. [[CrossRef](#)]
16. Kuijpers, N.C.W.; Vermolen, F.J.; Vuik, C.; Koenis, P.T.G.; Nilsen, K.E.; van der Zwaag, S. The dependence of the beta-AlFeSi to alpha-Al(FeMn)Si transformation kinetics in Al-Mg-Si alloys on the alloying elements. *Mater. Sci. Eng. A-Struct. Mater. Prop. Microstruct. Process.* **2005**, *394*, 9–19. [[CrossRef](#)]
17. Osada, Y. EPMA mapping of small particles of alpha-AlFeSi and beta-AlFeSi in AA6063 alloy billets. *J. Mater. Sci.* **2003**, *38*, 1457–1464. [[CrossRef](#)]
18. Liu, C.L.; Azizi-Alizamini, H.; Parson, N.C.; Poole, W.J.; Du, Q. Microstructure evolution during homogenization of Al-Mg-Si-Mn-Fe alloys: Modelling experimental results. *Trans. Nonferrous Met. Soc. China* **2017**, *27*, 747–753. [[CrossRef](#)]
19. Gavgali, M.; Totik, Y.; Sadeler, R. The effects of artificial aging on wear properties of AA 6063 alloy. *Mater. Lett.* **2003**, *57*, 3713–3721. [[CrossRef](#)]
20. Chen, B.; Wu, Y.J.; Zhu, T.; Li, X.Y. The effects of Solid-solution on properties and microstructure of 6063 aluminum alloy. *Adv. Mater. Res.* **2014**, *881–883*, 1346–1350. [[CrossRef](#)]
21. Lang, P.; Povoden-Karadeniz, E.; Falahati, A.; Kozeschnik, E. Simulation of the effect of composition on the precipitation in 6xxx Al alloys during continuous-heating DSC. *J. Alloy. Compd.* **2014**, *612*, 443–449. [[CrossRef](#)]
22. Sjolander, E.; Seifeddine, S. The heat treatment of Al-Si-Cu-Mg casting alloys. *J. Mater. Process. Technol.* **2010**, *210*, 1249–1259. [[CrossRef](#)]
23. Siddiqui, R.A.; Abdullah, H.A.; Al-Belushi, K.R. Influence of aging parameters on the mechanical properties of 6063 aluminium alloy. *J. Mater. Process. Technol.* **2000**, *102*, 234–240. [[CrossRef](#)]

24. Milkereit, B.; Wanderka, N.; Schick, C.; Kessler, O. Continuous cooling precipitation diagrams of Al-Mg-Si alloys. *Mater. Sci. Eng. A-Struct. Mater. Prop. Microstruct. Process.* **2012**, *550*, 87–96. [[CrossRef](#)]
25. Yuksel, B. Effect of artificial aging on hardness and intergranular corrosion of 6063 Al alloy. *Pamukkale Univ. J. Eng. Sci. -Pamukkale Univ. Muhendis. Bilimleri Derg.* **2017**, *23*, 395–398. [[CrossRef](#)]
26. Liu, S.H.; Wang, X.D.; Pan, Q.L.; Li, M.J.; Ye, J.; Li, K.; Peng, Z.W.; Sun, Y.Q. Investigation of microstructure evolution and quench sensitivity of Al-Mg-Si-Mn-Cr alloy during isothermal treatment. *J. Alloy. Compd.* **2020**, *826*, 11. [[CrossRef](#)]
27. Saito, T.; Marioara, C.D.; Royset, J.; Marthinsen, K.; Holmestad, R. The effects of quench rate and pre-deformation on precipitation hardening in Al-Mg-Si alloys with different Cu amounts. *Mater. Sci. Eng. A-Struct. Mater. Prop. Microstruct. Process.* **2014**, *609*, 72–79. [[CrossRef](#)]
28. Meyveci, A.; Karacan, I.; Caligulu, U.; Durmus, H. Pin-on-disc characterization of 2xxx and 6xxx aluminium alloys aged by precipitation age hardening. *J. Alloy. Compd.* **2010**, *491*, 278–283. [[CrossRef](#)]
29. Nandy, S.; Abu Bakkar, M.; Das, D. Influence of Ageing on Mechanical Properties of 6063 Al Alloy. *Mater. Today-Proc.* **2015**, *2*, 1234–1242. [[CrossRef](#)]
30. Zohrabyan, D.; Milkereit, B.; Kessler, O.; Schick, C. Precipitation enthalpy during cooling of aluminum alloys obtained from calorimetric reheating experiments. *Thermochim. Acta* **2012**, *529*, 51–58. [[CrossRef](#)]
31. Li, H.Y.; Zeng, C.T.; Han, M.S.; Liu, J.J.; Lu, X.C. Time-temperature-property curves for quench sensitivity of 6063 aluminum alloy. *Trans. Nonferrous Met. Soc. China* **2013**, *23*, 38–45. [[CrossRef](#)]
32. Cavazos, J.L.; Colas, R. Quench sensitivity of a heat treatable aluminum alloy. *Mater. Sci. Eng. A-Struct. Mater. Prop. Microstruct. Process.* **2003**, *363*, 171–178. [[CrossRef](#)]
33. Giersberg, L.; Milkereit, B.; Schick, C.; Kessler, O. In-situ isothermal calorimetric measurement of precipitation behaviour in Al-Mg-Si alloys. *Mater. Sci. Forum* **2014**, *794–796*, 939. [[CrossRef](#)]
34. Luoh, T.; Bow, J.S.; Peng, A.; Tsai, S.Y.; Tseng, M.R. Observation of recording marks in phase-change media using scanning electron microscopy channelling contrast image. *Jpn. J. Appl. Phys. Part 1-Regul. Pap. Short Notes Rev. Pap.* **1999**, *38*, 1698–1700. [[CrossRef](#)]
35. Frock, H.; Kappis, L.V.; Reich, M.; Kessler, O. A Phenomenological Mechanical Material Model for Precipitation Hardening Aluminium Alloys. *Metals* **2019**, *9*, 1165. [[CrossRef](#)]
36. Hamdi, I.; Boumerzoug, Z.; Chabane, F. Study of precipitation kinetics of an Al-Mg-Si alloy using differential scanning calorimetry. *Acta Metall. Slovaca* **2017**, *23*, 155–160. [[CrossRef](#)]
37. Vedani, M.; Angella, G.; Bassani, P.; Ripamonti, D.; Tuissi, A. DSC analysis of strengthening precipitates in ultrafine Al-Mg-Si alloys. *J. Therm. Anal. Calorim.* **2007**, *87*, 277–284. [[CrossRef](#)]
38. van de Langkruis, J.; Vossenbergh, M.S.; Kool, W.H.; van der Zwaag, S. A study on the beta ' and beta " formation kinetics in AA6063 using differential scanning calorimetry. *J. Mater. Eng. Perform.* **2003**, *12*, 408–413. [[CrossRef](#)]
39. Ohmori, Y.; Doan, L.C.; Matsuura, Y.; Kobayashi, S.; Nakai, K. Morphology and crystallography of beta-Mg<sub>2</sub>Si precipitation in Al-Mg-Si alloys. *Mater. Trans.* **2001**, *42*, 2576–2583. [[CrossRef](#)]
40. Edwards, G.A.; Stiller, K.; Dunlop, G.L.; Couper, M.J. The precipitation sequence in Al-Mg-Si alloys. *Acta Mater.* **1998**, *46*, 3893–3904. [[CrossRef](#)]
41. Tsao, C.S.; Chen, C.Y.; Jeng, U.S.; Kuo, T.Y. Precipitation kinetics and transformation of metastable phases in Al-Mg-Si alloys. *Acta Mater.* **2006**, *54*, 4621–4631. [[CrossRef](#)]
42. Murayama, M.; Hono, K. Pre-precipitate clusters and precipitation processes in Al-Mg-Si alloys. *Acta Mater.* **1999**, *47*, 1537–1548. [[CrossRef](#)]



Article

# Simulation on the Effect of Porosity in the Elastic Modulus of SiC Particle Reinforced Al Matrix Composites

Jorge E. Rivera-Salinas <sup>1,\*</sup>, Karla M. Gregorio-Jáuregui <sup>2</sup>, José A. Romero-Serrano <sup>2</sup>, Alejandro Cruz-Ramírez <sup>2</sup>, Ernesto Hernández-Hernández <sup>3</sup>, Argelia Miranda-Pérez <sup>4</sup> and Víctor H. Gutiérrez-Pérez <sup>5</sup>

<sup>1</sup> Catedrático CONAcYT—Department of Plastics Transformation Processing, Centro de Investigación en Química Aplicada—CIQA, 25294 Saltillo, Coahuila, Mexico

<sup>2</sup> Metallurgy and Materials Department, Instituto Politécnico Nacional, Escuela Superior de Ingeniería Química e Industrias Extractivas—ESIQIE, UPALM, 07738 México D.F., Mexico; kaarlaa@gmail.com (K.M.G.-J.); romeroipn@hotmail.com (J.A.R.-S.); alex73ipn@gmail.com (A.C.-R.)

<sup>3</sup> Department of Advanced Materials. Centro de Investigación en Química Aplicada—CIQA, 25294 Saltillo, Coahuila, Mexico; ernesto.hernandez@ciqa.edu.mx

<sup>4</sup> Corporación Mexicana de Investigación en Materiales S.A. de C.V., Ciencia y Tecnología—COMIMSA, 25290 Saltillo, Coahuila, Mexico; argelia.miranda@comimsa.com

<sup>5</sup> Professional Specific Training Department. Instituto Politécnico Nacional—Unidad Profesional Interdisciplinaria de Ingeniería campus Zacatecas (UPIIZ), 98160 Zacatecas, Mexico; metalurgico2@hotmail.com

\* Correspondence: enrique.rivera@ciqa.edu.mx; Tel.: +52-844-389-830

Received: 17 February 2020; Accepted: 14 March 2020; Published: 19 March 2020

**Abstract:** Although the porosity in Al-SiC metal matrix composites (MMC) can be diminished; its existence is unavoidable. The purpose of this work is to study the effect of porosity on Young's modulus of SiC reinforced aluminum matrix composites. Finite element analysis is performed based on the unit cell and the representative volume element approaches. The reliability of the models is validated by comparing the numerical predictions against several experimental data ranging in low- and high-volume fractions and good agreement is found. It is found that despite the stress transfer from the soft matrix to the reinforcement remains effective in the presence of pores, there is a drop in the stress gathering capability of the particles and thus, the resulting effective elastic modulus of composite decreases. The elastic property of the composite is more sensitive to pores away the reinforcement. It is confirmed, qualitatively, that the experimentally reported in the literature decrease in the elastic modulus is caused by the presence of pores.

**Keywords:** Al/SiC composite; porosity in composites; finite element analysis

---

## 1. Introduction

Particles embedded in a matrix are commonly encountered in metal matrixes since they arise during melt processing by non-controlled phase changes, mechanical interaction of the melt with its surroundings, or they are added intentionally as filler material. Stiff and soft particle inclusions in a matrix have effects that could be considered adverse or beneficial in the physical and mechanical properties of the bulk matrix. For example, hard particles in steel are considered harmful and they often originate the variability of steel properties [1]. On the other hand, the incorporation of ceramic stiffer particles—e.g., SiC, SiO<sub>2</sub>, Al<sub>2</sub>O<sub>3</sub>, and WC—to matrixes such as aluminum alloys reinforce the bulk matrix and metal matrix composites (MMC) arise. Due to their high specific strength and modulus, reinforced materials can be tailored, finding applications in multiple industries such as

naval, aeronautics, automotive, and machining-tools. Moreover, MMC exhibit isotropic material properties [2].

The elastic properties of MMC depend principally on geometrical parameters: volume fraction, size distribution, shapes and stiffness of the particles, porosity, and bonding state at the interface. Studies have been conducted to elucidate the effects of particles embedded in metal matrixes [3,4], concluding that the shape of the particles influences the overall elastic response of the composite. While the particle size has no significant influence on the elastic modulus at low content of reinforcement [5,6].

For the microstructures having different phases like hard ceramic particles and pores, it is desirable to predict strength properties for the development of high-performance materials. Porosity in MMC can greatly influence the material properties and is mainly caused by manufacturing processes, thermal cycles, and both distribution and percentage particles [7–9]. For instance, enhancement of strength is affected in the interface causing crack initiation sites, which was evidenced in Hassani's study at varying milling times with different particle sizes and amounts. The visualization of porosity and voids employed specialized techniques such as nondestructive laser-ultrasonic spectroscopy where Podymova et al. [10] proposed a calibration curve for porosity evaluation as this defect compromise composite strength. Other techniques, such as neutron and synchrotron diffraction, were voids and pores are easily observed and micro stresses can be detected. Previous investigations conclude that thermal fatigue damage is produced by the porosity presence and can influence the coefficient of thermal efficiency behavior in MMC, tensile and fatigue properties are also affected [8,11]. Consequently, porosity content decreases mechanical properties of MMC—such as tensile strength, Poisson ratio, and Young's modulus.

Modeling of inclusion-matrix interaction or pore-matrix interaction at the microscale is usefully in accurately predicting effective properties (e.g., Young's modulus). In the literature, several constitutive models (analytical, semi-empirical, differential, and variational methods) for the prediction of mechanical properties with specified volume fractions can be found elsewhere. Among these models, the ones proposed by Voigt and Reuss (V–R) [12,13] and by Hashin–Shtrikman (H–S) [14] have proven to be effective means to obtain upper and lower bounds for the elastic moduli of the MMC from the known properties of its constituents. The H–S model represents the tightest bounds. This model is based on variational principles of linear elasticity and assumes isotropic composite. None of the previous methods (V–R, H–S) consider microstructural information.

Micromechanical analytical models also have been established to predict the mechanical properties of porous solids. Ramakrishnan and Arunachalam (R–A) [15] derived a useful analytical model using the principles of statistical continuum mechanics, where the effective elastic moduli of bulk material are predicted as a function of the volume fraction of the pores, the variation of the effective Poisson's ratio, and the elastic modulus of the corresponding dense material. This model considers an assemblage of hollow spheres. Additional information about other theoretical models for porous solids and its validity can be found in [16]. It is difficult to derive analytical solutions for particle–pore interaction systems because the stress distribution around particles and pores start interfering with each other.

The finite element modeling of micromechanics is an alternative means to analytical models for the simulation of mechanical properties. Finite element analysis has become increasingly more popular and an accurate approach to study different phases and complex morphologies of reinforcement particles in the microstructures [1]. Approaches are the unit cell model (UC) and the representative volume element (REV). In the UC approach, one or two particles are embedded in the metal matrix to represent a periodical array since this approach assumes that the material microstructure is periodic. Because of the periodic assumption, the UC approach is computationally efficient. The REV approach assumes random microstructures. Studies on numerical modeling in MMC have simplified the morphology of the particle reinforcement to that of a circle, rectangle, or ellipse to study the elastic response of the composite [17,18]. Good correlation between the numerical predictions and the experimental data was obtained. Available theoretical studies have shown the effect of reinforcement volume fraction on the stress distribution and modulus of MMC. However, such an understanding still lacks when particles

interact with pores in MMC, where the presence of pore close to particle or even within the particle produces inhomogeneous stress distributions and the load-bearing capacity of MMC is affected.

On the other hand, in polymer matrix composites containing fibers, numerical studies have shown that the porosity has a much larger influence in transversal properties than the longitudinal ones and a critical volume fraction exists below when the strength is unaffected by pores [19]. For solders, the effects of the morphology of intermetallic and porosity volume fraction on the modulus of the solder were studied by Chawla et al. [20]. They used a 2D microstructure based finite element modeling to study the effect of the morphology of Ag<sub>3</sub>Sn intermetallic and porosity on the Young's modulus of Sn–Ag solders. The Ag<sub>3</sub>Sn morphology was controlled by cooling rate; spherical and needle-like particles were obtained. They conclude that the morphology of the particles should not have a significant influence on Young's modulus of the Ag-solder. Rather, the porosity is responsible for the variability of the elastic moduli. However, in this study the porosity effect was not included in the numerical model, instead, it analyzed with the (R–A) analytical model.

MMC porosity arises generally by causes of gas entrapment and the evolution of dissolved gases [21]. Although the porosity in MMC can be diminished, its existence is unavoidable [22]. As porosity causes structural weakness in particulate composites, this factor remains as one of the focuses to attract researchers' attention in the development of high-performance materials. Ray [23] classified porosity of composites in two types: (a) at the boundary of the matrix phase and the reinforcement, and (b) away from the filler particles in the matrix alloy. In the works of Sun et al. [24] and Podymova et al. [10], it was found that pores coexist with the clustered and large-sized particles, and they significantly decrease the mechanical properties of the composites. The porosity in MMC arises from different origins, therefore it is of great interest to screening the inhomogeneous stress field around pores interacting with hard particles, and how the discontinuity produced by the pores has a damaging effect on the load-bearing capacity of the MMC. Finite element analysis is a means of properly interpreting the effect of porosity on the elastic properties of porous materials [16,19]. This paper aims to investigate the effect of porosity on the elastic modulus of SiC particle reinforced Al matrix composites. Finite element models based on the UC and REV approaches were developed. Porosity is considered within the Al matrix and within SiC particle to determine how the load-bearing capacity of the composite is affected by the different regions of stress concentration origins. The shapes of the reinforcement particle are angular and circular in the UC approach. Whereas, in the REV approach, the microstructures were developed to incorporate the mechanical interaction between the reinforcing particles. Firstly, the numerical methodology is validated against experimental data available in the literature ranging in a low and high-volume fraction of reinforcement. Also, the constitutive models of H–S, V–R, and R–A are used for reference.

## 2. Numerical Modeling

Square and circular morphologies of the particle reinforcement were selected to elucidate the effect of the inclusion shape in the elastic moduli. Two validation studies are conducted first by comparing the FEA results within experimental data reported for the system Co–WC [25] and experimental results for porous refractory spinel [16]. In the case of matrix strengthening, the composite matrix is made of cobalt (Co), whose elastic modulus  $E_2 = 207$  [GPa], Poisson's ratio  $\eta_2 = 0.31$  and shear modulus  $G_2 = 79$  [GPa]. The inclusion is tungsten carbide (WC) whose elastic modulus  $E_1 = 700$  [GPa], Poisson's ratio  $\eta_1 = 0.23$ , and shear modulus  $G_1 = 278$  [GPa]. For the Co–WC composite, experimental data of the elastic moduli as a function of the volume fraction of reinforcement ranging at high concentrations of filler are available in the literature [25]. Therefore, this data allows examining the reliability of the numerical model when high volume fractions are considered. As the volume fraction of the reinforcement increases, advanced micromechanical models are needed [26].

In the case of the porous material, the elastic modulus and Poisson's ratio of MgAl<sub>2</sub>O<sub>4</sub> are  $E_{spinel} = 268.2$  [GPa] and  $\nu_0 = 0.262$ , respectively. For modeling the pore, zero-moduli and zero-Poisson's ratio are assigned appropriately to avoid singularities in the numerical model. For computing the effective

elastic moduli of the materials, two-dimensional (2D) UCs models of  $8 \times 8$  mm with a different volume fraction of the reinforcement and porosity were created. Plane strain behavior is assumed. In the case of the UCs models the center of mass of the reinforcement particles coincides with that of the square representing the matrix. Pores are introduced explicitly in the metal matrix and within the particle reinforcement. Since the model is 2D, the volume fraction is equal to that of area fraction. The sizes of the particles are varied to obtain different volume fractions. For the REV models, the volume fraction and particle sizes are fixed. The unit cell is under tensile loading.

### 2.1. Linear Elasticity Equations

The governing equations for the static mechanic's problem are given by the equilibrium equation

$$\nabla \cdot \boldsymbol{\sigma} + \mathbf{f} = 0 \quad (1)$$

where,  $\boldsymbol{\sigma}$  and  $\mathbf{f}$  are the stress tensor and body force, respectively. For the stress-strain relation, it is assumed a plane strain model. Therefore, strain normal to the plane is zero, and shear strains that involve angles normal to the plane are assumed to vanish. Constituent materials are isotropic, so the constitutive equation ( $\boldsymbol{\sigma} = \mathbf{D}\boldsymbol{\varepsilon}$ ) is given by [27]

$$\mathbf{D} = \frac{E}{(1+\nu)(1+2\nu)} \begin{bmatrix} 1-\nu & \nu & 0 \\ \nu & 1-\nu & 0 \\ 0 & 0 & (1-2\nu)/2 \end{bmatrix} \quad (2)$$

where  $E$  is the Young's modulus and  $\nu$  the Poisson's ratio. Macroscopically, the heterogeneous material can be assumed as a homogenous medium. The average strains, stress and strain in the composite are related to the boundary displacements of the UC and the REV by Gauss theorem. Therefore, using appropriate boundary conditions to produce uniform stress and strain in the homogeneous medium, the relation between the actual heterogeneous composite and the homogeneous medium is given by averaging the stress and strain tensors over the area of the unit cell [28].

$$\bar{\sigma}_{ij} = \frac{1}{A} \int_A \sigma_{ij}(x, y) dA = \frac{1}{A} \int_{\Gamma} (Eu_i n_j + Eu_j n_i) d\Gamma \quad (3)$$

$$\bar{\varepsilon}_{ij} = \frac{1}{A} \int_A \varepsilon_{ij}(x, y) dA = \frac{1}{A} \int_{\Gamma} (u_i n_j + u_j n_i) d\Gamma \quad (4)$$

The effective elastic moduli of the metal matrix composite ( $E_c$ ), is given by substitution of the two previous equations into the Hook's law  $\bar{\sigma}_{ij} = E_c \bar{\varepsilon}_{ij}$ .

### 2.2. Finite Element Implementation

The 2D numerical models are developed using the mechanic's module in the software COMSOL Multiphysics. Boundary conditions assume plane strain-tension to evaluate the elastic modulus of the composites. Figure 1 shows the boundary conditions and the periodic microstructures that are considered for the UCs models. The mesh refinement is applied to ensure mesh independent solutions for each microstructure. The inclusion volume fraction is varied by changing the inclusion size in a parametric study, where the circular reinforcement is only able of producing volume fraction up to 0.71% while the square reinforcement a maximum volume fraction of 0.91%. The external load  $\mathbf{F}$  is set to 0.1 Pa. The microstructures used in the REV approach are shown in Section 3.2.5. This latter study was performed to compare the mechanical behavior predicted by the UCs models, with that predicted by the structure of real composite material. The boundary conditions are the same as those used in the UCs models.

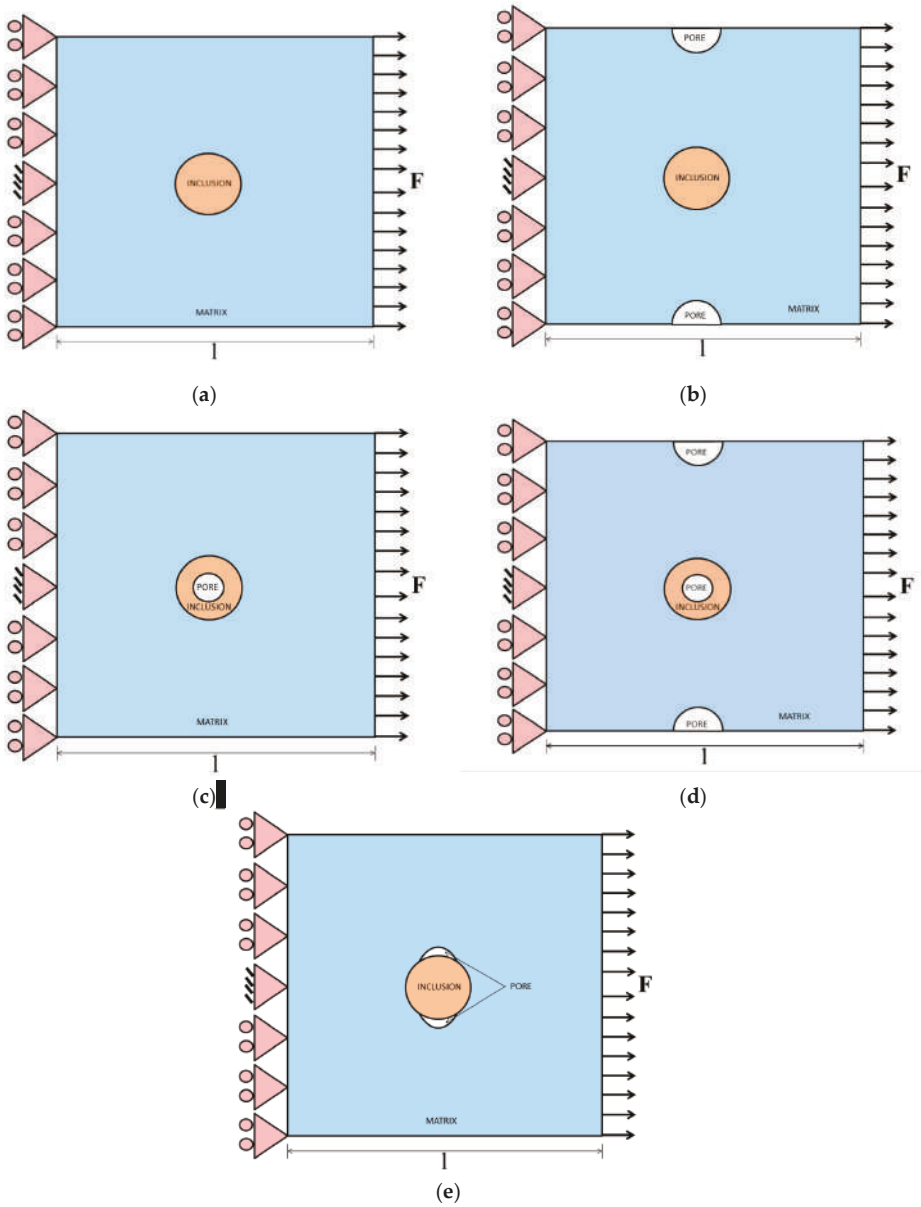


**Figure 1.** Schematic representation of the unit cell model and its boundary conditions. Particle reinforcements are considered square and circular. (a) Pore free matrix and pore-free particle. (b) Porous matrix and pore-free particle. (c) Pore free matrix and porous particle and (d) porous matrix and porous particle. (e) Porosity at particle–matrix interface. The triangles on the left side represent constraints displacement in the node.

### 3. Results and Discussions

#### 3.1. Comparison of FEA Predictions with Experimental Data

The numerical methodology was validated by comparing the numerical effective elastic modulus of the composites against experimental data published for the cemented carbides, which consist of WC particles distributed in cobalt [25]. This study considers small and large granules, with reinforcement volume fraction ranging from 50–90% and the elastic modulus were determined by resonant ultrasound spectroscopy (RUS) and impulse excitation. The elastic modulus predicted from the bounds of Hashin–Shtrikman (H–S) and Voigt–Reuss (V–R) is also used as a reference. The H–S micromechanical model is perhaps the most widely used because of its accuracy. Bounds are the tightest possible ones from a range of composite moduli; the two-phase material moduli can be obtained as

$$E^{\pm} = E_2 + \frac{\phi_1}{1/(E_1 - E_2) + (3\phi_2/(3E_2 + 4G_2))} \quad (5)$$

For the computation of the upper bound  $E_2 > E_1$ , meanwhile, the lower bound is computed by interchanging the subscripts (1, 2) in the previous equation. Here,  $E$  is the Young's modulus,  $G$  is the shear moduli, and  $\phi$  is the volume fraction.

Figure 2 shows the comparison between H–S bounds on the Young's modulus for the Co/WC system, experimental results [25] and numerical data obtained by simplifying the actual particle morphology to a square and a circle. V–R bounds are also plotted for reference. It is seen that the numerical predictions fall within the H–S bounds and that the square capture the angular nature of the WC particles since these data are closer to the experimental values (WC particles are angular). However, at the volume fraction of filler of 91%, the numerical prediction lies above the H–S upper bound. The numerical error was evaluated as  $|(E_{HS}^+ - E_{numerical})/E_{HS}^+|$ , which is lower than 3% at the volume fraction of 91% with  $E_{numerical} = 655$  [GPa] and  $E_{HS}^+ = 638$  [GPa]. Whenever the numerical predictions do not overtake the (V–R) bounds, the predictions are considered valid [29]. The upper bound of the V–R bounds is just 655 [GPa] at the volume fraction of 91%, so the numerical prediction lies at the upper bound of the V–R model and does not overtake this bound. This confirms that the predictions for the elastic moduli from the UC models developed are reliable. Results also show that the square particle has a little greater stiffening effect than the circular particles. Since the square particle values are close to the experimental ones, no additional effort was undertaken to consider a polygonal shape of the inclusion.

The information plotted in Figure 2 shows that the numerical model correctly predicts the stiffening effect. The validity of the developed numerical methodology was evaluated for the prediction of the effective Young's moduli when one phase of the composite has a zero-moduli and zero-Poisson's ratio. The analytical model for micromechanics of porous mediums proposed by Ramakrishnan and Arunachalam (R–A) was used as a reference. Experimental data reported in [16] was used to determine the accuracy of the numerical methodology in capturing the presence of pores in the composite. The R–A model was established considering that the dispersed phase of the composite has zero moduli, which means that in the porous area, the stress is zero but not the strain, the equations that describe this behavior are the following

$$E^* = E(1 - \theta)^2 / (1 + b_{\theta}\theta) \quad (6)$$

$$b_{\theta} = 2 - 3\nu_0 \quad (7)$$

where  $E$  is the Young's modulus of the fully dense material,  $\theta$  the porosity, and  $b_{\theta}$  is a constant that depends on the Poisson's ratio  $\nu_0$  of fully dense material.

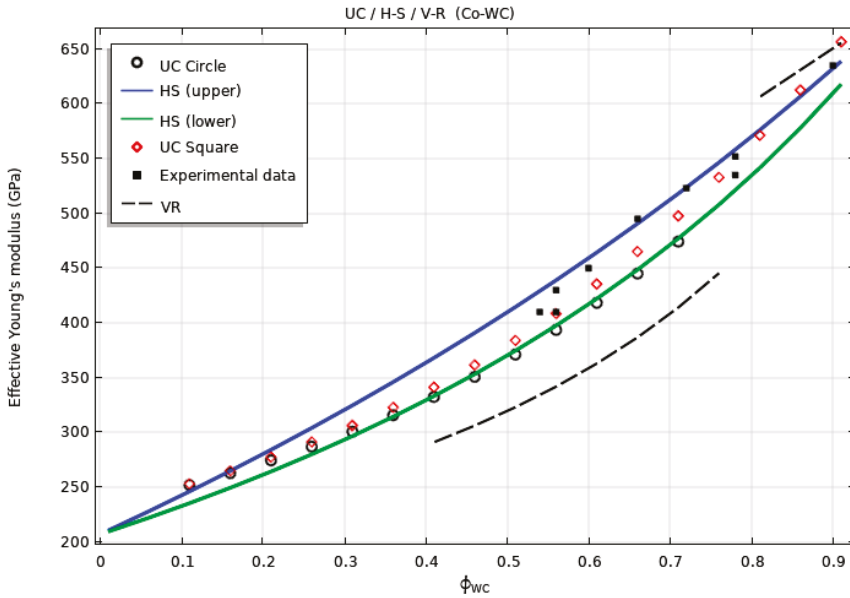


**Figure 2.** H–S bounds (—), experimental data (■) [25], numerical data (square ◊, circle ●) and V–R bounds (---) for the Young’s modulus for Co–WC system.

Numerical results were compared to the experimental data for the porous refractory spinel, where the effective elastic modulus was determined in [16] as a function of the porosity ranging from a fully dense material up to 40% porosity. Figure 3 shows this comparison when the pore shapes are circular and square to reflect the effect of pore shape on the Young’s moduli. The circular porous geometry fit the experimental data better than that of the square one. Since the simulation results with a circular pore show a close match to experimental data, the pore geometry considered in the UC models is only circular. The comparison between numerical results and experimental data shows that the present numerical models developed are also reliable when zero moduli and zero-Poisson’s ratio are assigned for one phase in the heterogeneous material. The computed results show that the UC model calculations are in good agreement with experimental data available in the literature [16,25] which proves the validity of the presented approach for microstructures of two phases. However, it is necessary to be careful when considering a three-phase material since it is necessary to place an inclusion (particle or pore) out from the center of mass of the UC model. In this work, pores are placed in the boundary, at the center of the UC and both the boundary and the center of the UC. In order to take into care that the composite behavior is not dominated by the boundary conditions (Saint-Venant’s principle), the influence of pore location on the computed elastic modulus was first established. As mentioned above, when the pore is in the center of mass of the UC, the numerical results are close to the experimental data in a wide range of values of pore content (Figure 3). On the other hand, when the pores are placed on the boundaries of the unit cell, the model predictions are reliable only when the pore content is ranging in low volume fraction as shown in Figure 4. Besides, it is observed that the model predictions are reliable when considering porosity up to 14% with a maximal deviation ( $(E_{exp} - E_{FEM})/E_{exp}$ ) of 6.6%. Thus, to interpret the numerical results properly when the pore is out from the center of mass of the UC, pore content should be lower than 14%. It is assumed that similar accuracy pertains when the numerical methodology is used to find the local stress and strain for the porous (Al/SiC) composites.

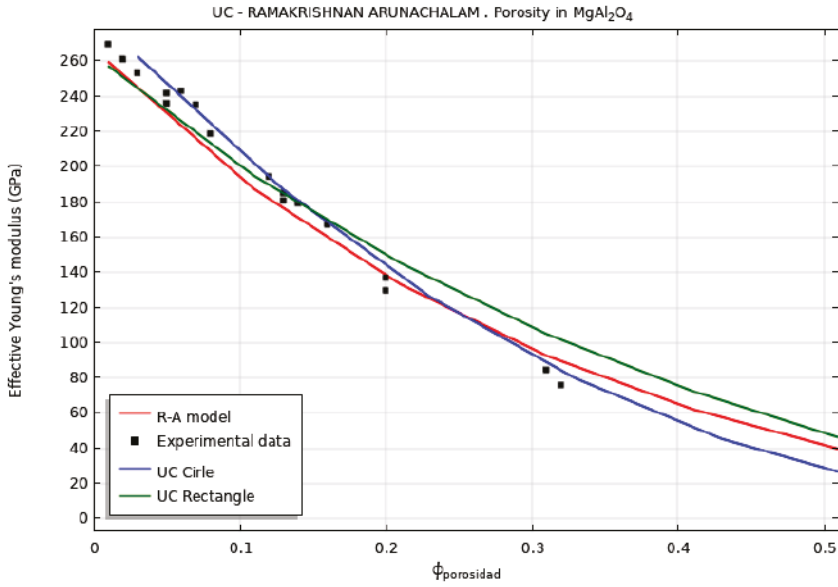


Figure 3. Variation of the effective elastic moduli for porous spinel. R–A model (—), experimental data (■) [16] and numerical data (square —, circle —).

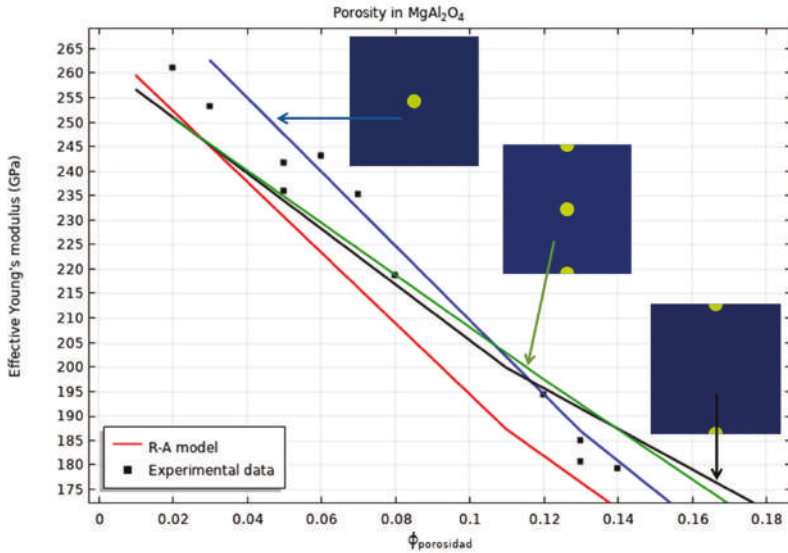


Figure 4. Influence of pore location on the numerical predictions of the elastic modulus. When the pore is placed at the center of mass, the model is reliable for a wide range of porous volume fraction. On the other hand, when the pores are placed in the boundaries of the UC, the model is reliable for porosity content ranging from 0% to 14% with an error lower to 7%.

### 3.2. SiC Particle Reinforced Aluminum Composites

Aluminum matrix composites possess both structural and functional applications, as a result, they are being increasingly used in several industries such as automotive; however, with the current

manufacturing process, it is difficult to avoid the porosity in MMC. Moreover, the porosity arises from different origins [10,23,24]. Therefore, the porosity has different destructive effects on the strength of the MMC. This factor has attracted the interest of the current research to investigate the effect of the porosity using finite element analysis on the load-bearing capacity of Al/SiC composites. The numerical models based on the microstructures shown in Figure 1 were constructed. The shape of the SiC particle is considered square and circular to determine the strengthening effect due to the particle's shape. The mechanical properties of the particle and matrix are shown in Table 1 [30]. The results are shown in the next section.

**Table 1.** Material properties of the SiC particle and Al matrix [30].

Material	Young's Modulus (GPa)	Poisson's Ratio
Al	74	0.33
SiC	410	0.19

### 3.2.1. Pore-Free Al-Matrix and Pore-Free SiC-Particle

Figure 5 illustrates the surface plots of von Mises stress in the microstructure when the particle and matrix are fully dense. Both unit cells (square and circular SiC-particle) are under the same external load and the volume fraction of reinforcement is 0.26%. For the SiC square particle (Figure 5a) the maximum stress value in the particle is 0.4 Pa, this stress is mainly concentrated at the corners of the particle. In the case of the circular SiC particle (Figure 5b), its maximum stress value is 0.11 Pa, which is concentrated at the contour of the particle. A comparison of both the square and circle particles shows that the stress gradient at the interface of the particle-matrix is larger when the reinforcement shape is angular (Figure 5a) than when is circular (Figure 5b). In both cases, the stress in the particle is larger than the stress in the matrix. Regarding the deformation in the composite, the strain in the matrix is larger than that of the particle because the particles are stiffer than the matrix. Based in the fact that the external load must equal the sum of the volume-averaged loads borne by the constituents (matrix and reinforcement). Then, if the reinforcement carries a relatively high proportion of the externally applied load, it is regarded as acting efficiently ( $\sigma_c = \sigma_m(1 - \phi) + \sigma_p\phi$ ) [31]. Then, the load is better transferred from the soft Al-matrix to the hard SiC particles when angular particles are used as reinforcement. These results agree with that reported in [17], where the load transfer by a shear-lag type of mechanism is more effective across planar interfaces than a spherical interface.

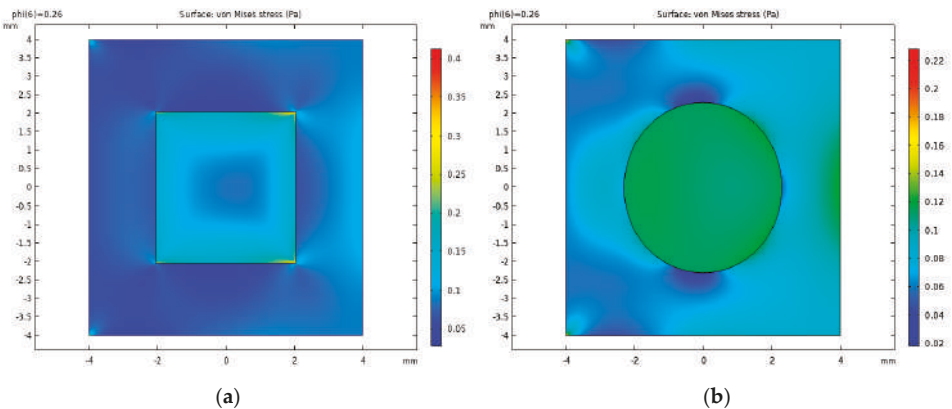


**Figure 5.** Surface plots of von Mises stress for the composite reinforced by SiC particles of (a) square shape and (b) circular shape. The volume fraction of reinforcement is 0.26%.

Figure 6 shows that, at low volume fractions of particle reinforcement, the effective elastic modulus of the circular particles composite is like that obtained with angular particles (red and black dashed lines). Then, the amount of transfer external-load from the matrix to the particle reinforcement at low volume fractions of SiC particles is similar for angular than circular particles. Therefore, at low volume reinforcement content, the particle shape has little effect on the elastic modulus of the composite. Figure 6 also shows the comparison between H–S bounds on Young’s modulus for the Al/SiC system with data from various Al/SiC MMCs experimental results [32–37] and the numerical data obtained in this study. In the plot, the gathered experimental data—as well as the numerical predictions on the Young’s modulus of the composite—lies near the lower bound of the H–S model. Therefore, the prediction on the strength of the Al–SiC composites can be done with a high level of confidence using the lower bound of the H–S micromechanical model. Numerical predictions of the elastic modulus based on the square and circular SiC particles are very close to the reported measured data for the Al alloy–SiC systems. As the volume fraction of SiC increases, angular particles strengthen the composite better than the circular ones do. According to the H–S lower bound, the circular shape in the numerical model underpredicts the elastic modulus of the Al–SiC composite. Though these predictions (with circular particles) fall off from the H–S lower bound, the data reported by Qu et al. [34] demonstrates that the numerical predictions are reliable and the condition proposed in [29], is confirmed; while the V–R bounds are not overtaken, the numerical model is reliable. However, the accuracy of the numerical results must be checked by comparing the results to experimental data.

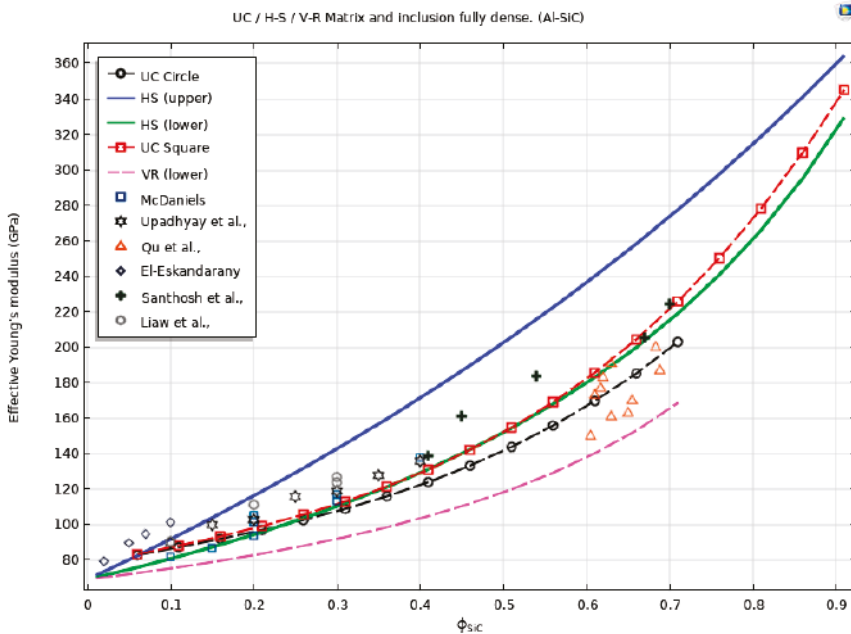
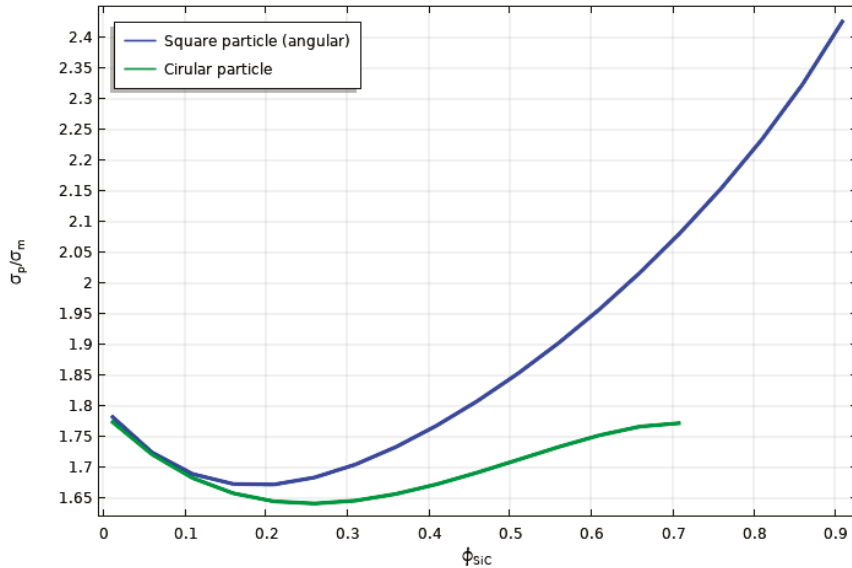


Figure 6. Effect of reinforcement content on the elastic modulus of Al–SiC composite. H–S bounds (—), experimental data [32–37], numerical data (square ■, circle ●) and V–R bounds (---).

The SiC square or angular particle reinforced Al matrix composites endure more load than reinforced with SiC round particles as shown in Figure 7. This plot shows the stress ratio (stress in the particle and the stress in the matrix,  $\sigma_p / \sigma_m$ ) as a function of the reinforcement volume fraction. It is considered that the composite remains elastic independently of the applied load [31]. It is found that the square and circular particles endure the same load to the volume fraction up to 11%. However,

above this reinforcement content, the angular particle endures more load. Then, the effective elastic modulus of the MMC is independent of the particle morphology when the reinforcement content is lower than 11%.



**Figure 7.** The portion of the external load borne by each of the constituents of the composite. Square particle (blue) and circular particle (green).

### 3.2.2. Porous Al-Matrix and Pore-Free SiC Particle

The porosity significantly affects the mechanical performance of the composites. The porosity increases as the weighting percentage of particles increases. In [21] it was found that the porosity content of the Al composites varied from 1.01% to 2.69% with the increased SiC wt % from 0% to 25%. A parametric study was performed, where a similar increase-relationship between the amount of porosity and the content of SiC particles is maintained; where the porosity increases as the volume fraction of reinforcement do. Porosity content (volume fraction) varies from 0% to 3.1% with SiC particle added from 1% to 31%. Figure 8 shows the surface plots of von Mises stress in the microstructure when the Al-matrix is porous, and the SiC-particle is fully dense. These results are based on the microstructure shown in Figure 1b. The maximum stress obtained in the square particle is about 0.5 MPa (Figure 8a). Whereas, for the circular particle, the maximum stress in the particle is 0.14 MPa (Figure 8b). In both Al-matrixes (square and circular particle) high-stress concentration around the pore is observed, with a value of about 0.2 MPa, however, the stress in the matrix is bigger than the stress in the particle in the case of the circular reinforcement. As the stress in the SiC square particle is higher than that of the Al-matrix, the load transfer remains effective despite the presence of pores in the Al-matrix. In Figure 8b it is shown that the stress gradient at the interface of the SiC circular particle and Al-matrix is low; namely at some points of the interface, the matrix and the reinforcement endure the same load.

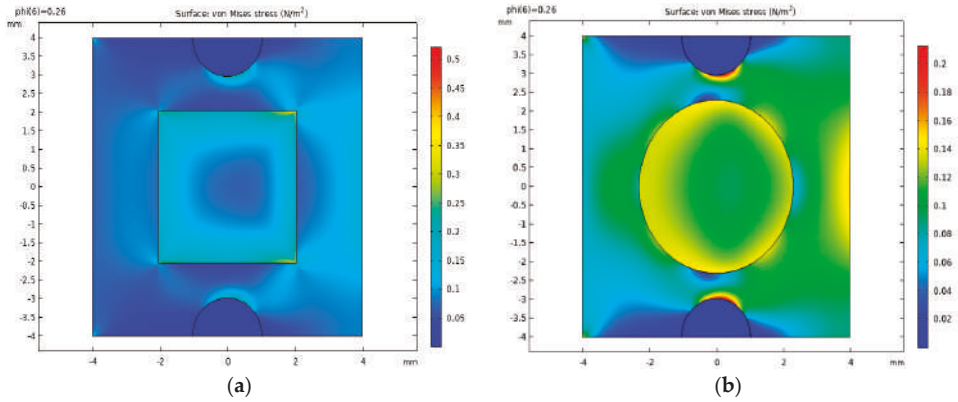


**Figure 8.** Von-Mises stress distribution of 26% SiC particulate filled porous-aluminum matrix under tensile loading. (a) Square shape and (b) circular shape.

### 3.2.3. Pore Free Al-matrix and Porous SiC Particle

Figure 9 shows the surface plots von Mises stress in the microstructure when the Al-matrix is fully dense, and the SiC-particle is porous. These results are based on the microstructure shown in Figure 1c. For the square porous particle (Figure 9a), the stress in the particle (maximum stress 0.44 Pa) is greater than the stress in the matrix, which shows that strengthening of the composite is by transfer load from the soft Al-matrix to the SiC hard particle. The stress concentration around the pore within the particle is 0.35 Pa, while the stress located in the angles of the particle is 0.44 Pa. In the case of the SiC circular particle (Figure 9b), the maximum stress in the particle is around the pore with a value of 0.42 Pa, while in the Al-matrix the stress is lower, so transfer load is also effective in this case. Stress concentration around the pore is higher for the circular particles than square particles, which means that circular porous particles are more prone to fracture than angular porous particles when pores coexist inside the particles.

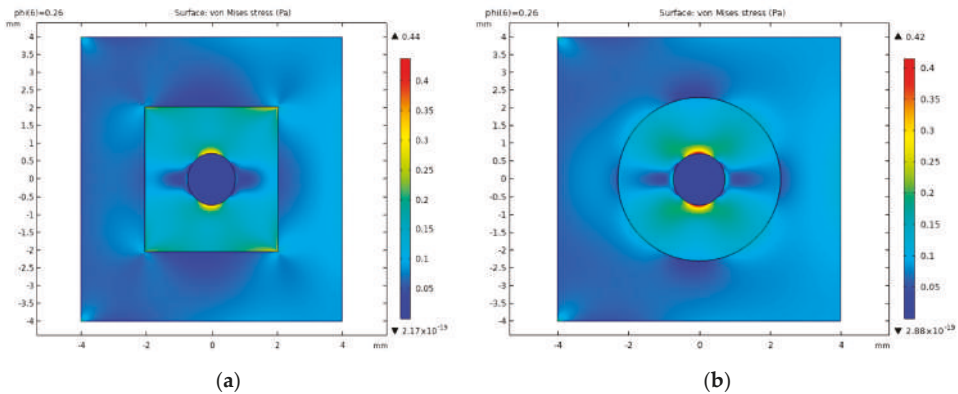


**Figure 9.** Von Mises stress distribution of SiC porous-particulate filled aluminum matrix under tensile loading. (a) Square shape and (b) circular shape. The volume fraction of SiC particles and pore content is 26% and 2.6%, respectively.

### 3.2.4. Porous Al-Matrix and Porous SiC Particle

Figure 10 shows the surface plots of von Mises stress in the microstructure when the Al-matrix and the SiC-particle are both porous. These results are based on the microstructure shown in Figure 1d. In this case, the total porosity is divided into an equal content in the matrix and the particle; so, the pore content in the matrix is 1.3%, while the pore content in the particle is 1.3%. The total pore content in the composite is 2.6%. Figure 10a,b show that the stress concentration around the pore in the Al-matrix is about 0.2 Pa in both cases (the square particle and circular one). However, the stress around the pore in the SiC particle reinforcement is bigger for the circular particle (0.39 Pa) than the stress in the pore located in the square particle (0.31 Pa). Therefore, when the matrix is porous, the stress gathering around the pore within the particles is lower than when the matrix is fully dense. That means that the pore in the matrix reduces the transfer load mechanism and more load is endured by the matrix lowering the strengthening of the composite. For the square SiC particle, the maximum stress (in the corners) is 0.5 Pa, while the stress in the Al-matrix is 0.2 Pa, this shows that the transfer load mechanism from the matrix to the reinforcement remains despite the pore presence at the matrix and particle.

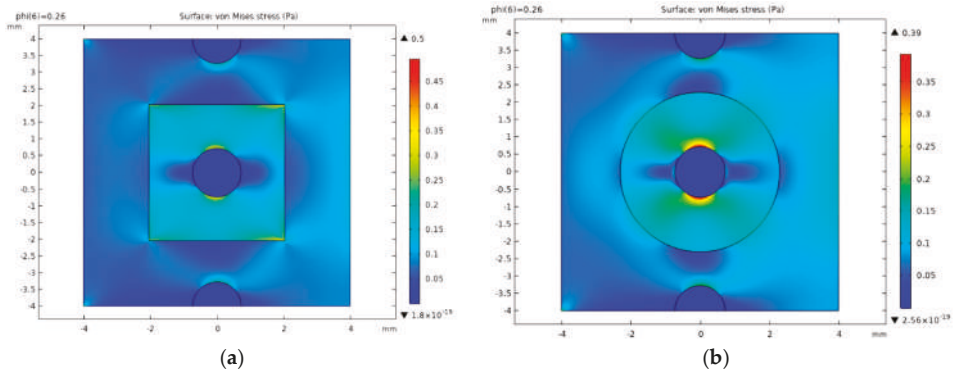


**Figure 10.** Von Mises stress distribution of SiC porous-particulate filled porous aluminum matrix under tensile loading. (a) Square shape and (b) circular shape. The volume fraction of SiC particles and pore content is 26% and 2.6%, respectively.

### 3.2.5. Porosity at Matrix–Particle Interface

Figure 11 shows the surface plots of von Mises stress in the microstructure when the pore is located at the particle-matrix interface. For the square particle (Figure 11a), the stress in the particle (0.3 Pa) is greater than the stress in the matrix (0.09 Pa), which shows that strengthening of the composite is by transfer load from the soft Al-matrix to the SiC hard particle. The stress is concentrated at the particle corners, but the highest stress concentration (0.5 Pa) is located at some contact points between the particle, matrix, and pore. In the case of the SiC circular particle (Figure 11b), the stress concentration is at all the contact points among the particle, matrix, and pore, and when compared to the square particle, the stress intensity is two-fold. Moreover, the stress level in the particle (0.13 Pa) is a little bit greater than that in the matrix (0.11 Pa). Therefore, in the case of the circular particles, the pores located at the particle-matrix interface significantly affect the transfer load mechanism, whereas in the case of the angular particles, the transfer load remains effective still because a relatively high proportion of the externally applied load is endured by the particle. As mentioned in Ray [23] this type of porosity aid the debonding of particles from the matrix under low stress, because the interface damage starts to develop since the contact points among the particle matrix and the pores act as a stress concentrator, as shown here.

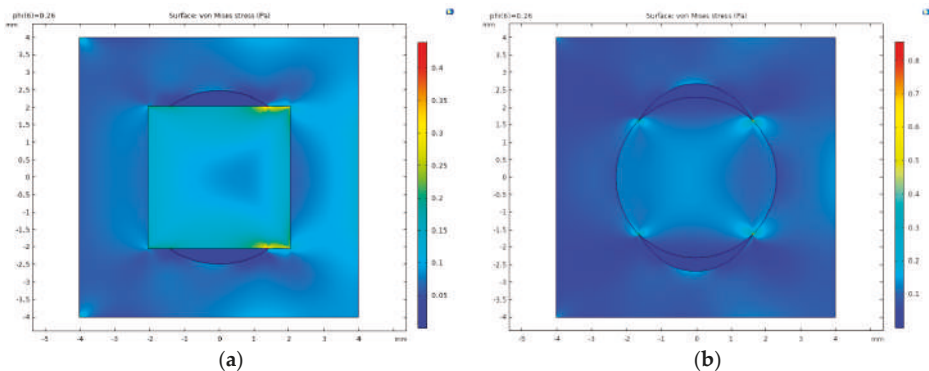


**Figure 11.** Surface plots of the von Mises stress for the composite reinforced by SiC particles of (a) square shape and (b) circular shape. The volume fraction of SiC particles and pore content is 26% and 2.6%, respectively. Porosity at particle–matrix interface.

It is found that square particles carry much higher stress than matrix in the case of porous matrix and fully dense particle (Figure 8a). Whereas, in the case of the circular particle, it carries much higher stress than matrix when the particle is porous, and the matrix is fully dense (Figure 9b). From the previous results, it can be seen that despite the presence of pore in the composite, stress transfer from the soft matrix to the hard particle is effective in all cases, except in the case of fully dense circular particle and porous matrix (Figure 8b), where the matrix endures more load than the particle. Then, the transfer load is lowered, and this is reflected as a reduction in the elastic modulus of the composite (Figure 12, black line with circular markers). Figure 12 shows the results gathered from the parametric study to demonstrate the effect of the porosity in the elastic modulus of the SiC particle reinforced Al matrix. In this parametric study, porosity content varies from 0% to 3.1% with SiC particle added from 1% to 31%. For the studied cases that consider coexistence of pores inside the particle and the matrix, the greater impairing on the Young's modulus of the composite was found to be in the case of the fully dense particle and porous matrix. The lower impairing on the elastic modulus of the composite is for the porous particle and fully dense matrix. Intermediate values on the impairing of the Young's modulus of the composite are for the case of porous particle and porous matrix, as well as the pore located at particle–matrix interface when the particle is circular. For the square or angular particles, the pore within the particle affects the load transfer mechanism in a similar manner to the pore located at the particle matrix interface. These results mean that the elastic property of the composite is more sensitive to the porosity in the matrix because the particles are stiffer than the matrix. The declining trend for the elastic moduli is consistent in both the angular and circular particle shapes. In all cases, the square or angular particles strengthen the composite when compared to the circular particles. From the results, it is concluded that the disrupting of continuity in the composite by the presence of pores causes elastic relaxation of the matrix, which leads to the reinforcement particles (angular or circular) undergoing increased loads. Consequently, this leads to a relaxation in the particle, and there is a drop in its stress gathering capability, and thus the resulting effective elastic modulus of the Al/SiC composite decreases. Therefore, the data indicate that the porosity in the composite matrix is the main cause in the impairing of the elastic modulus in MMC. In practice, the scatter of experimental data on the elastic modulus is caused mainly by the porosity in the composite because the difficult of experimentally reproducing the same porosity in the composite every test. Table 2 shows how the % increment in porosity in the matrix reduces the elastic modulus of the composite. Moreover, despite the volume fraction of the reinforcement is increased, if the porosity increase, the impairing on the Young's modulus is increased also. Therefore, the porosity plays a significant role in the strength of the

composites, and for a given porosity in the matrix, it impairs the Young’s modulus in the same way independently of the shape of the SiC-reinforcement.

**Table 2.** Porosity increase in the Al-matrix and its effect on the Young’s modulus of the composite.

SiC Volume Fraction	10%	-	20%	-	30%	-
Shape of the Particle	1% in porosity	% reduction	2% in porosity	% reduction	3% in porosity	% reduction
Square	88.2 GPa * 80.8 GPa †	8.3	99.3 GPa * 85.1 GPa †	14.3	113.15 GPa * 94.7 GPa †	16.3
Circular	87.3 GPa * 80.0 GPa †	8.3	97.1 GPa * 82.9 GPa †	14.6	109.0 GPa * 90.2 GPa †	17.2

\* Pore-free matrix † Porous matrix.

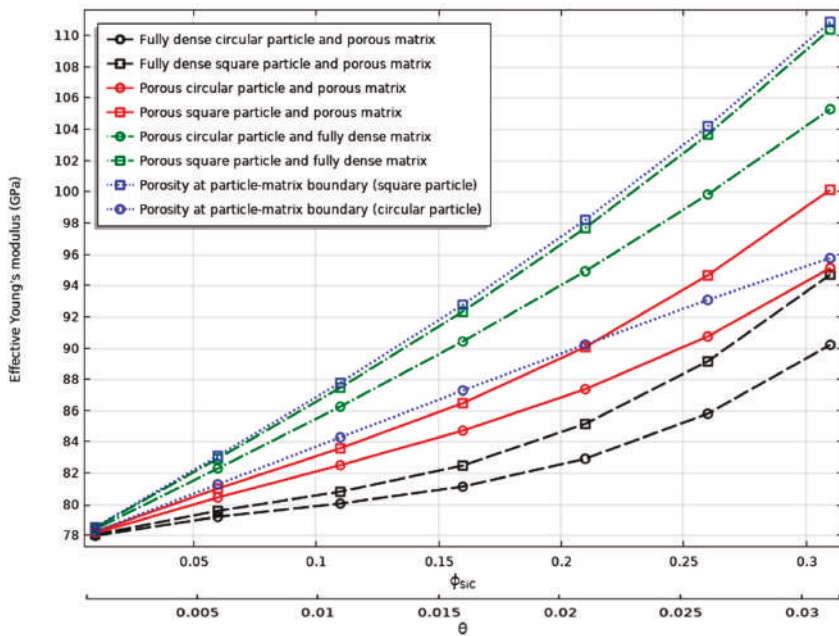


**Figure 12.** Effect of porosity in the elastic modulus of the Al-SiC composite.  $\phi_{SiC}$  is the reinforcing content and  $\theta$  is the porosity content in the composite. Square markers are for the square particle while circular markers are for the circular particle.

### 3.2.6. REV Models with SiC Particles Representing 2D Real Microstructures

The effective material properties are linked to the microstructure of composite. Therefore, the global behavior of the material depends on the microstructure, and modeling of the microstructure is as important as the prediction of global behavior. To visualize the difference between the material properties predictions conducted by assuming a single SiC particle of simple geometry in a unit cell, and those predictions of a cell model with several SiC particles exhibiting statistical homogeneity and isotropy as the real microstructures. Thus, two cell models (REV approach) that display distribution and orientation of particles of different sizes and shapes are established. The interactions between the particles produce a complicated local stress field with high stress concentrations which depends on the particle morphology. Figure 13 shows the developed microstructures. By comparing these

microstructures with the experimentally obtained microstructures for SiC reinforced Al matrix composites reported elsewhere, they are quite similar in the context that the position of the polygonal particles are randomly defined, the particles present different sizes, shapes, and orientation. Hence, these microstructures capture the same complicated mechanical interactions as the experimental ones will do. The volume fraction of reinforcement is 12% (Figure 13a) whereas the pore content is 1.2% in volume fraction (Figure 13b). The finite element implementation of these unit cell models is the same followed in Section 2.2, with the main difference that in this section, a parametric study is not needed, due to the volume fraction of the constituents is fixed. It is important to note that despite the shape of some pores look like a circle, they are not perfectly circular.

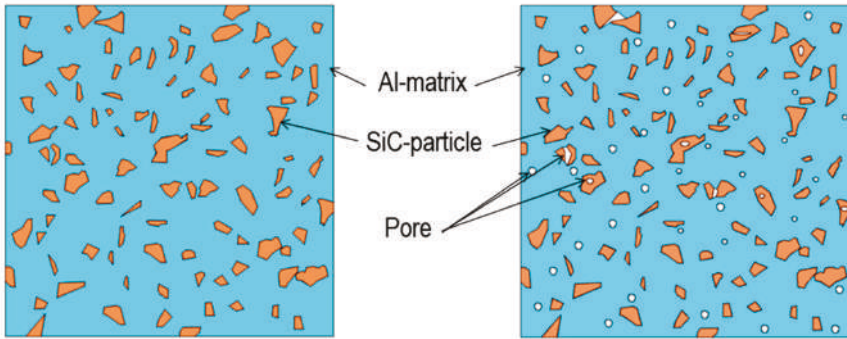


**Figure 13.** Developed microstructures for Al-SiC composite. (a) Fully dense materials and (b) porous materials.

Figure 14a,b show the surface plots of von Mises stress in the Al-matrix and the SiC particles, respectively. The stress in the particles is larger than in the matrix, and the stress in the particles is mainly concentrated in the sharp angular corners. These results are in agreement with the stress fields shown previously in Sections 3.2.1–3.2.5. Moreover, the stress field magnitudes are similar for the matrix as well as for the particles. The Young’s modulus of the composite using this microstructure is 91.06 GPa, while Young’s modulus predicted by the unit cell (used in Section 3.2.1) is 89.35 GPa. Evaluating the difference, this value is lower than 2%.

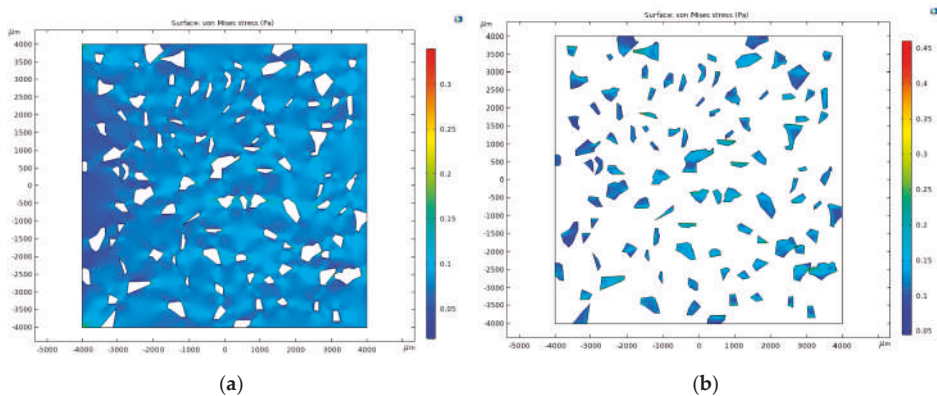


**Figure 14.** Von Mises stress distribution in (a) matrix and (b) particles. Constituents are fully dense.

Figure 15a,b show the surface plots of von Mises stress in the porous Al-matrix and the SiC particles (some particles are porous), respectively. The presence of the pores within the composite

produces higher stress in the matrix as well as in the particles, but the particles are under higher stress when compared to the fully dense composite, indicating that the particles undergoing increased loads. The stress is concentrated in the poles of the pores, in the sharp angular corners of the particles and at the contact points among the particle, matrix, and pore. The Young's modulus of this porous composite is 86.6 GPa. The pore content of 1.2% (volume fraction), reduced the elastic modulus by about 5% (from 91.06 to 86.6 GPa) despite the load transfer is increased. The mechanical behavior observed within the structure of a real composite material under load, is similar to that observed in the results of Sections 3.2.1–3.2.5. Thus, as the results computed with the UCs models are coincident with experimental data, as well as with the results computed by the REV models, the conclusions drawn by this research are confirmed. Therefore, the presence of the pores leads to a relaxation of the composite and reduces its stress gathering capability.

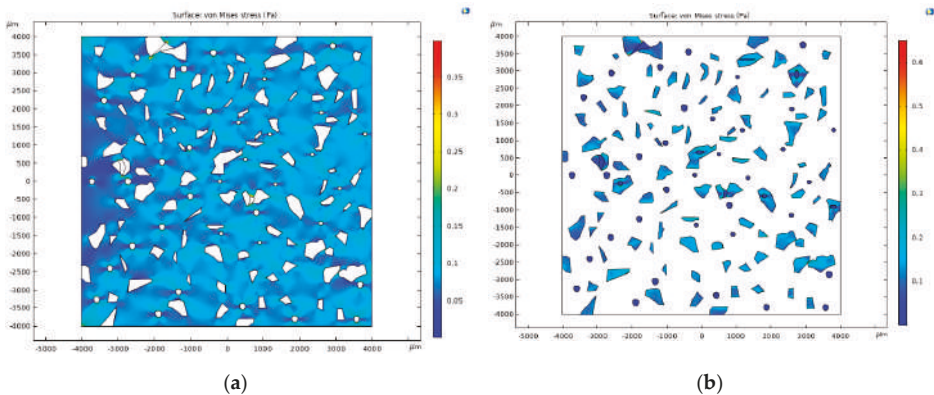


**Figure 15.** Von Mises stress distribution in (a) matrix and (b) particles. Matrix is porous while particles are both porous and pore free.

#### 4. Conclusions

In the present work, 2D models (UC and REV approaches) and finite element analysis are used to investigate the porosity effect on the SiC particle reinforced Al matrix composites. The reliability of the numerical methodology was validated by comparing the numerical results against several experimental data, micromechanical constitutive models, and structures that represent real composite materials. The main results to be highlighted are as follows:

- (1) In the case of fully dense SiC particles and fully dense Al-matrix, the square and circular particles endure the same load to the volume fraction up to 11%. However, above this reinforcement content, the angular particle endures more load. Therefore, the effective elastic modulus of the MMC is independent of the morphology when the reinforcement content is lower to 11%.
- (2) Despite the presence of pore in the composite, stress transfer from the soft matrix to the hard particle is effective in all cases, except in the case of fully dense circular particle and porous matrix.
- (3) For pores within the particles, the stress concentration around the pore is higher for the circular particles than the square ones.
- (4) The elastic modulus is more sensitive to porosity in the matrix, which is a common defect in MMC.
- (5) For the square or angular particles, the pore within the particle affects the load transfer mechanism in the same way to the pore located at the particle matrix interface.
- (6) For the porosity at the particle–matrix interface, the contact points among the particle, matrix, and the pore acts as a stress concentrator.

- (7) The porosity plays a significant role in the strength of the composites, and for a given porosity in the matrix, it impairs the Young's modulus in the same way independently of the shape of the SiC-reinforcement.

**Author Contributions:** Conceptualization, J.E.R.-S. and K.M.G.-J.; methodology, J.E.R.-S. and K.M.G.-J.; software, J.E.R.-S.; validation, J.E.R.-S. and K.M.G.-J.; formal analysis, J.E.R.-S.; investigation, J.E.R.-S.; resources, A.C.-R., J.A.R.-S., V.H.G.-P., A.M.-P., and E.H.-H.; data curation, J.E.R.-S.; writing—original draft preparation, J.E.R.-S. and K.M.G.-J.; writing—review and editing, J.E.R.-S., K.M.G.-J., A.C.-R. and A.M.-P.; visualization, J.E.R.-S., K.M.G.-J., A.C.-R., J.A.R.-S., A.M.-P., E.H.-H., and V.H.G.-P.; supervision, J.E.R.-S., A.C.-R., and J.A.R.-S.; project administration, J.E.R.-S.; funding acquisition, J.E.R.-S., K.M.G.-J., A.C.-R., J.A.R.-S., E.H.-H., A.M.-P. and V.H.G.-P. All authors have read and agreed to the published version of the manuscript.

**Funding:** This research was funded by CONACYT, grant number “A1-S-9692” and “The APC was funded by CONACYT A1-S-9692”.

**Acknowledgments:** The authors wish to thank the Institutions CONACYT, SNI, Centro de Investigación en Química Aplicada, and Instituto Politécnico Nacional, for their permanent support. J.E. Rivera gratefully acknowledges the financial support received from Cátedras CONACYT project 809.

**Conflicts of Interest:** The authors declare no conflict of interest.

## References

- Arreola-Herrera, R.; Cruz-Ramírez, A.; Rivera-Salinas, J.E.; Romero-Serrano, J.A.; Sánchez-Alvarado, R.G. The effect of non-metallic inclusions on the mechanical properties of 32 CDV 13 steel and their mechanical stress analysis by numerical simulation. *Theor. Appl. Fract. Mech.* **2018**, *94*, 134–146. [\[CrossRef\]](#)
- Kulkarni, S.G.; Achche, L.; Menghani, J.V. Effect of reinforcement type and porosity on strength of metal matrix composite. *Int. J. Comput. Mater. Sci. Eng.* **2016**, *5*, 1650006. [\[CrossRef\]](#)
- Shen, L.; Finot, M.; Needleman, A.; Suresh, S. Effective plastic response of two-phase composites. *Acta Metall. Mater.* **1995**, *43*, 1701–1722. [\[CrossRef\]](#)
- Chawla, N.; Chawla, K.K. Microstructure-based modeling of the deformation behavior of particle reinforced metal matrix composites. *J. Mater. Sci.* **2006**, *41*, 913–925. [\[CrossRef\]](#)
- Nasher, N.; Hori, M. *Micromechanics: Overall Properties of Heterogeneous Materials*, 2nd ed.; Elsevier: North-Holland, The Netherlands, 1999.
- Gentieu, T.; Catapano, A.; Jume, J.; Broughton, J. Computational modeling of particulate-reinforced materials up to high volume fractions: Linear elastic homogenization. *J. Mater. Des. Appl.* **2019**, *233*, 1101–1116.
- Hassani, A.; Bagherpour, E.; Qods, F. Influence of pores on workability of porous Al/SiC composites fabricated through powder metallurgy + mechanical alloying. *J. Alloys Compd.* **2014**, *591*, 132–142. [\[CrossRef\]](#)
- Schöbel, M.; Requena, G.; Fiedler, G.; Tolnai, D.; Vaucher, S.; Degischer, H.P. Void formation in metal matrix composites by solidification and shrinkage of an AlSi7 matrix between densely packed particles. *Compos. Part A Appl. Sci. Manuf.* **2014**, *66*, 103–108. [\[CrossRef\]](#)
- Arif, M.N.; Bukhari, M.Z.; Brabazon, D.; Hashmi, M.S.J. Coefficient of thermal expansion (CTE) study in metal matrix composite of CuSiC vs. AlSiC. *IOP Conf. Ser. Mater. Sci. Eng.* **2019**, *701*, 012057. [\[CrossRef\]](#)
- Podymova, N.B.; Kalashnikov, I.E.; Bolotova, L.K.; Kobeleva, L.I. Laser-ultrasonic nondestructive evaluation of porosity in particulate reinforced metal-matrix composites. *Ultrasonics* **2019**, *99*, 105959. [\[CrossRef\]](#)
- Schöbel, M.; Altendorfer, W.; Degischer, H.P.; Vaucher, S.; Buslaps, T.; Di Michiel, M.; Hofmann, M. Internal stresses and voids in SiC particle reinforced aluminum composites for heat sink applications. *Compos. Sci. Technol.* **2011**, *71*, 724–733. [\[CrossRef\]](#)
- Voigt, W. Über die Beziehung zwischen den beiden Elastizitätskonstanten Isotroper Körper. *Wied. Ann. Phys.* **1889**, *38*, 573–587. [\[CrossRef\]](#)
- Reuss, A. Berechnung der Fließgrenze von Mischkristallen auf Grund der Plastizitätsbedingung für Einkristalle. *J. Appl. Math. Mech.* **1929**, *9*, 49–58.
- Hashin, Z.; Shtrikman, S. A variational approach to the theory of the elastic behavior of multiphase materials. *J. Mech. Phys. Solids* **1963**, *11*, 127–140. [\[CrossRef\]](#)
- Ramakrishnan, N.; Arunachalam, V. Effective elastic moduli of porous solids. *J. Mater. Sci.* **1990**, *25*, 3930–3937. [\[CrossRef\]](#)
- Ramakrishnan, N.; Arunachalam, V. Effective elastic moduli of porous ceramic materials. *J. Am. Ceram. Soc.* **1993**, *76*, 2745–2752. [\[CrossRef\]](#)

17. Chawla, N.; Shen, Y. Mechanical behavior of particle reinforced metal matrix composites. *Adv. Eng. Mater.* **2001**, *6*, 357–370. [[CrossRef](#)]
18. Chawla, N.; Ganesh, V.; Wunsch, B. Three-dimensional (3D) microstructure visualization and finite element modeling of the mechanical behavior of SiC particle reinforced aluminum composites. *Scr. Mater.* **2004**, *51*, 161–165. [[CrossRef](#)]
19. Dong, C. Effects of process-induced voids on the properties of fibre reinforced composites. *J. Mater. Sci. Technol.* **2016**, *32*, 597–604. [[CrossRef](#)]
20. Deng, X.; Koopman, M.; Chawla, K.K.; Scarritt, S. Measurement and prediction of Young's modulus of a Pb-free solder. *J. Mater. Sci. Mater. Electron.* **2004**, *15*, 385–388.
21. Kukshal, V.; Gangwar, S.; Patnaik, A. Experimental and finite element analysis of mechanical and fracture behavior of SiC particulate filled A356 alloy composites: Part I. *J. Mater. Des. Appl.* **2015**, *229*, 91–105. [[CrossRef](#)]
22. Hashim, J.; Looney, M.; Hashmi, M.S.J. The enhancement of wettability of SiC particles in cast aluminum matrix composites. *J. Mater. Process. Technol.* **1999**, *1*, 329–335.
23. Ray, S. Review Synthesis of cast metal matrix particulate composite. *J. Mater. Sci.* **1993**, *28*, 539–5413. [[CrossRef](#)]
24. Sun, C.; Song, M.; Wang, Z.; He, Y. Effect of particle size on the microstructures and mechanical properties of SiC-reinforced pure aluminum composites. *J. Mater. Eng. Perform.* **2011**, *20*, 1606–1612. [[CrossRef](#)]
25. Koopman, M.; Chawla, K.K.; Coffin, C.; Patterson, B.R.; Deng, X.; Patel, B.V.; Fang, Z.; Lockwood, G. Determination of elastic constants in WC/Co metal matrix composites by resonant ultrasound spectroscopy and impulse excitation. *Adv. Eng. Mater.* **2002**, *4*, 37–42. [[CrossRef](#)]
26. Eroshkin, O.; Tsukrov, I. On micromechanical modeling of particulate composites with inclusions of various shapes. *Int. J. Solids Struct.* **2005**, *42*, 409–427. [[CrossRef](#)]
27. Fish, J.; Belytschko, T. *A Fist Course in Finite Elements*; John Wiley and Sons, Ltd.: Hoboken, NJ, USA, 2007.
28. Sun, C.T.; Vaidya, R.S. Prediction of composite properties from a representative volume element. *Compos. Sci. Technol.* **1996**, *56*, 171–179. [[CrossRef](#)]
29. Tillmann, W.; Klusemann, B.; Nebel, J.; Svendsen, B. Analysis of the mechanical properties of an Arc-sprayed WC-FeCSiMn coating: Nanoindentation and simulation. *J. Therm. Spray Technol.* **2011**, *20*, 328–335. [[CrossRef](#)]
30. Ganesh, V.V.; Chawla, N. Effect of particle orientation anisotropy on the tensile behavior of metal matrix composites: Experiments and microstructure-based simulation. *Mater. Sci. Eng. A* **2005**, *391*, 342–353. [[CrossRef](#)]
31. Clayne, T.W.; Withers, P.J. *An Introduction to Metal Matrix Composites*; Cambridge University Press: Cambridge, UK, 1995.
32. McDaniels, D.L. Analysis of stress-strain, fracture, and ductility behavior of aluminum matrix composites containing discontinuous silicon carbide reinforcement. *Metall. Trans. A* **1985**, *16*, 1105–1115. [[CrossRef](#)]
33. Upadhy, A.; Ramvir, S. Prediction of effective elastic modulus of biphasic composite materials. *Mod. Mech. Eng.* **2012**, *2*, 6–13. [[CrossRef](#)]
34. Qu, S.G.; Lou, H.S.; Li, X.Q. Influence of particle size distribution on properties of SiC particles reinforced aluminum matrix composites with high SiC particle content. *J. Compos. Mater.* **2016**, *50*, 1049–1058. [[CrossRef](#)]
35. Sherif El-Eskandarany, M. Mechanical solid state mixing for synthesizing of SiCp/Al nanocomposites. *J. Alloys Compd.* **1998**, *279*, 263–271. [[CrossRef](#)]
36. Santhosh Kumar, S.; Seshu Bai, V.; Rajkumar, K.V.; Sharma, G.K.; Jayakumar, T.; Rajasekharan, T. Elastic modulus of Al-Si/SiC metal matrix composites as a function of volume fraction. *J. Phys. D Appl. Phys.* **2009**, *42*, 175504. [[CrossRef](#)]
37. Liaw, P.K.; Shannon, R.E.; Clark, W.G.; Harrigan, W.C.; Jeong, H.; Hsu, D.K. Nondestructive characterization of material properties of metal-matrix composites. *Mater. Chem. Phys.* **1995**, *39*, 220–228. [[CrossRef](#)]

